

RIJKSUNIVERSITEIT GRONINGEN

Digital Pulse-Shape Analysis and Controls for Advanced Detector Systems

Proefschrift

ter verkrijging van het doctoraat in de
Wiskunde en Natuurwetenschappen
aan de Rijksuniversiteit Groningen
op gezag van de
Rector Magnificus, dr. E. Sterken,
in het openbaar te verdedigen op
maandag 9 januari 2012
om 14:30 uur

door

Victor Ionuț Stoica

geboren op 12 mei 1983
te Boekarest, Romania

Promotor: Prof. dr. N. Kalantar-Nayestanaki
Copromotores: Dr. H. J. Wörtche
Dr. C. Rigollet

Beoordelingscommissie: Prof. dr. T. Aumann
Prof. dr. H. Löhner
Prof. dr. T. Nilsson

This work is sponsored by the Helmholtzzentrum für Schwerionrforschung GmbH (GSI), Germany - KVI University of Groningen collaboration agreement.

PRINTED BY: GVO drukkers & vormgevers B.V. Ponsen & Looijen

Contents

1	Introduction	1
2	Motivation and theoretical background	5
2.1	NuSTAR at FAIR	6
2.1.1	R^3B	7
2.1.2	HISPEC - DESPEC	10
2.1.3	EXL	12
2.2	Interaction of Radiation with Matter	13
2.2.1	Interaction of photons	14
2.2.2	Interaction of charged particles	16
2.3	Scintillation detectors	18
3	FPGA-embedded modular signal processing	27
3.1	Digital Pulse-Shape Analysis Algorithms	27
3.2	Baseline Follower and $k\sigma$ triggering	30

3.3	Moving Window Deconvolution	34
3.4	Moving Average Filter	39
3.5	Box-trigger	41
3.6	Pile-up Compensation	46
3.7	Developed hardware for R&D towards NuSTAR FEE	53
4	Non-supervised control loops based on local digitized-signal processing	55
4.1	NuSTAR data acquisition	55
4.2	Control systems and self-adjusting control loops	57
4.3	EPICS control system	60
4.4	Realization of a self-adjusting control loop embedded in front-end electronics	66
4.4.1	Device support	68
4.4.2	Peak-sensing algorithm	69
4.4.3	System dynamics	71
4.4.4	Self-adjusting control loop	75
4.4.5	Time aspects/constraints in the self-adjusting control loop	79
5	Overall testing of the signal processing	83
5.1	Results from test measurements performed with a radioactive source	83
5.1.1	Data	84
5.1.2	Energy resolution	84
5.1.3	Peak efficiency	88
5.1.4	Time stamps	91
5.1.5	Multiple channels pile-up compensation	93
5.2	In-beam test measurements	95
5.2.1	Energy calibration	99
5.2.2	Event multiplicity	101
5.2.3	Energy resolution and pile-up to peak ratio	105
6	Summary and conclusions	109

A Abbreviations used in this thesis	113
Nederlandse Samenvatting	115
Acknowledgments	119
References	123

1

Introduction

Within the next decade the new Facility for Antiproton and Ion Research (FAIR) [1] will become one of the largest physics facilities worldwide. FAIR will be built next to the *GSI Helmholtzzentrum für Schwerionenforschung* facility in Darmstadt, Germany [2], taking advantage of the existing GSI accelerators which will be integrated as pre-accelerators. FAIR will provide antiproton and ion beams with unprecedented intensity, higher beam quality and energies, and will allow parallel operation for different experiments. Nuclear physics and astrophysics-related research at FAIR will be organized within the Nuclear STructure, Astrophysics and Reactions (NuSTAR) collaboration [3]. The collaboration is presently setting up a variety of experiments that will benefit from the rare-isotope beams produced by means of the Super-FRagment Separator (Super FRS) [4] to three experimental branches: the high-energy branch, the low-energy branch, and the ring branch.

The high-energy branch focusses on high-energy reactions in inverse kinematics such as: knock-out reactions, break-up reactions, quasi-free scattering, projectile fragmentation, and multi-fragmentation which will employ the complex experimental setup R³B [5].

The low-energy branch will benefit from radioactive ion beams from hydrogen to uranium, with energies ranging from about 3 MeV/u to 150 MeV/u. The main physics topics are the study of the evolution of shell structure and nuclear shapes, the spin structure of the nucleus, transition probabilities and half-lives, particle decay branching ratios, first excited states, and isomeric decays for nuclei far from stability. Examples of experiments at the low-energy branch are the HISPEC/DESPEC [6] projects.

The ring branch will exploit cooled beams that are stored in the storage ring NESR [7]. The main physics topics covered are nuclear masses and lifetimes, charged matter distributions of neutron rich-nuclei near the neutron drip line, single-particle structure evolution (new magic numbers, new shell gaps, spectroscopic factors), NN correlations, new collective modes, in-medium interactions in asymmetric and low-density matter, astrophysical r- and rp-processes. One of the main experiments at the NESR will be EXL [8].

The diversity of physics that will be studied at NuSTAR requires the development and construction of dedicated detector systems (eg. R³B, HISPEC/DESPEC, EXL) and opens a wide range of requirements for data acquisition and controls. In this thesis the focus will be on developments of the Digital Pulse-Shape Analysis (DPSA) embedded in Front-End Electronics (FEE) and slow-controls needed for such systems. The slow-controls system covers functions such as setup and status reporting, calibration, optimization, and run-time controls, involving updating of control parameters, monitoring of systems and environmental parameters. The physics cases as well as the requirements from the Data Acquisition (DAQ) and controls will be outlined in chapter 2. At the moment there is a strong tendency to migrate from the usual analog solutions to fully digital and distributed systems. This allows a more dynamical and broad interaction between the user and the system. It also raises new challenges, since most of the systems are currently running with analog electronics. The newly-designed experimental setups have to be integrated in an environment compatible with the existing analog systems.

The large number of electronics channels with very different requirements will

be one of the challenges for the DAQ. The high rates and large number of channels will lead to an unprecedented amount of information. This implies that fast, online processing of the data should be implemented to extract the desired information from the registered events. In chapter 3 we will discuss the DPSA algorithms that we have implemented on Front-End Electronics (FEE) and tested off-line and in beam in the course of this project. For the implementation of the algorithms a general Trigger and Response Board (TRB) [9] containing a Xilinx Field Programmable Gate Array (FPGA) [10] was developed at the Kernfysisch Versneller Instituut (KVI). The following algorithms, Baseline-follower, Moving Window Deconvolution (MWD), Moving Average Filter (MAF), Box-trigger, and Pile-up Compensation were implemented on the TRB. The implemented algorithms process the signal from its generation to the physics output delivered to the user. Building these algorithms in "building blocks" allows full flexibility and makes adding or removing algorithms into the processing chain possible depending on the needs of a specific signal. We have implemented and tested the pile-up compensation algorithm which offers a complete new approach for dealing with pile-up online. In a traditional way one would identify the pile-up (if possible at all) and reject it. With the pile-up algorithm that we have implemented we not only identify the pile-up but we correct for this effect, thus allowing the use of these data. The challenge and also the main advantage lie in the fact that this correction is done on-line and offers the corrected result to the end user.

In chapter 4 we discuss slow-control aspects such as non-supervised control loops that make use of the local digitized-signal processing. In order to tackle various problems that arise from the requirements set by the very different experiments currently being set up by the NuSTAR collaboration, we need a robust and flexible system. The approach we take on controls should allow for the extension or changes to the solution proposed. Therefore, we have chosen a modular approach in which we build and implement the slow-control methods and DPSA algorithms. The Experimental Physics and Industrial Control System (EPICS) [11] will be introduced and the implementation of non-supervised control loops in EPICS on FEE will be shown. We have used EPICS as a control system because it allows unlimited expansion and it

provides a flexible set of tools to build controls. EPICS was developed in the late 80s to satisfy the needs of small collaborations, but was not restricted in any sense. It was developed based on concepts like distributed control, real-time front-end computers, interactive configuration tools, and workstation-based operator consoles. Since its functionality is based on communication protocols at every level, it permits the integration of newly available technologies, such as VME [12], VXI etc. Proving its flexibility and reliability, EPICS has grown into a huge collaboration creating tools that allow its users to build and further extend its capabilities to suit their needs.

In several performance studies the functionality of the DPSA algorithms has been verified, off-line at KVI as well as in-beam at GSI. For the in-beam experiment performed at GSI the aforementioned algorithms were implemented and tested on the SIS3302 [13] board manufactured by STRUCK [14]. The analysis and results of these experiments are presented in chapter 5. Finally, a summary of the work and some outlook are given in chapter 6.

2

Motivation and theoretical background

The Facility for Antiproton and Ion Research (FAIR) [1, 15] will provide a wide range of high-energy and high-intensity radioactive ion beams, high intensity antiprotons and high-energy heavy-ions. The new facility will provide opportunities to investigate a broad range of science including nuclear structure, hadronic, relativistic heavy ion, plasma and atomic physics.

This chapter introduces the next generation of detector systems that will be used in the NuSTAR project (Nuclear STructure Astrophysics and Reactions) [3]. A short overview of the main experiments that will be performed using radioactive ion beams with high energy (R^3B [5, 16]), low-energy (HISPEC/DESPEC [6]) and in the storage ring (EXL [8]) will be presented. Such a wide range of physics requires the detection of a variety of elementary particles and nuclear fragments. The interaction of photons, charged particles and neutrons with matter are, therefore, also reviewed in this chapter. The third section contains the general properties of detectors, such as detector response, energy resolution, sensitivity, efficiency, response time and dead time. The last section discusses the main properties of scintillation detectors and

ionization detectors, which have been used in experiments discussed in this thesis.

2.1 NuSTAR at FAIR

Nuclear reactions are powerful tools in nuclear structure and astrophysics studies as they can probe the matter deep into the heart of the nucleus or just at its surface, depending on the type and energy of the radioactive ion beams. Nuclei far from stability, characterized by a large asymmetry in proton (Z) and neutron (N) numbers will provide stringent test grounds for existing nuclear structure and nuclear astrophysics models, that have reached their limits of validity when applied to nuclei far from stability.

Figure 2.1 shows the layout of the existing facility at GSI [2] that comprises the linear accelerator UNILAC [17] and the heavy ion synchrotron SIS [18], as well as the FAIR [1] facility presently under construction. The existing accelerator facility will be complemented by four cooler/storage rings: the two stage synchrotron SIS100/300, a collector ring (CR) for the collection and stochastic cooling of radioactive ion or antiproton beams from production targets, a new experimental storage ring (NESR) serving as an accumulator and storage ring for radioactive ions, and a high-energy storage ring (HESR) for antiprotons with energies up to 14 GeV. The main experiments at FAIR are: PANDA [19], NuSTAR [3], CBM [20] and APPA [21].

The Nuclear Structure, Astrophysics and Reactions (NuSTAR) collaboration gathers all experiments that will be benefiting from the unique possibilities opened up through the Super-FRS, which will deliver an unprecedented range of radioactive ion beams (RIBs). The experiments will exploit beams of different energies and characteristics at three branches (see Fig. 2.2): the high-energy branch utilizes the RIBs at relativistic energies (300-1500 MeV/u) as created in the production process, the low-energy branch aims at using beams up to 150 MeV/u, whereas the ring branch will exploit cooled and stored beams in the storage ring NESR [7].

The High-Energy Branch will contain a complex detector setup (R^3B) around a large-acceptance bending magnet for kinematically-complete experiments on nuclear structure and reaction physics up to the highest available energies. At the Low-

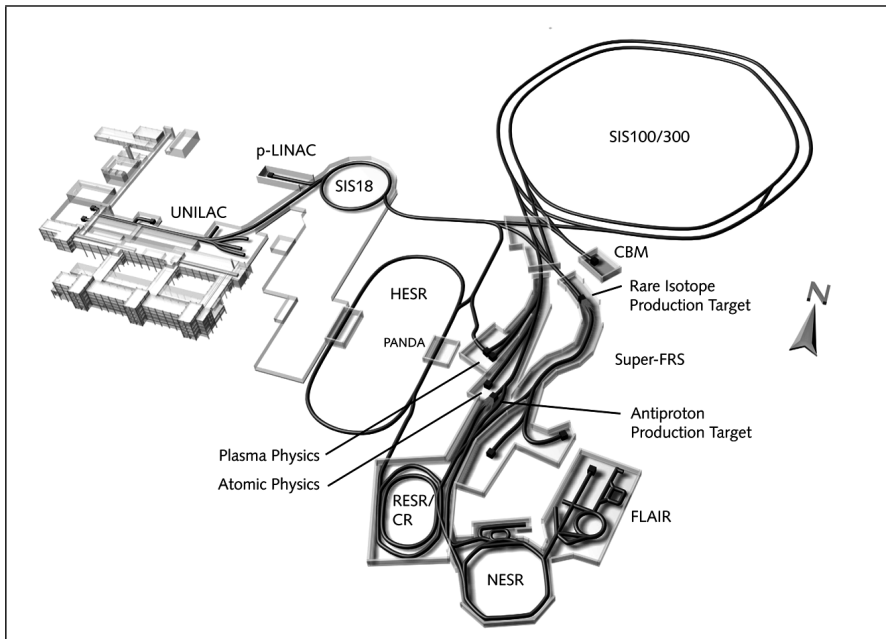


Figure 2.1: The existing GSI facility and the future FAIR facility in Darmstadt.

Energy Branch the high-energy beams are slowed down by an energy buncher system and are stopped in a gas cell for decay spectroscopy, for trap experiments, and laser spectroscopy. Alternatively, the low-energy beams can be directed to a dedicated setup for spectroscopy and reaction studies, where detailed information on very short-lived nuclei (with lifetimes in the μs scale) can be obtained. HISPEC-DESPEC will be further discussed as an example from this branch. The Ring Branch consists of a storage ring system in which ions can be stored and cooled for mass and lifetime measurements as well as scattering experiments, performed in the EXL setup. A detailed description of the physics topics covered by the NuSTAR experiments is given in [15, 22].

2.1.1 R³B

R³B will cover experimental reaction studies with exotic nuclei far off stability, with emphasis on nuclear structure and dynamics. The main physic topics covered are:

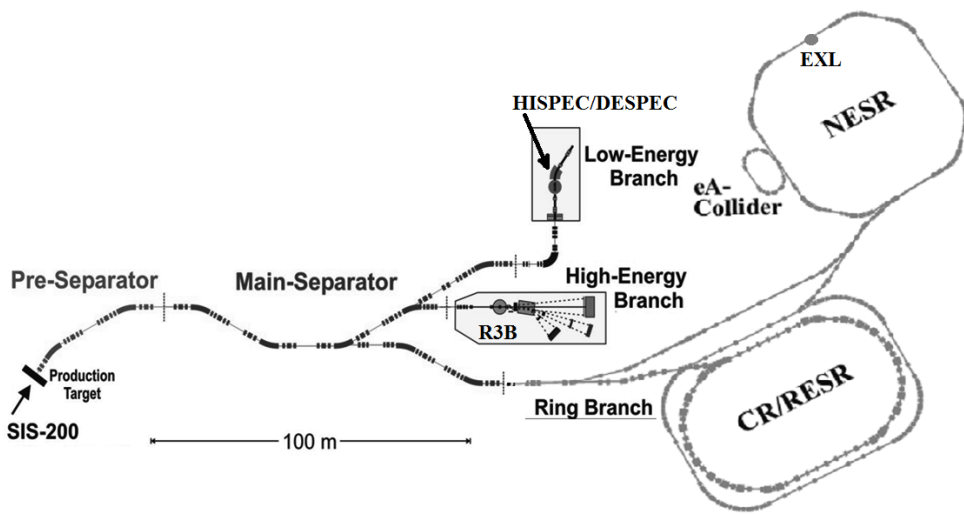


Figure 2.2: The Super-FRS including the Pre-Separator and the Main-Separator, with the three branches, the Low-Energy Branch, the High-Energy Branch and Ring Branch. The locations of all experiments are indicated.

knockout reactions, quasi-free scattering, projectile fragmentation and multifragmentation. The experimental setup is adapted to the highest beam energies delivered by the Super-FRS. A schematic view of the R^3B experimental setup is shown in Fig. 2.3. The R^3B setup consists of: tracking detectors (for protons and fragments), a γ -ray spectrometer, a target recoil detector, a large-acceptance dipole, a high-resolution spectrometer, two large-area Time of Flight (ToF) walls for charged particles, and a neutron ToF spectrometer. The incoming beam will be tracked (starting from the dispersive focus at the Super-FRS) in order to determine its momentum, angle of incidence and position on the target. The particles emerging from the interaction zone are tracked in a similar way by the spectrometer behind the target.

Figure 2.3 shows that the target is surrounded by a γ -ray spectrometer, followed by a Čerenkov detector. For most of the experiments, a high efficiency total γ -absorption spectrometer (some of the materials considered are cooled scintillators made of undoped CsI or NaI) is the optimum solution, which may also be used to

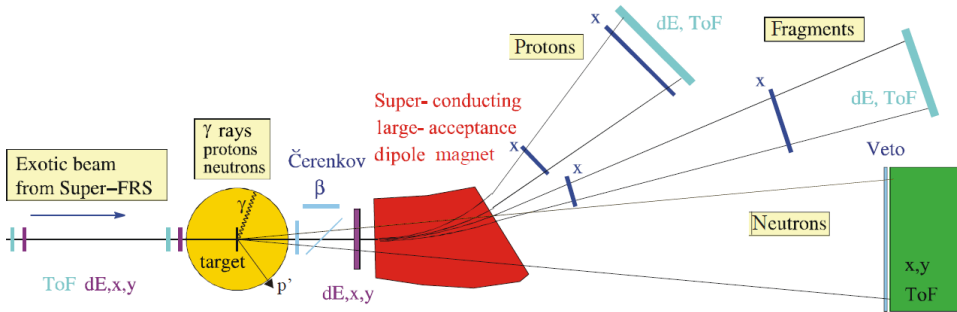


Figure 2.3: Schematic drawing of the R³B experimental setup (not to scale). The incoming secondary beam is identified by measuring its magnetic rigidity, energy loss dE and time-of-flight ToF. Behind the target, the kinematically forward-focused reaction products are identified and momentum analyzed.

measure the energy of recoiling protons. It is desired to obtain a photo-peak efficiency $\epsilon > 50\%$ (at $E_{\gamma}^{lab} = 10$ MeV) with a γ -energy resolution of 2%. For specific experiments requiring high energy resolution for γ -detection, the alternative Germanium spectrometer AGATA [23] might replace the γ -ray spectrometer. Employing half of the AGATA detectors in a compact arrangement covering the angular range from 9° to 45° at a target distance of 50 cm will result in a photo-peak efficiency $\epsilon \approx 12\%$ (for $E_{\gamma}^{lab} = 3$ MeV).

The number of channels to be read out by the electronics is in the order of thousands. The total amount of data expected per second is in the order of 10-100 MBytes/s. This implies that the total amount of data per day is in the order of 1-10 TBytes. This requires that intelligent triggers will be implemented into the Front-End electronics in order to record only the desired events. One may consider to use different parts of the data stream at different locations to perform different tasks: mass storage, online analysis, slow control feedback. The slow controls of the experiment or setup have to be implemented in such a way to allow the continuous adjustment of parameter settings without manual interference.

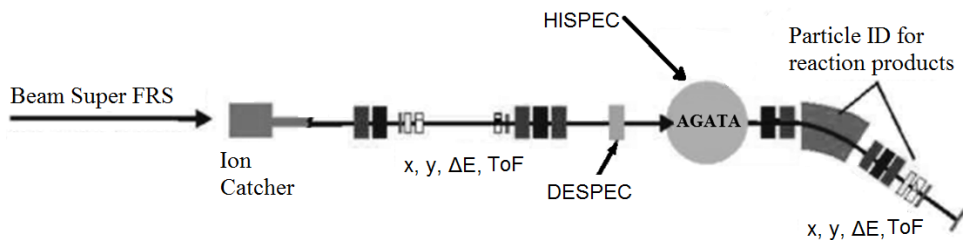


Figure 2.4: Schematic drawing of the HISPEC and DESPEC experimental setups. The HISPEC experimental setup consists of detectors for beam tracking and particle identification, the AGATA gamma-ray spectrometer, devices for precision lifetime measurements, a ToF-dE-E detector system for particle identification, and a large acceptance magnetic spectrometer with tagging detectors in the focal plane. The main components of the DESPEC setup are the implantation double-sided silicon-strip detector (DSSD), a high resolution γ -detection array, and a modular neutron detector array.

2.1.2 HISPEC - DESPEC

The HISPEC/DESPEC experiments will be located at the low-energy branch of the Super-FRS. Several thousands of isotope beams, ranging from hydrogen to uranium, will be available with energies up to 150 MeV/u.

The HISPEC and DESPEC experiments will have several concurrently running data-acquisition systems, each of them serving different detector subsystems. Experiences in using data-acquisition systems for high resolution in-flight spectroscopy have recently been gained at the RISING setup [24]. The beam tracking and identification detector subsystem, which is part of the beam line of the Low-Energy-Branch of the Super-FRS will use the standard NuSTAR data-acquisition system. The estimated count rate of these detectors is up to 10 MHz, with up to 100 parameters to be read out in each event. The amount of data expected per second is 0.1 - 1 GBytes/s which results in 1 - 10 TBytes/day.

Figure 2.4 is a schematic view of the HISPEC/DESPEC experimental setups. The HISPEC setup consists of detectors for beam tracking and particle identification, the AGATA gamma-ray spectrometer [23], devices for precision lifetime measurements,

a ToF- dE/E detector system for particle identification after the secondary target, and a large acceptance magnetic spectrometer with tagging detectors in the focal plane. The main components of the DESPEC experimental setup are the implantation double-sided silicon-strip detector (AIDA [25]), a high-resolution γ -detection array, and a modular neutron detector array.

The various detector subsystems located around and downstream of the secondary target position will use their own dedicated data-acquisition systems. Most of these systems will be built specifically for HISPEC-DESPEC, while others will use systems that need to be integrated into the HISPEC-DESPEC setup. The counting rates and data rates of the detector subsystems around and behind the secondary target will vary considerably ($10^4 - 10^7$ Hz) depending on the type of experiment.

Each detector subsystem will have its own time stamp, which is needed to correlate the data from the different subsystems. Some of the detector subsystems will produce and use a local trigger signal, which is used for that particular subsystem. Other subsystems will run totally triggerless in so-called total data read-out mode. In this case each piece of data stored will have a time stamp attached, that will later be used for the reconstruction of the event.

The on-line monitoring and analysis will almost be as complex as the later off-line analysis. Most of the front-end electronics for various detector subsystems will be fully digital, i.e. the preamplifier or photomultiplier signals will be digitized and pre-processed by hardware and software located near the detector. The controls for these systems will be developed in the framework of the NuSTAR controls. Also there is the need to design systems for slow control and monitoring of detector bias, heat and power consumption of detectors and electronics, etc. The digital data will then be transmitted optically to the data-acquisition systems. The number of channels to be read from the target area alone is in the order of ten thousands. The details about each detector subsystem and their functionality can be found in [6].

2.1.3 EXL

The EXotic Nuclei Studied in Light-Ion Induced Reactions (EXL) setup is located at the NESR storage ring. The main focus of the EXL collaboration is the study of the structure of exotic nuclei in light-ion scattering experiments at intermediate energies (typical energies considered are in the range of 100 - 700 MeV/u) using inverse kinematics on light stable target nuclei. The main physics topics covered are the study of the matter distribution of neutron-rich nuclei near the neutron drip line (halo, skin, ...), the study of the shell structure in nuclei of extreme proton-to-neutron asymmetry (new magic numbers, spectroscopic factors), NN correlations, pairing and clusterization phenomena, new collective modes (different deformations for p and n, giant resonance strength), in-medium interactions in asymmetric and low-density matter, and astrophysical r- and rp-processes.

The experiment is based on the complete reconstruction of light-ion induced direct reactions in inverse kinematics making use of novel storage ring techniques. The gas-jet target will be placed in the storage ring, while using stored exotic nuclei far from the valley of stability as projectiles. A schematic view of the EXL setup can be seen in Fig. 2.5. It comprises a silicon target-recoil detector for charged particles, completed by a calorimeter, located around the internal gas-jet target, forward detectors for fast ejectiles (both charged particles and neutrons) and an in-ring heavy-ion spectrometer.

The number of channels that need to be read and controlled in EXL is around half a million and the information to be stored is in the order of 0.1 to 0.5 GBytes/s. In EXL, the information given by detectors placed in different physical locations will be used to reconstruct the same event. Generally, the recoil detector will be the first to register an event, then the ejectile detectors and finally the heavy ion spectrometer will observe the same event. Each event will be reconstructed based on its time stamp. As already stated, some of the EXL detectors will be placed inside the ultra high vacuum part of the storage ring. Due to their inaccessibility and also the large number of channels, a self-adjusting and self-monitoring system is needed. More details on slow control and the functionality of such a system are given in chapter 4.

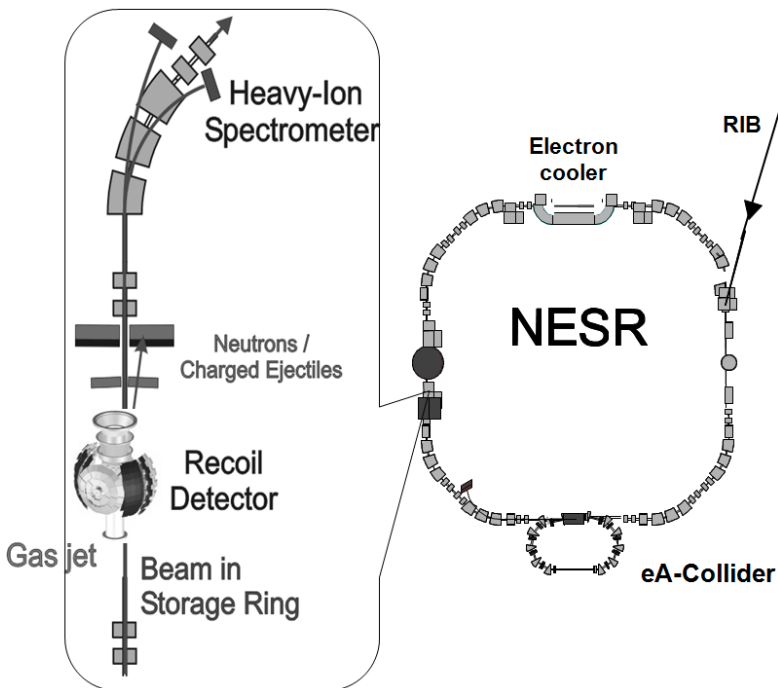


Figure 2.5: Schematic view of the EXL detection system, built into the NESR storage ring. It consists of a silicon target-recoil detector for charged particles, completed by a calorimeter, located around the internal gas-jet target, forward detectors for fast ejectiles (both charged particles and neutrons) and an in-ring heavy-ion spectrometer.

2.2 Interaction of Radiation with Matter

Radiation is detected by its interaction with matter. Thus, the detection of particles starts always with the interaction of the particles with the detector medium. As a result, part of the energy of the radiation is deposited inside the detector material and transformed into an electrical signal, which is read out and recorded. The fundamental mechanism, on which radiation detectors are based, is the dissipation (of a fraction) of the incoming radiation-energy inside the detecting material. The transferred energy is distributed among carriers and transformed into the signal (e.g. electrons-holes in semiconductors, ion pairs in gaseous devices, photons in scintillating media). This signal is further processed by appropriate readout elements, like

front-end electronics for semiconductor detectors and for gaseous devices, or photomultipliers for scintillating materials. The type of interaction process that takes place inside the detector depends on both the type and the energy of the incoming particles. As a consequence, the required information that characterizes the incoming particle (energy, charge, particle identification) can be obtained. In case of FAIR experiments, the energy of charged particles ranges from fractions of keV to 10^{10} eV. The detecting materials to be used in a particular application have to be carefully selected for a specific particle type and energy. In the following section we will cover the main types of radiation encountered in nuclear spectroscopy and their interaction processes with matter. For more details we refer to [26, 27, 28].

2.2.1 Interaction of photons

The main three mechanisms through which a photon interacts with matter and which provide the largest contributions to the total cross section are: the photoelectric effect, in which the interaction occurs with the entire atomic electron cloud and which results in the complete absorption of the primary photon energy; Compton scattering on atomic electrons at such photon energies that the electron binding energies can be neglected and electrons can be treated as quasi free; pair production, in which the energy of the incoming photon is high enough to allow the creation of an electron-positron pair in the Coulomb field of an electron or a nucleus. The importance of each process depends on the energy of the incoming photon as well as the atomic number of the media.

The photoelectric process dominates at low energies (i.e., below 50 keV for aluminum and 500 keV for lead absorber). As the energy increases (between 0.05 and 15 MeV for aluminum and between 0.5 and 5 MeV for lead) the main contribution to the attenuation coefficient comes from Compton scattering. At larger photon energies, electron-positron pair production becomes the dominant mechanism of photon interaction with matter. The photon can be elastically scattered or absorbed by the nucleus. However, this kind of process is not easily treated for systematic calculations due to its dependence on A and Z , and the sensitivity to the isotopic abundance.

In the photoelectric effect, a gamma ray enters the Coulomb field of an atom and transfers its entire energy to a bound electron causing ionization. The electron is subsequently ejected from the atom with a kinetic energy equal to the difference between the gamma ray energy and the binding energy of the ejected photoelectron. The cross section for the photoelectric effect can be calculated as a function of atomic number and photon energy as shown in [28]. For energies of the incoming photon that are large compared with the ionization energy of the K-shell electrons, the Born approximation can be used to calculate the cross section for the interaction of a photon with an electron from the K-shell $\sigma_{k,B}$:

$$\sigma_{k,B} = \sigma_{Th} 4\sqrt{2} \frac{Z^5}{137^4} \left(\frac{m_e c^2}{h\nu} \right)^{\frac{7}{2}}, \quad (2.1)$$

where $\sigma_{Th} = \frac{8}{3} \pi r_e^2 \simeq 6.65 \times 10^{-25} \text{ cm}^2$ is the classical Thomson scattering cross section, Z is the atomic number of the nucleus, m_e is the rest mass of the electron, and $h\nu$ is the energy of the incoming photon. As can be seen from Eq. 2.1, higher atomic numbers Z cause larger cross sections for the photoelectric effect. The photoelectric cross section decreases with increasing photon energy. For heavy elements or for incoming photon energies close to the ionization energy of electrons of K, L, M, ... shells, the Born approximation is no longer valid and exact calculations of wave functions must be used.

The Compton effect is based on the corpuscular behavior of the incident radiation and it is an incoherent scattering process on individual atomic electrons. These electrons can be described as quasi-free since to a first approximation their binding energies can be neglected with respect to the energy of the photon. The electron is knocked out resulting in a recoil electron and the incident photon is scattered into an angle θ between 0° and 180° with respect to its original direction. The energy transferred to the electron can vary from zero to a large fraction of the photon energy. The cross section of Compton phenomena decreases as a function of energy and is directly proportional to the electron concentration in the atom. The cross section for Compton scattering on quasi-free electrons was first calculated by Klein and Nishina (1929) [29]. Their calculation yields the differential cross section for Compton scat-

tering of an unpolarized photon on a quasi-free electron:

$$\frac{d\sigma}{d\Omega} = Z r_e^2 \left(\frac{1 + \cos^2 \theta}{2 [1 + \alpha(1 - \cos \theta)]^2} \right) \left(1 + \frac{\alpha^2 (1 - \cos \theta)^2}{(1 + \cos^2 \theta)[1 + \alpha(1 - \cos \theta)]} \right), \quad (2.2)$$

where $\alpha = \frac{E_\gamma}{m_e c^2}$, E_γ is the energy of the incoming photon, r_e is the classical electron radius and θ is the scattering angle.

If the incoming photon energy exceeds 1.022 MeV, which is twice the energy corresponding to the electron rest mass, the production of an electron positron pair becomes possible. The process of pair production occurs close to a charged massive object (for instance a nucleus) which takes away the amount of momentum needed to conserve the total momentum during the interaction with the Coulomb field of the massive object itself. The pair production process becomes the dominant mechanism for photon interactions in matter for incident photon energies larger than ~ 5 MeV and accounts for almost the whole γ -ray absorption in this energy range.

Figure 2.6 shows the relative importance of the three major interaction processes of gamma radiation for different photon energies and different absorber materials. The left curve represents the energy for which the photoelectric effect is equally probable to the Compton scattering as a function of the absorber atomic number. The curve on the right represents the energy for which Compton scattering and pair production are equally probable as a function of the absorber atomic number.

2.2.2 Interaction of charged particles

The interaction with a medium causes a continuous energy loss of the impinging charged particle which is degraded from its original energy E and possibly stopped inside the material. The principal mechanism leading to energy loss is the Coulomb interaction between the particle and the negative charge cloud of the orbital electrons of the absorber atoms. Other mechanisms, depending on the particle type, like electromagnetic or strong interactions with the nuclei are also present. The energy transferred from the particle to the absorber can be so low to only excite atoms and/or molecules (excitation processes) or high enough to produce ionization. The energy

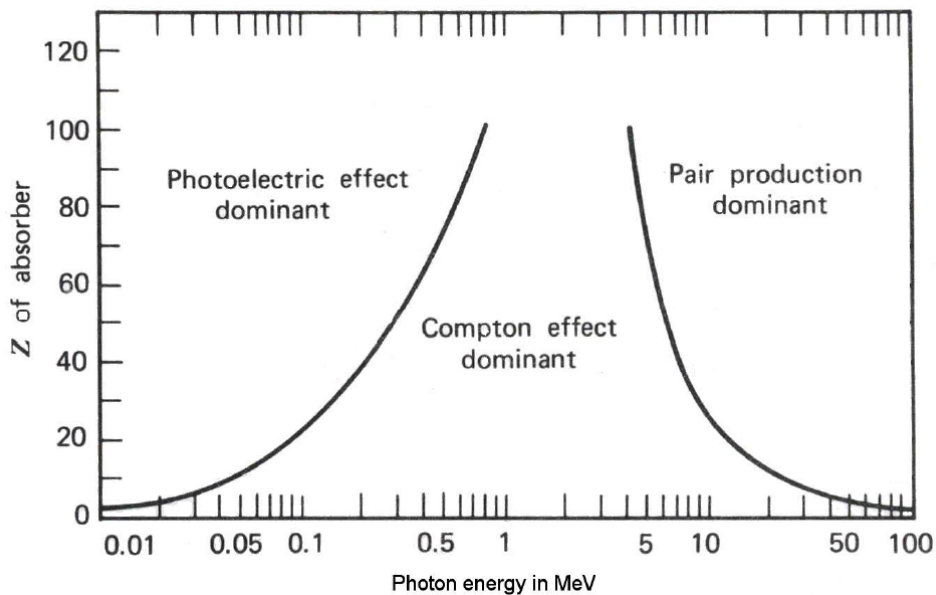


Figure 2.6: The relative probability of the photoelectric effect, Compton scattering and pair production as a function of energy and absorber atomic number [27]. The left curve represents the energy for which the photoelectric effect is equally probable to the Compton scattering as a function of the absorber atomic number. The curve on the right represents the energy for which the Compton scattering and pair production are equally probable as a function of absorber atomic number.

deposited in the detector can thus be obtained either through atomic/molecular excited states, which subsequently de-excite with the emission of low-energy photons, or through the creation of electron-ion pairs (electron-hole pairs in semiconductors) resulting from the ionization processes.

For an incoming heavy charged particle of mass $M \gg m_e$, velocity $v = \beta c$, charge $z e$, the theoretical expression for the energy loss by collision, $\frac{dE}{dx}$, is given by the energy-loss formula, also known as the Bethe-Bloch formula [30, 31, 32]:

$$-\frac{dE}{dx} = \frac{2\pi n z^2 e^4}{m_e v^2} \left\{ \ln \left[\frac{2 m_e v^2 W_m}{I^2(1 - \beta^2)} \right] - 2\beta^2 - \delta - U \right\}, \quad (2.3)$$

where m_e is the electron mass, $n \propto \frac{Z\rho}{A}$ is the number of electrons per cm^3 of the

material, ρ is the density of the material, I is the mean excitation energy of the atoms of the material, normally treated as an experimentally determined value for each element, W_m is the maximum transferable energy from the incident particle to atomic electrons, δ is the correction for the density-effect, and U is the term related to the non-participation of electrons of inner shells (K, L) for very low incoming kinetic energies (the shell correction term). W_m takes the expression:

$$W_m = 2m_e c^2 \frac{\beta^2}{1 - \beta^2} \left[1 + \left(\frac{m_e}{M} \right)^2 + 2 \frac{1}{\sqrt{1 - \beta^2}} \frac{m_e}{M} \right]^{-1}. \quad (2.4)$$

The energy loss increases with the charge $z e$ of the incoming particle and also with the number of electrons per cm^3 of the material. Therefore, materials with high density and high atomic numbers have a larger stopping power than materials with low atomic numbers and low density.

2.3 Scintillation detectors

Scintillators are materials in which the energy loss of impinging particles is transformed into photons close to or in the visible range. Radiation detection systems based on scintillation detectors commonly consist of four main components: a scintillator (the sensitive volume of the detector), an optical coupling system, a photomultiplier tube (PMT), and signal processing electronics as shown in Fig. 2.7.

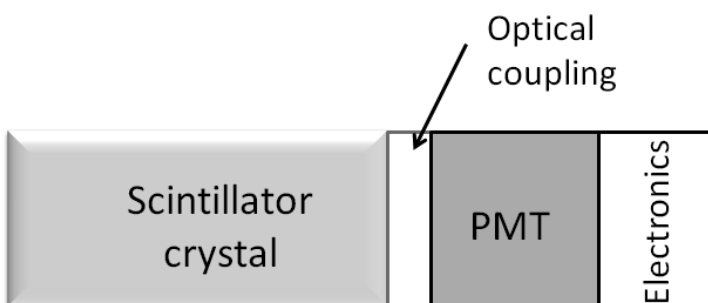


Figure 2.7: Schematic view of a scintillator coupled to a photomultiplier tube.

There are significant differences in the scintillation process between inorganic and organic scintillators. In inorganic impurity-activated crystals, the scintillation emission is mainly characteristic of the luminescence centres. The result of energy dissipation from a particle passing through a crystal is the production of electron-hole pairs.

In organic scintillators luminescence is associated with conjugated and aromatic organic molecules, which form molecular liquids or crystals in which the molecules are bound together by Van der Waals forces and retain their individual identity, electronic structure and luminescence. The origin of the main scintillation emission, i.e. the medium-fast component, is the excitation of π -electron excited singlet states [33].

Although the mechanism that leads to the emission of scintillation light is different from one material to the other, it can be summarized to be the excitation of molecular states from the ground state to one or more excited states whose decay leads to the emission of light. The lifetime τ_i of these states characterizes the exponential decay of the light output of the scintillator. The component that contains the largest part of the emitted light is called the main component. The fraction of light contained in each component may vary with the temperature of the material [34, 35].

By definition, the scintillation light response L is

$$L = S E, \quad (2.5)$$

where E is the particle energy dissipated in the scintillator and S is the absolute scintillation efficiency. Relation 2.5 is valid to a good approximation in inorganic scintillators. Due to the quenching effect, for organic scintillators, the relation between the emitted light and the energy deposited by an ionizing particle is not linear. In this case, the scintillator response depends also on the type of particle and its specific ionization. The dependence of the light emission with respect to the path x within the scintillator is

$$\begin{aligned} \frac{dL}{dx} &= -S \frac{dE}{dx}, && \text{inorganic scintillators} \\ \frac{dL}{dx} &= \frac{S(-\frac{dE}{dx})}{1+KB(-\frac{dE}{dx})}, && \text{organic scintillators} \end{aligned} \quad (2.6)$$

where K is the quenching parameter and B is a constant. The second line of Eq. 2.6 is known as Birks' Law [36]. The rise time of the photon emission, depending on the

rate dL/dt of the scintillation response is defined as the time during which dL/dt is increased from 10% to 90% [33]. One can write down the equation describing the variation of the scintillator response with time

$$\frac{dL}{dt} = \frac{dL}{dx} \frac{dx}{dt}. \quad (2.7)$$

For a charged particle, the energy loss in the medium is given by the Bethe-Bloch formula. If this particle, with a rest mass M ($\gg m_e$), is traveling at nonrelativistic speed, the energy dE transferred as excitation and ionization along an element of path dx described by the Bethe-Bloch formula can be parameterized to a good approximation by

$$\frac{dE}{dx} = \frac{C}{E}, \quad (2.8)$$

where C is a constant that characterizes both the stopping element and the charged particle. The scintillator light pulse of the photon emission in inorganic and organic scintillators is described by [33]

$$\begin{aligned} \frac{dL}{dt} &= \frac{\sqrt{2}CS}{\sqrt{M}\sqrt{E}}, && \text{for inorganic scintillator;} \\ \frac{dL}{dt} &= \frac{\sqrt{2}CS\sqrt{E}}{\sqrt{M}(E+KBC)}, && \text{for organic scintillator.} \end{aligned} \quad (2.9)$$

It can be seen that the rise time of the scintillator light pulse depends on the energy of the incoming particle. For inorganic scintillators, dL/dt increases as E decreases. Making use of Eq. 2.9, typical rise times for different materials and incident particles and energy are calculated to be in the order of ps [33]. For inorganic scintillators the light pulse behaves like $L(t) \propto t^{\frac{2}{3}}$. However, this approximation breaks down at very low energies at the end of the particle range in the medium, when the charged particle deposits almost all its energy. At this point, the light pulse increases sharply [33].

The shape of the scintillation light pulse $L(t)$ is characterized by a fast rise time of the order of ps and a decay time of the order of 100 ns. The scintillator light pulse can be described, as a function of time, by

$$L(t) = \begin{cases} \sum_i L_i e^{-\frac{t}{\tau_i}} - L e^{-\frac{t}{\tau_R}}, & t > 0 \\ 0, & t < 0 \end{cases} \quad (2.10)$$

Table 2.1: General properties of the most commonly used inorganic scintillators.

	NaI(Tl)	CsI
Density (g/cm ³)	3.67	4.51
Radiation Length (cm)	2.59	1.85
Decay Time (ns)	230	630
Peak Emission (nm)	415	420
Refractive index at peak emission	1.85	1.84
Light Yield (vs. NaI(Tl))	1	0.85
Hygroscopic	Yes	Slightly

where L_i and τ_i are the initial intensity and characteristic time of the i -th exponential component, τ_R is the characteristic constant of the rise time and L is the total intensity [35].

Table 2.1 summarizes the values of decay constants and light yields for the crystals we have used in various measurements. It also shows that the maximum of the spectral emission for the materials presented takes place around 400 - 550 nm, a range which overlaps with the spectral sensitivity domain of standard photocathodes.

Photons which strike the PMT's photocathode eject an electron by the photoelectric effect. This electron is accelerated towards the first dynode by a DC potential of 100 to 200 V. Secondary electrons are ejected when the electron strikes the first dynode, and these electrons are subsequently accelerated towards the second dynode. Typically, the process continues for a number of n dynodes (typically $n= 8$ to 14), each providing an electron gain $\delta \approx 4$ to 5, producing 10^5 to 10^9 electrons which are collected by the anode.

Figure 2.8 shows the diagram and working principle of the photomultiplier tube. If the voltage between each pair of dynodes is the same, the output charge for each electron leaving the cathode is just $\delta^n e$ for a n -stage tube. Writing the gain as being $G = (\delta)^n$ the output charge for N photoelectrons is $q = GNe$ [38]. Problems due to space-charge effects which, particularly if N is large, may arise in the latter stages of the tube, are ignored in this treatment, as are effects due to the finite transit times of

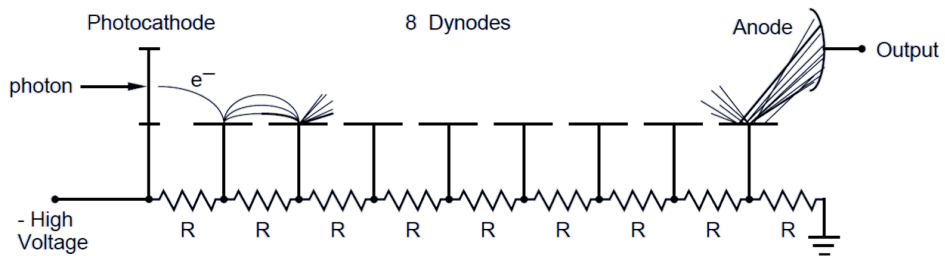


Figure 2.8: Schematic view of a photomultiplier tube, from [37]. Photons which strike the PMT's photocathode eject an electron by the photoelectric effect. This electron is accelerated towards the first dynode by a DC potential of 100 to 200 V.

the electron. The transit time is the interval between the arrival of a light pulse at the photocathode and the appearance of the output pulse. As can be seen from Fig. 2.8, most of the PMT output current is drawn from the last dynodes, which will lead to a voltage drop across the last dynodes as compared to the first ones. This effect is seen in Fig. 2.9, where it can be seen that in the presence of the photocurrent, the voltage across the dynodes is not linearly distributed anymore. If the incident level is increased further so that the anode current becomes very large, the current collection efficiency of the anode drops leading to saturation. In this case, the output signal is not proportional to the deposited energy inside the detector. This can be prevented by replacing the last resistors in Fig. 2.8 with Zener diodes coupled to fast capacitors, as seen in Fig. 2.10. As long as there is some reverse current through a Zener diode, the voltage across the diodes is nearly constant. This will prevent the voltage on these stages from dropping as the output current is increased.

An electron can be emitted from the photocathode or from the dynode surface in any direction, leading to fluctuations in the transit time. These fluctuations are called transit time spread (TTS). The standard deviation of the TTS decreases with the number of photoelectrons, and typical values for most commonly used PMTs are a few ns for a single photoelectron/pulse and 100 ps for 100 photoelectrons/pulse [37]. If the transit time is described by the function $g(t)$ and the PMT has not reached

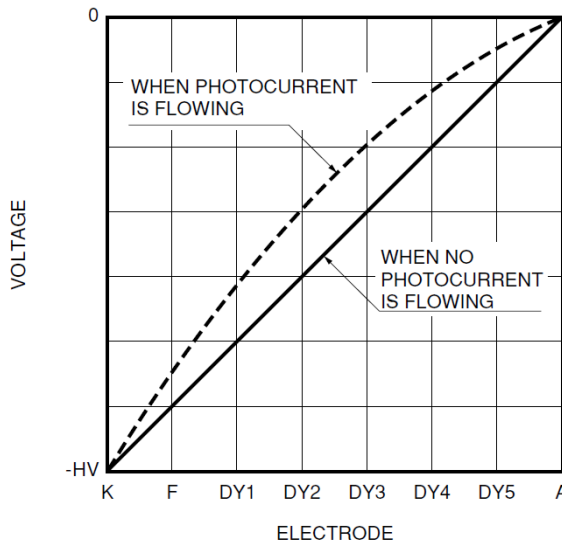


Figure 2.9: Influence of photocurrent on voltage applied to each dynode [37]. *K* is the cathode, *F* the focusing electrode, *DY1* - *DY5* represent the dynodes, and *A* is the anode.

saturation, the output signal at the anode can be written as

$$i(t) = \int_0^t G N e \left(\sum_i \frac{f_i}{\tau_i} e^{-\frac{t'}{\tau_i}} - \frac{1}{\tau_R} e^{-\frac{t'}{\tau_R}} \right) g(t-t') dt, \quad (2.11)$$

where G is the gain of the photomultiplier tube, N is the total number of electrons emitted by the photocathode, e is the charge of the electron, f_i is the fraction of light contained in each decay mode, τ_i is the decay constant of each component of the scintillator light and τ_R is the characteristic constant of the rise time of the scintillator light pulse. From an electrical point of view, the photomultiplier can be reduced to a current generator in parallel with a resistance R and a capacity C . The differential equation that describes the output voltage takes the form

$$\frac{dV}{dt} + \frac{1}{RC} V = i(t), \quad (2.12)$$

with the initial condition $V(t=0) = 0$, where $i(t)$ is the output current at the anode.

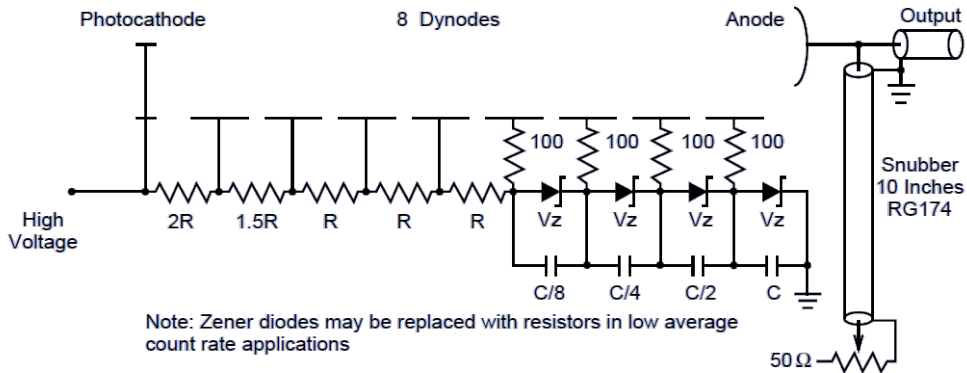


Figure 2.10: Alternative scheme of a photomultiplier tube optimized for pulse-shape stability. In order to improve the linearity of the output, the last resistors are replaced by Zener diodes. As long as there is some reverse current through a Zener diode, the voltage across the diodes is nearly constant. This will prevent the voltage on these stages from dropping as the output current is increased [37].

The general solution of the first-order linear differential equation is:

$$V(t) = \frac{\int e^{\frac{t}{\tau_p}} i(t) dt + C}{e^{\frac{t}{\tau_p}}}, \quad (2.13)$$

where $\tau_p = RC$ and C is a constant chosen such that it matches the initial condition.

Assuming that the scintillator light pulse has a single component with a decay time τ , the rise time of the scintillator light pulse is very small and the transit time spread is negligible, the output pulse-shape takes the form

$$V(t) = \begin{cases} \frac{GNeR}{\tau - \tau_p} \left[e^{-\frac{t}{\tau}} - e^{-\frac{t}{\tau_p}} \right], & \tau \neq \tau_p \\ \frac{GNeR}{\tau^2} t e^{-\frac{t}{\tau}}, & \tau = \tau_p \end{cases}. \quad (2.14)$$

If $\tau_p \gg \tau$, the amplification is large and the decay time of the pulse is given by the τ_p of the photomultiplier circuit. If $\tau_p \ll \tau$, the amplification is small and the decay time of the pulse is given by the decay time in the scintillator. Figure 2.11 shows a typical voltage pulse from the preamplifier as collected from a NaI(Tl) detector coupled to a Hamamatsu R877 PMT [39].

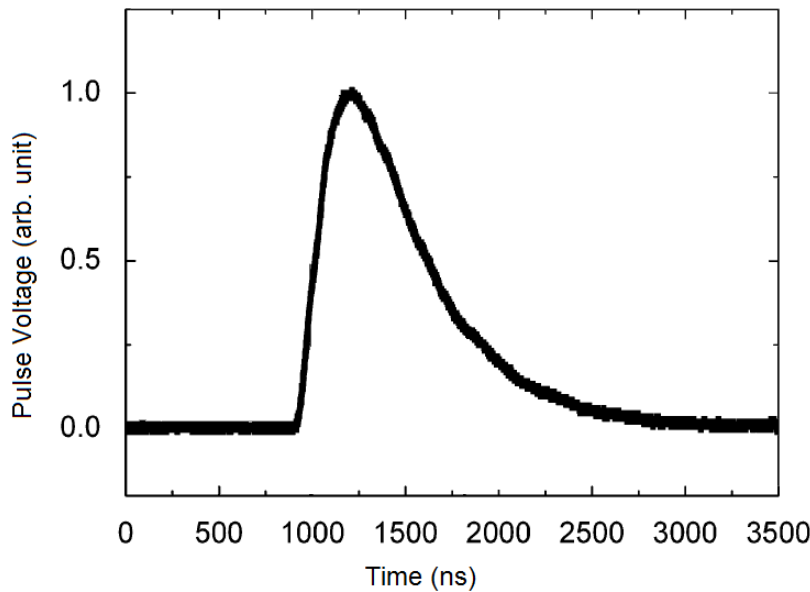


Figure 2.11: Typical voltage pulse from the preamplifier as collected from a NaI(Tl) detector coupled to a Hamamatsu R877 PMT [39].

If the signal pulse repetition rate increases and multiple pulses enter the measuring system, these pulses are added together to create a large pulse. This problem is called pile-up. For this problem, we have developed a scheme, discussed in the next chapter, to recover the original amplitudes.

3

FPGA-embedded modular signal processing

3.1 Digital Pulse-Shape Analysis Algorithms

In order to improve the performance of detector systems and to add new features, we have studied and developed new methods of applying pulse-shape analysis. Taking into account the various specifications and requirements of the NuSTAR detectors, we have implemented several algorithms, organized as independent interconnected modules, that deal with the digitized signal, in a real-time environment. The modular approach allows us to turn on and off any of the implemented modules.

Each of the modules consists of a specific algorithm, which will be presented in more detail later on in this chapter: baseline follower, $k\sigma$ triggering, moving window deconvolution, moving average filter, box-trigger, and pile-up compensation. Apart from the known moving window deconvolution and moving average filter, the pile-up compensation method brings a new approach in dealing with the pile-up.

A typical digitized signal is affected by both noise and a baseline that may be

fluctuating over time. Therefore, we have implemented a baseline follower to correct for the baseline value at each given time during the measurement. The baseline follower uses a pre-triggering module, the $k\sigma$ triggering (see section 3.2), in order to prevent the value of the baseline to be affected by the occurrence of a pulse. If the incoming rate of the radiation on the detector is high, then the measured spectra are affected by pile-up. To prevent this problem, we have implemented a pile-up compensation algorithm that requires at input the values of the digitized signal amplitudes that are affected by pile-up and the time stamps of the pulses and returns the value of the corrected amplitude. This amplitude value is obtained using two filters: a moving window deconvolution and a moving average. In order to get the time stamps we have implemented the box trigger.

We have tested our Digital Pulse-Shape Analysis (DPSA) on CsI scintillation detectors and HPGe detectors. Figures 3.1 and 3.2 show simulated pulse shapes to mimic the signals produced by a gamma source irradiating a CsI scintillation detector and a large volume HPGe detector, respectively. Characteristic for the pulse-shape of the signal of the HPGe detector in comparison with the scintillation detector is the exponential decay tail exceeding the rise time by factors 10 - 1000. The functionality of the algorithms has been studied by adjusting the parameters to the two different pulse shapes. The data used for different studies in this chapter are synthetic datasets. The algorithms have been first implemented and tested in the high-level language environment OCTAVE [40] and afterwards embedded in the FPGA (Field Programable Gate Array). All the data presented in this chapter are the results of the OCTAVE analysis.

The algorithms are implemented in a Field Programmable Gate Array (FPGA). The prototype board developed at KVI during this project, consists of a Quad ADC board [41] built on top of the previously developed Trigger and Response Board (TRB) [9] which was built for the HADES experiment [42] at GSI.

To understand better the structure of the pulse-shape analysis on the STRUCK SIS3302 [13], the scheme of the pulse-shape algorithms is shown in Fig. 3.3. The raw signal R , read from the ADC, is analyzed and filtered with the baseline follower

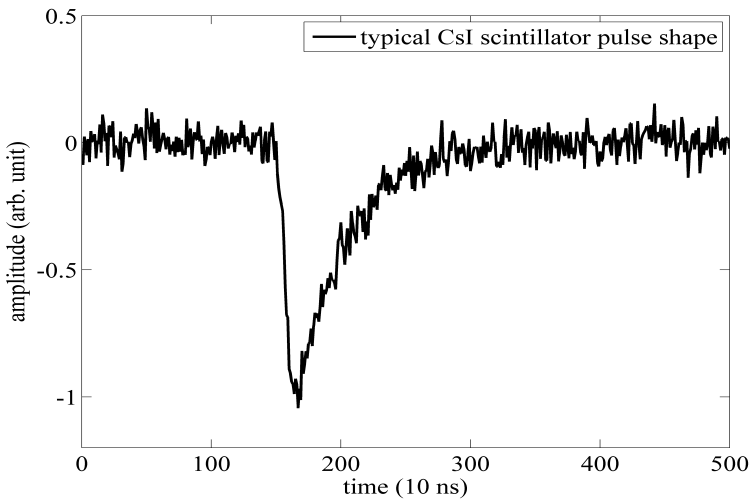


Figure 3.1: Simulated pulse-shape to mimic the signal produced by a photon of 0.66 MeV irradiating a CsI scintillation detector.

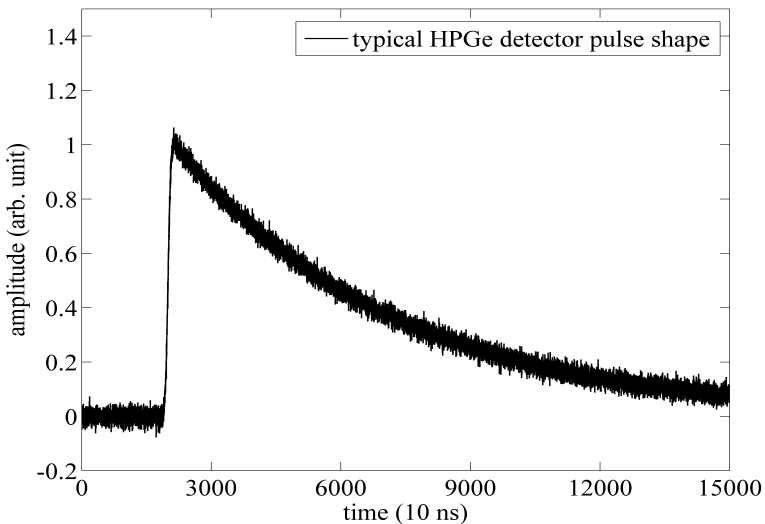


Figure 3.2: Simulated response of a high purity, large volume, Ge detector, irradiated by a photon of 0.66 MeV.

[43]. The information of the baseline values B and the filtered signal S can be used to calculate dynamically adjusted thresholds T . Whenever the filtered signal exceeds the value of the threshold T , the baseline follower enters a sleeping mode. The threshold T is also used as input for the box trigger, which returns the time stamps t_i of each occurring pulse, numbered i . The signal S , corrected with the baseline value B , is then filtered by the Moving Window Deconvolution (MWD) [44] and the Moving Average Filters (MAF) in order to recover the amplitudes a_i of each pulse. The time stamps t_i and amplitudes a_i are passed to the pile-up compensation unit and the compensated amplitudes b_i are recovered.

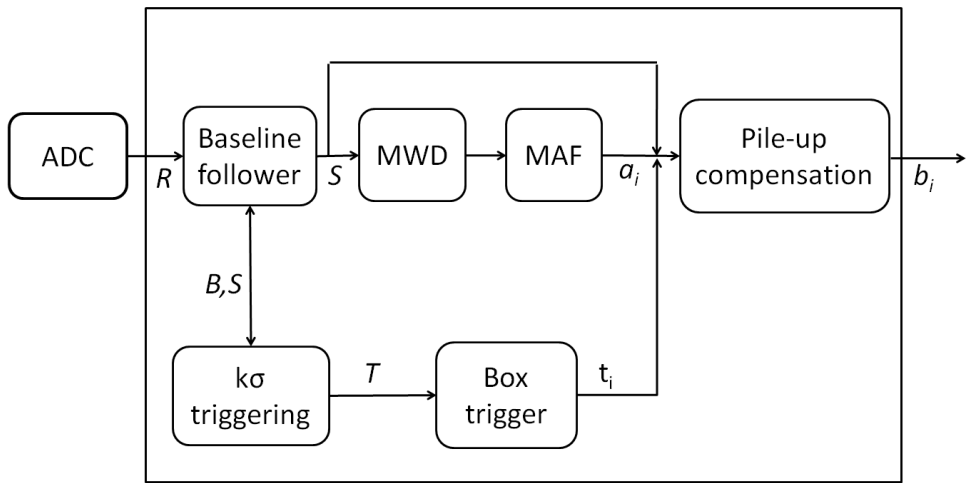


Figure 3.3: Scheme of the real-time signal analysis in the FPGA.

3.2 Baseline Follower and $k\sigma$ triggering

Whenever we proceed in the analysis of spectroscopic data, the first problem that we have to tackle is estimating the baseline. A digitized signal features both a noisy baseline that is fluctuating as well as large and extremely short-lived fluctuations of the noise, called spikes that originate from electronic pickup or after-pulses. Monitoring a dynamical baseline requires investigating the mean value and relative fluctuations

of the baseline during a given time interval, i.e. over a given baseline section, compared to previous average baseline values. This requires taking into account already processed data points which occurred before the events that are considered in the current analysis window. A baseline follower was developed [43] with the purpose to monitor the baseline and the variations caused by the occurrence of a pulse, and is organized as a first order recursive filter. The baseline follower:

- is able to follow a fluctuating baseline (the time scale of the fluctuations is much larger than the typical duration of a pulse);
- is immune to baseline pulling by the occurrence of a pulse;
- has a better signal-to-noise ratio;
- follows the noise level of the baseline (variance σ^2) and expresses the trigger level in units of σ^2 of the baseline noise.

The data contain three dynamic quantities: the signal pulses S (characterized by the pulse width W), the dynamical baseline (characterized by a variation on a timescale longer than W) and the baseline noise σ^2 (characterized by a timescale much larger than W). These three quantities are evaluated during every sampling period:

$$\begin{aligned} S(t_i) &= B(t_{i-1}) + \frac{1}{\tau_s} [R(t_i) - B(t_{i-1})] , \\ B(t_i) &= B(t_{i-1}) + \frac{1}{\tau_b} [R(t_i) - B(t_{i-1})] , \\ \sigma(t_i) &= \sigma(t_{i-1}) + \frac{1}{\tau_\sigma} [D(t_i) - \sigma(t_{i-1})] , \end{aligned} \quad (3.1)$$

where $R(t_i)$, $B(t_i)$ and $S(t_i)$ are the raw signal, baseline value and filtered signal at sampling time t_i , and t_{i-1} is the time at the previous sampling point. $D(t_i)$ is the deviation of the signal $S(t_i)$ from the baseline $B(t_i)$, $D(t_i) = |S(t_i) - B(t_i)|$, and τ_b , τ_s and τ_σ are parameters reflecting the dynamics of the digitized data stream. The values of the parameters τ_b , τ_s and τ_σ with respect to the pulse width W used in our simulation are given in Tab. 3.1. These parameters are fixed, their exact values being

set in the calibration phase depending on the width of the pulse W using an optimal Kalman filter [45]. The width of the pulse is taken equal to 5τ , where τ is the decay time constant of the pulse. After the time 5τ the amplitude of the signal drops to 1% of its original value. Each value may be understood as the required number of time samples necessary for the baseline follower to pick up the changes in the signal, baseline and noise fluctuations.

Table 3.1: Time parameters reflecting system dynamics.

Signal	Parameter	Value
Filtered signal	τ_s	$\frac{W}{5}$
Baseline	τ_b	W
Noise	τ_σ	$200W$

In order for the baseline follower to be immune to pulling due to the occurrence of a pulse, the follower enters a "sleeping mode" whenever a pulse is detected by the $k\sigma$ follower. This means that the evaluation of the mean value for the baseline is inhibited for a time equal to the length of the pulse and is picked up later starting with the last value available for the baseline. In order to make sure that the evaluation of the baseline value is not influenced by the leading edge of the pulse, before entering the sleeping mode the follower goes back a number of sampling points depending on the rise time of the pulse. Figure 3.4 shows the output (black line) of the baseline follower on synthesized data (gray line).

The trigger level $T = k\sigma$ is a dynamical quantity expressed in units of $\sigma(t_i)$, the standard noise deviation. The same value is used as an external threshold value for the box-trigger. In figure 3.5 we can see how the $k\sigma$ triggering works. The gray line represents the synthesized data, consisting of a slowly fluctuating baseline on which a random noise has been superimposed. Several peaks have been added to the data, as well as a number of spikes. The black line represents the evolution of the noise level expressed in units of σ . Due to the fact that the time parameters τ_b , τ_s and τ_σ have been set to match the dynamics of the real pulses, the $k\sigma$ method will prevent

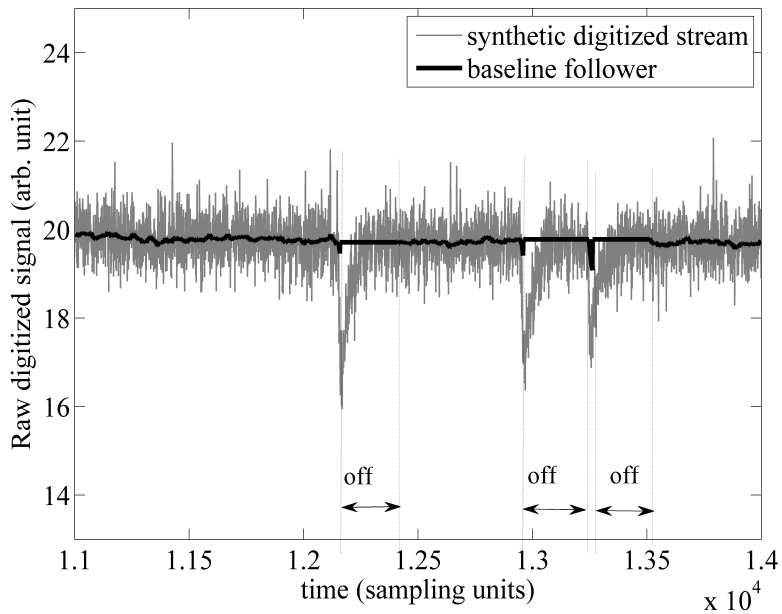


Figure 3.4: The output of the baseline follower $B(t_i)$ (black line) on a synthesized discrete digitizer output $R(t_i)$ (gray line). The periods the follower is "off" are indicated.

the triggering on the spikes, which are much shorter than the real pulses.

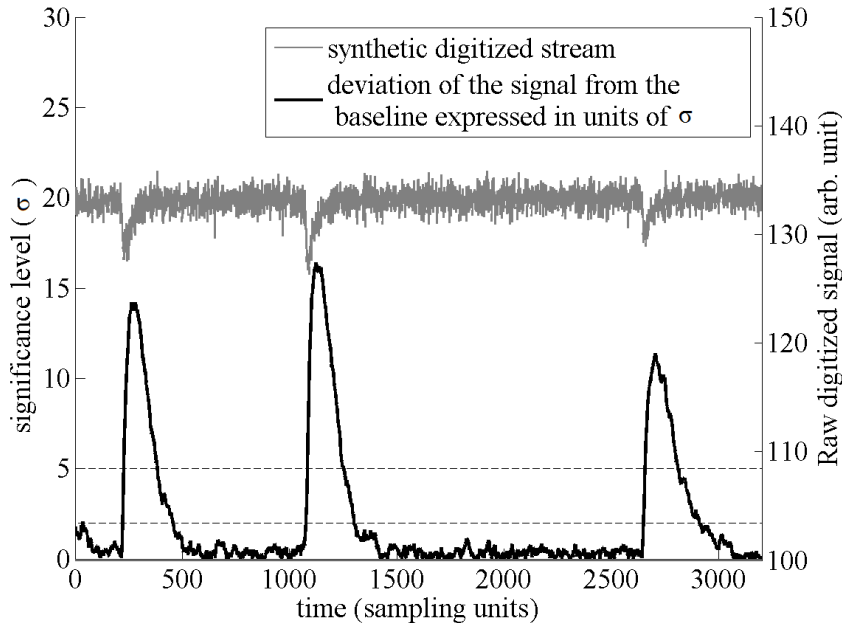


Figure 3.5: Schematic representation of the $k\sigma$ triggering. The black line, with values presented on the left vertical axis, shows the deviation from the baseline in units of σ ; the two dashed lines represent 2 and 5σ . The gray line is the digitized signal, with values presented on the right vertical axis.

3.3 Moving Window Deconvolution

The response of the preamplifier to the detector signal has the shape of a fast rising step caused by the charge collection, followed by a slow exponential decay. This exponential decay reduces the final peak height depending on the signal rise time. This influence of the preamplifier has to be removed from the signal in order to maintain the original pulse height. Moreover, the fact that the charge is only slowly decaying increases the dead time of a measurement, causes pile-up and prohibits a fast and reliable measurement. However, an improvement can be achieved using the Moving Window Deconvolution algorithm (MWD) [44]. Ideally, the preamplifier output features a single exponential decay and, by knowing the decay time and the start time

of the signal, the initial amplitude can be determined from a single data point of the decaying signal. A detailed discussion of the MWD algorithm can be found in [46].

From the expression of a single exponential decay starting at time $t_0 = 0$, the amplitude of the signal can be modeled at any given time by the expression:

$$A(t) = \begin{cases} N \exp\left(-\frac{t}{\tau}\right), & t \geq 0 \\ 0, & t < 0 \end{cases}, \quad (3.2)$$

where τ is the decay constant, and N the maximum amplitude. We define an auxiliary function $U(t_k)$ expressed in terms of the initial amplitude N for times $t_k > 0$ as follows:

$$\begin{aligned} U(t_k) &= A(t_k) + N - A(t_k) \\ &= A(t_k) + N \left(1 - \exp\left(-\frac{t_k}{\tau}\right)\right) \\ &= A(t_k) + \frac{1}{\tau} \int_0^{t_k} dt A(t) \\ &= A(t_k) + \frac{1}{\tau} \int_{-\infty}^{t_k} dt A(t), \end{aligned} \quad (3.3)$$

where the extension of the integral to $-\infty$ in the last step can be made because the amplitude $A(t)$ is zero for times $t < 0$. Although we have started with an expression for $U(t)$ valid only for times $t > 0$, we can extend the expression in Eq. 3.3 for times $t_k < 0$. The auxiliary function $U(t)$ is simply:

$$U(t) = \begin{cases} N & t \geq 0 \\ 0, & t < 0 \end{cases}, \quad (3.4)$$

If we transform the expression in Eq. 3.3 to the digital domain we get the value for N at time t_k :

$$U(t_k) = A(t_k) + \frac{1}{\tau} \sum_{i=-\infty}^{k-1} A(t_i), \quad (3.5)$$

where τ is now expressed in units of the sampling time.

Although there are several algorithms to compensate for the exponential decay, the moving window deconvolution has the advantage of being both fast and intuitive, which makes it ideal for the implementation on the FPGA. The expression for

the MWD simply follows from differentiating the expression in Eq. 3.5. If $A(t_k)$, $A(t_{k-1})$, ..., $A(t_0)$ are the digitized signal samples and w is the width of the moving window, then the output of the filter at a given time t_k is given by the expression:

$$\begin{aligned} MWD(t_k) &= U(t_k) - U(t_{k-w}) \\ &= A(t_k) - A(t_{k-w}) + \frac{1}{\tau} \sum_{i=k-w}^{k-1} A(t_i), \end{aligned} \quad (3.6)$$

where τ is the exponential decay time constant to compensate for, expressed in units of the sampling time.

Ideally, if the rise time is zero (or less than one sampling unit), by applying the moving window deconvolution to the original slowly-decaying exponential signal, the long tail of the pulse shape is transformed into a rectangular pulse shape, with a duration equal to the span of the moving window, as seen in Fig. 3.6a. However, on a real signal, for which the rise time is nonzero, the transformed signal shape will present a leading edge (a deformation from the rectangular shape) that reflects the shape of the original digitized signal corrected for the exponential decay. Furthermore, the processed signal reaches a plateau value, that is exactly the same for a given deposited energy inside the detector, independent of the rise time, after which it returns to zero with no tail, as in Fig. 3.6a.

Selecting a wrong value for the τ parameter of the moving window deconvolution algorithm, different from the exponential decay constant, may lead to errors in the evaluation of the amplitude of the initial pulse shape, as shown in Fig. 3.6b and Fig. 3.6c. Using an underestimated value of the decay constant will lead to a positive slope on the step function and consequently an overestimation of the original amplitude. The processed signal presents a long tail, instead of dropping to zero. This tail will have further influence on the following pulse signal that will be processed with the moving window deconvolution, giving rise to an overestimation of its amplitude. On the other hand, selecting a too large value for τ will be reflected in the processed signal by a descending slope on the step function and an underestimation of the amplitude. The decay constant τ is evaluated from the standard pulse shape. From the tail of the pulse, we select the interval between the point t_1 where the amplitude is

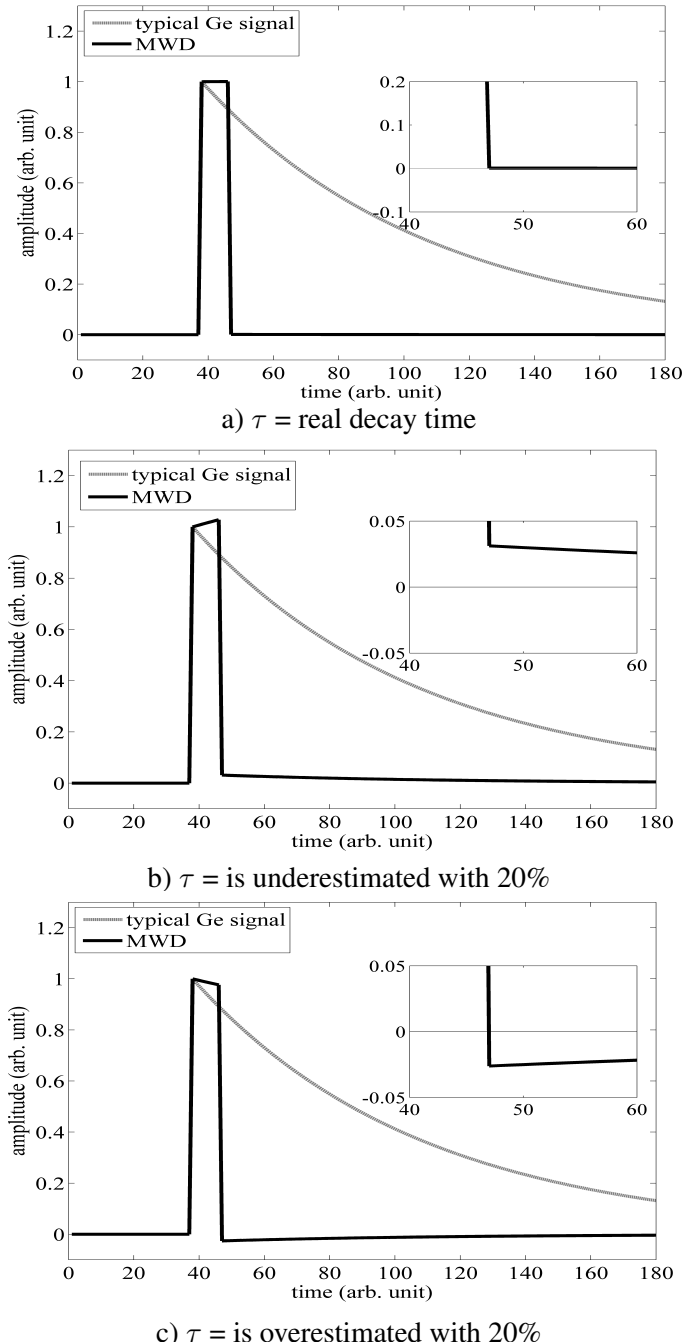


Figure 3.6: Moving Window Deconvolution. The gray dashed line corresponds to the original exponential decay, whereas the black line corresponds to the result of the MWD algorithm. The inserts are enlargements of the area situated between 40 and 60 units on the horizontal axis and in the vicinity of zero on the vertical axis.

90% of the top value and the point t_2 where the amplitude is equal to 10% of the top value. The exponential decay time constant expressed in sampling units is calculated with a linear regression on $y = A e^{-t/\tau}$:

$$\tau = \frac{t_2 - t_1}{\ln 9} = \frac{t_2 - t_1}{2.197}. \quad (3.7)$$

For HPGe detectors, for a sampling rate of 100 MHz, the decay constant is of the order of $10^3 - 10^4$ sampling units. For a decay constant of 10^3 sampling points, the error in estimating the time decay constant is smaller than 0.1%. However, for CsI detectors, for a sampling rate of 100 MHz, the decay constant is of the order of $10 - 10^2$ sampling units. For a decay constant of 10 sampling points, the error in evaluating τ is 9%.

The width w of the moving window is also a very important parameter. By selecting a value smaller than the rise time, the processed signal shape will never reach the stable, flat plateau, and thus the value at the top will not be proportional to the deposited energy inside the detector. This is an important observation, since our FPGA implementation on the SIS3302 [13] only allows for 8 bits of storage for this value, which makes the maximum value 255. If the rise time, in terms of sampling units, is longer than the maximum value permitted for the window span, the sampling unit has to be increased, until the rise time of the pulse, expressed in sampling units, becomes smaller than the maximum value allowed for the span of the window. On the other hand, a value too large for the window will limit the separation power of the MWD algorithm. Figure 3.7 shows how the application of the MWD method will lead to greatly improved results. The gray line mimics an original sample composed of ideal pulses, while the black line is the output of the MWD on the original stream. After the filter is applied, the initially piled-up pulses are completely separated and their amplitudes are recovered.

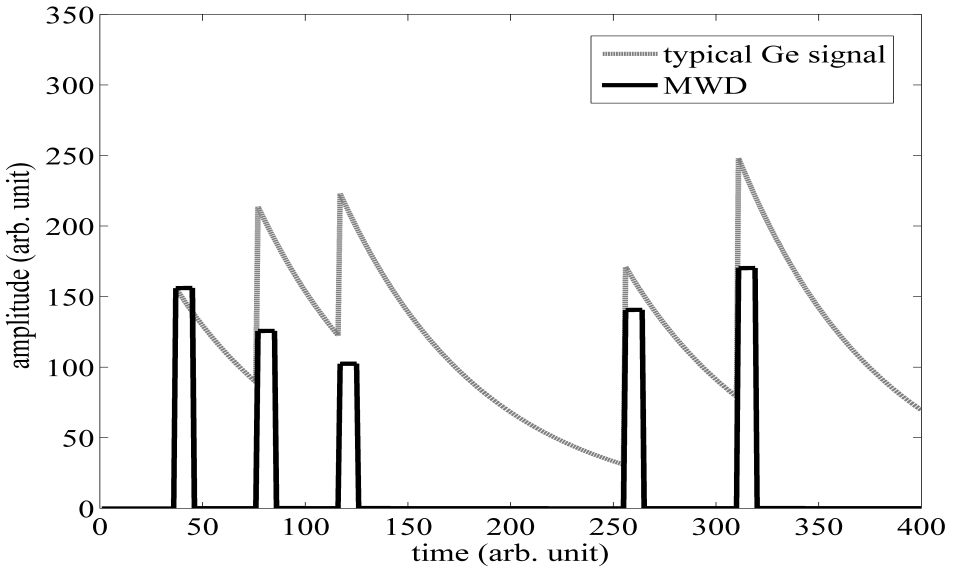


Figure 3.7: Result (black line) of the moving window deconvolution (MWD) algorithm on a set of synthetic piled-up Ge pulses (gray line).

3.4 Moving Average Filter

The moving average is the most common filter in digital signal processing, mainly because it is the easiest digital filter to understand and use. Despite its simplicity, the moving average filter (MAF) [46] is optimal for a common task: reducing random noise while retaining a sharp step response. As the name implies, the moving average filter operates by averaging a number of points from the input signal to produce one point in the output signal. This procedure is expressed by the following equation:

$$MAF(t_k) = \frac{1}{w'} \sum_{j=1}^{w'} x(t_{k-j}), \quad (3.8)$$

where: $x(t_k), x(t_{k-1}) \dots x(t_{k-w})$ is the signal at the sample times $t_k, t_{k-1} \dots t_{k-w}$, $MAF(t_k)$ is the output signal at time t_k , and w' is the width of the filter window, equal to the number of points in the average.

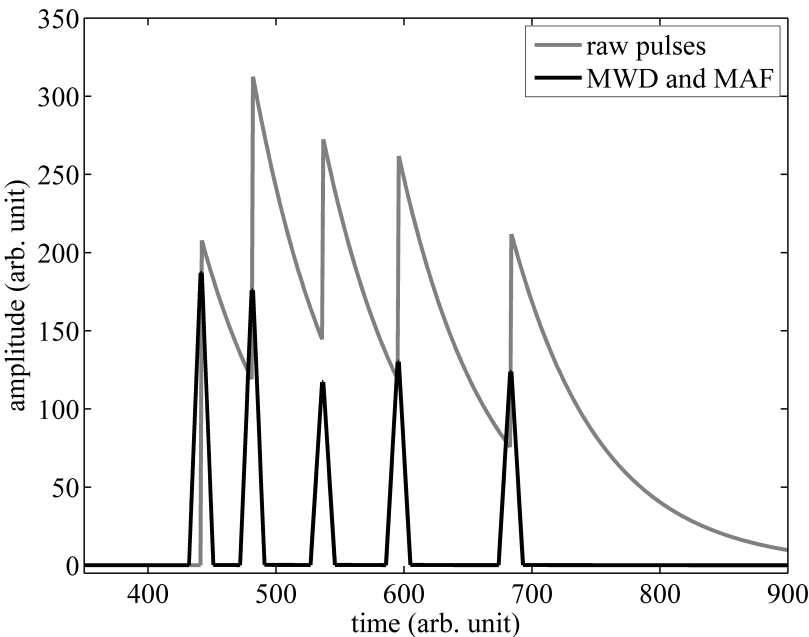


Figure 3.8: The output of the moving window deconvolution (MWD) and moving average filters (MAF) (black line) on a synthetic digitized stream (gray line).

In the SIS3302 FPGA, the moving average filter is implemented by adding to the previous value of the moving average filter the current signal value and subtracting the value of the signal at $w + 1$ samples earlier. This is done on each clock cycle. The resulting sum is scaled afterwards by shifting the bits.

$$MAF(t_k) = MAF(t_{k-1}) + \frac{1}{w'} (x(t_k) - x(t_{k-w'-1})) . \quad (3.9)$$

The moving average filter is used to filter the output of the moving window deconvolution for measuring the amplitude. Figure 3.8 shows the output (black line) of the moving average filter (MAF) combined with the MWD on a stream of synthesized data (gray line), consisting of ideal pulses of varying amplitudes.

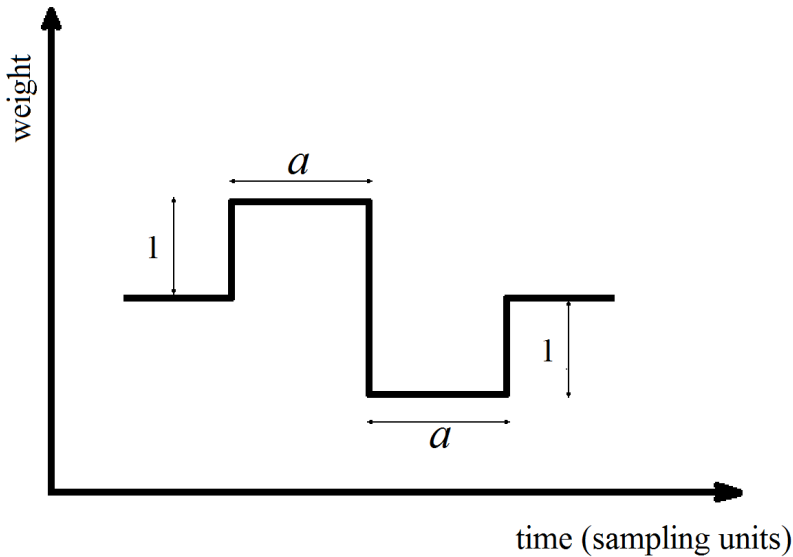


Figure 3.9: Schematic representation of the box-trigger.

3.5 Box-trigger

The box-trigger is a fast efficient triggering method, easy to implement on the FPGA. The box-trigger is given by the convolution of the stream of data with the signal shown in Fig. 3.9. The positive and the negative parts of the box-trigger are of the same size equal to a sampling points. If $A(t_k), A(t_{k-1}), \dots, A(t_0)$ are the digitized signal samples and a is the magnitude of the box, then the output of the trigger at a given time t_k is given by the expression:

$$BOX(t_k) = \sum_{i=k-2a+1}^{k-a} A(t_i) - \sum_{i=k-a+1}^k A(t_i). \quad (3.10)$$

As can be seen from Eq. 3.10, the box-trigger is a box version of the first derivative of the typical pulses to be measured. The method is not affected by the dynamics of the baseline, as long as the baseline fluctuations occur at a scale that is greater than the size of the box a . The box-trigger can be applied without any baseline correction

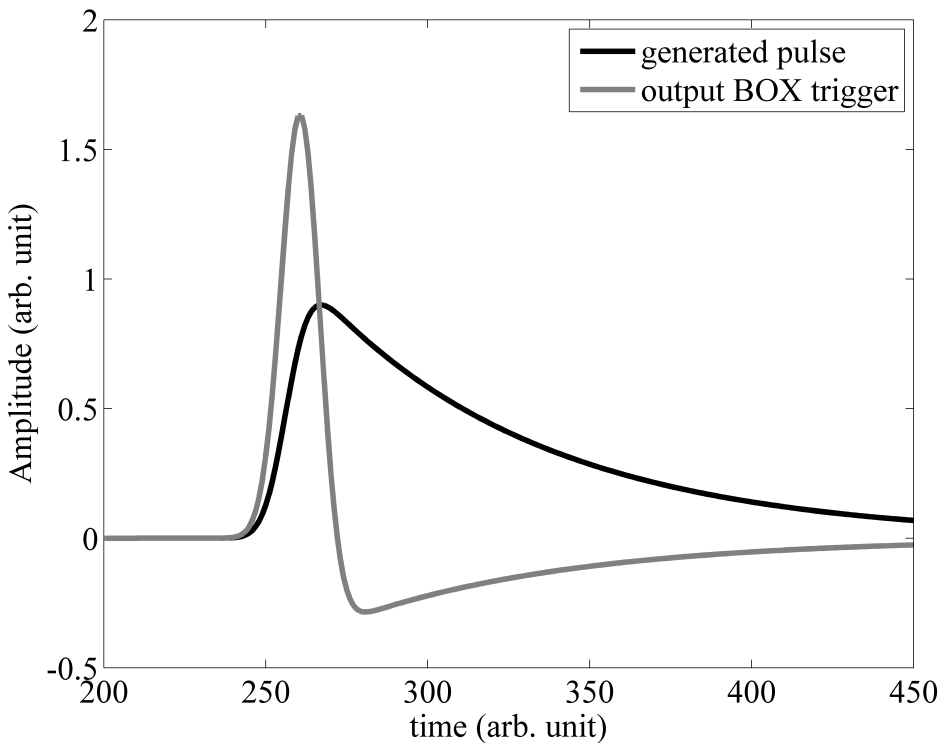


Figure 3.10: The output of the box-trigger (gray line) on a generated signal (black line).

on the digitized data stream, since the current baseline value is added and subtracted an equal number of times. The output of the box-trigger on a typical pulse is given in Fig. 3.10. The black line represents a typical signal coming from the detector, while the gray line is the response of the box-trigger. When the output of this filter exceeds an adjustable threshold value, the input pulse is detected. As can be seen in Fig. 3.11, it is not straightforward to select a value for the threshold. A threshold value too small or too large will lead to misidentification of the two pulses in case of signal pile-up. In principle, the threshold value is based on the magnitude of the noise level, as given by the $k\sigma$ triggering.

The efficiency of the box-trigger has been studied on artificial data sets, in different pile-up regimes. Several sets consisting of two pulses without noise have been

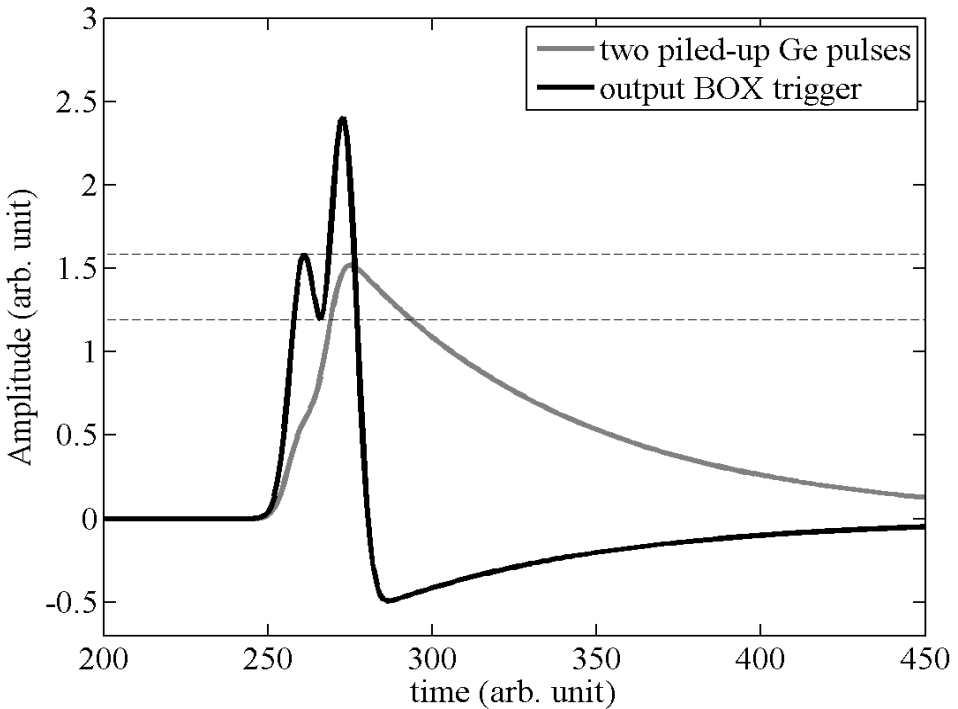


Figure 3.11: The output of the box-trigger on two piled-up pulses. The gray line is the simulated trace with two piled-up Ge detector pulses. The black line is the output of the box-trigger. The higher dashed line is the largest value for the threshold for which two pulses will be detected, while the lower dashed line is the smallest value for the threshold for which two pulses will be detected.

generated; for the simulation of these sets several parameters have been varied: the time delay between the two pulses, the relative magnitude of the two pulses, and the value of the box window. For each set of two generated pulses, two limit values have been calculated: the lower limit is given by the lowest positive threshold value that will give two hits for the box-trigger and is called threshold 1; the upper limit is given by the maximum value that will obey the same condition and is called threshold 2, where the relation threshold 1 < threshold 2 always holds. In Fig. 3.11 threshold 1 is the value of the dip between the two peaks (lower line) and threshold 2 is the

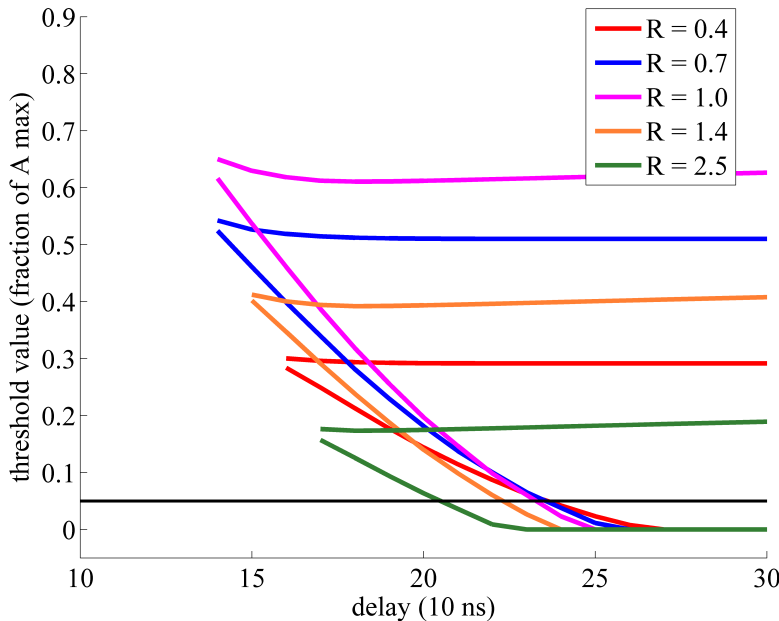


Figure 3.12: Dependence of the limiting threshold values on the delay time between the two pulses for different values of the relative amplitude of the two pulses. Note that a sampling point represents a delay of 10 ns. Threshold 1 is the lower curve and threshold 2 is the upper curve of the same color. The box-trigger with 100 ns sampling window has been applied.

amplitude of the first peak (upper line).

The results of the study have been plotted in figures 3.12 and 3.13. Fig. 3.12 shows the dependence of the limiting thresholds on the relative amplitude and the delay time between the two pulses. Sets of two pulses with different amplitude ratios, varying from 0.4 to 2.5 have been generated. The ratio R is given by A_2/A_1 , where A_1 is the amplitude of the first pulse, A_2 is the amplitude of the second pulse, with the condition that the largest of the two amplitudes is always the same. The time delay between the two pulses has been varied between 2 sampling units up to 30 sampling units. The box-trigger with the window of 10 sampling points has been applied to each set. For each set, the limit thresholds have been determined and their values have been plotted. From Fig. 3.12, it is easily seen that the curves flatten to zero at

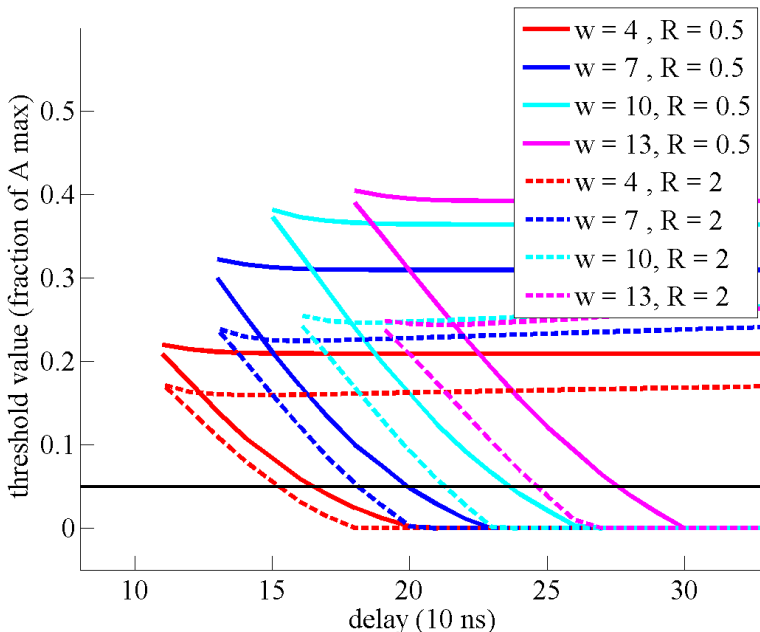


Figure 3.13: Dependence of the limiting threshold values on the delay time between the two pulses, for different widths of the window w of the box trigger. Note that a sampling point represents a delay of 10 ns.

27 sampling points, which means that at this point, the two pulses are completely separated by a box trigger with a window of 10 sampling points. Fig. 3.13 shows the dependence of the two threshold values on the window w of the box trigger. The results are plotted for two symmetric cases: the ratio of the two amplitudes $R = 0.5$ and $R = 2$. It is obvious that a smaller window w will produce a faster response of the box trigger, which will enable to identify pulses earlier than a box trigger with a larger window, although the tolerance to noise is reduced. For a box trigger with a window of 10 sampling points this value flattens out.

The efficiency of the pile-up compensation method depends on the efficiency of the box trigger for a given rate. If we assume a set of signals of equal amplitudes and a threshold T , evaluated with the $k\sigma$ triggering, equal to 5% of the amplitude, we can read from Fig. 3.12 that the box trigger with a window 100 ns will recog-

nize pulses that are more than 233 ns apart, the point where the line representing a threshold of 0.05 intersects the first threshold. For the generated pulse shape we use the decay constant $\tau_{decay}=750$ ns. We can use this information to evaluate how many of the pulses will not be detected by the box trigger, using a Poisson distribution for the times. The expression for the distribution of the time distance between two consecutive pulses is:

$$f(t) = \begin{cases} \lambda e^{-\lambda t}, & t \geq 0; \\ 0, & t < 0 \end{cases}, \quad (3.11)$$

where λ is the counting rate. For a low pile-up regime, with $\lambda = 1/(50\tau_{decay}) = 27$ kHz, the box trigger will identify 99.5% of the pulses. For a moderate pile-up regime, with $\lambda = 1/(15\tau_{decay}) = 89$ kHz, the box trigger will identify 98% of the pulses. However, for a severe pile-up regime, with $\lambda = 1/(3\tau_{decay}) = 444$ kHz, the box trigger will identify 90% of the pulses.

3.6 Pile-up Compensation

A new method of event-by-event pile-up compensation has been developed [47, 48], which uses the time stamps obtained in the signal analysis for the individual pulses to correct for pile-up effects in the measurement of pulse heights. We have implemented this technique in the FPGA to deal with piled-up pulses. One important requirement of our method is the stability of the pulse shape. Since the baseline corrections have already been applied, we can simply assume in our analysis, without losing the generality of the method, a series of pulses with a stable pulse shape superimposed on a zero-value baseline. If we define $p(t)$ to be the standard pulse shape, the i -th pulse with an amplitude a_i occurring at a time t_i can be modeled as:

$$p_i(t) = a_i p(t - t_i). \quad (3.12)$$

The digitized sample signal $s(t)$ as a function of time t can then be described over time as a sequence of pulses:

$$s(t) = \sum_i a_i p(t - t_i), \quad (3.13)$$

where both t and t_i are expressed in terms of the sampling period. However, the measured amplitudes are usually estimated by a weighted average of the original sampling sequence, in the vicinity of the peak of the pulse. This summation is constructed as a finite response filter (FIR), mathematically represented as:

$$q(t) = \sum_k f(k) s(t - k), \quad (3.14)$$

where $q(t)$ is the response of such a filter, described by the weights $f(k)$.

However, the presence of such a filter will induce a constant lag l in the time stamping of the measured pulses with respect to their original time of occurrence. Thus, the estimate of the amplitude b_i is defined by:

$$\begin{aligned} b_i &= \sum_k f(k) s(t_i - k + l) \\ &= \sum_k f(k) \left(\sum_j p(t_i - t_j + l - k) a_j \right) \\ &= \sum_j \left(\sum_k f(k) p(t_i - t_j + l - k) \right) a_j. \end{aligned} \quad (3.15)$$

As is easily seen from the equation above, the measured amplitudes are, in fact, just a linear combination of the real amplitudes. An example of pile-up is illustrated in Fig. 3.14. The amplitude of the pulse b_i is affected by the pulses b_{i-1} and b_{i+1} . In principle one has to deal with a linear problem, whose dimension is equal to the number of occurring pulses for the duration of the measurement. In general, this can be expressed as:

$$\mathbf{b} = \mathbf{M}\mathbf{a}, \quad (3.16)$$

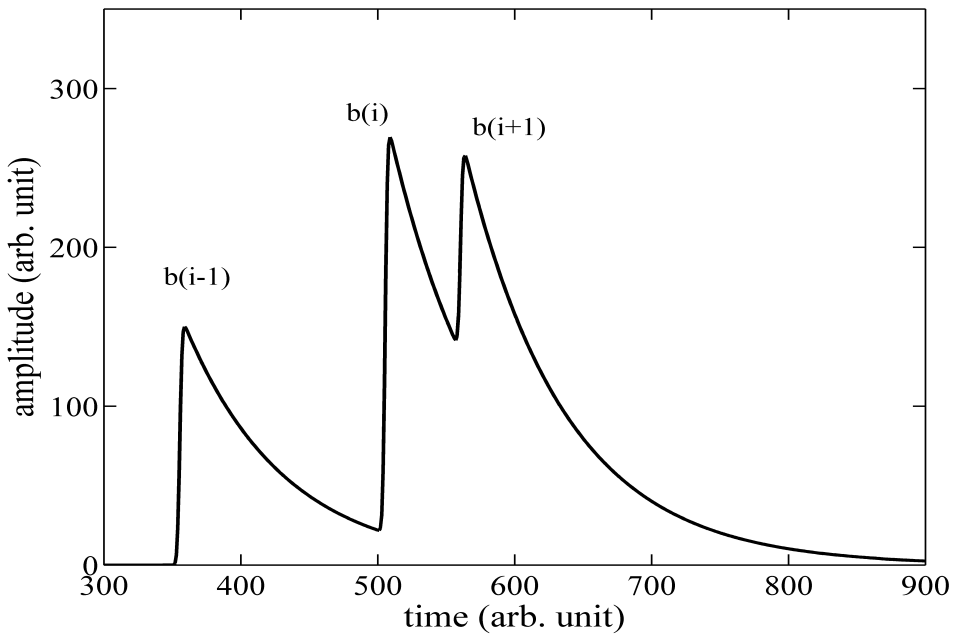


Figure 3.14: Example of Ge detector pulses in the pile-up regime.

where the elements of the pile-up matrix \mathbf{M} are defined as:

$$M_{i,j} = m(t_i - t_j + l), \quad (3.17)$$

$$m(t) = \sum_k f(k) p(t - k). \quad (3.18)$$

Nonetheless, the dimension of the problem can be reduced, due to the dominant diagonal band nature of \mathbf{M} . Furthermore, the values of the coefficients inside the matrix \mathbf{M} rapidly decrease as they deviate from the diagonal. A good approximate solution for such a matrix is to assume small numbers of pulses and to solve the system of linear equations for the reduced problem. This approximation allows for a real-time implementation, since it is not necessary to wait for the end of the measurement to be able to invert the matrix \mathbf{M} .

In principle, an easy way of simplifying the problem is to assume that each pulse is affected at most by a finite number of neighboring pulses that occur either before

or after the current pulse. If one assumes the simplest case, in which the current pulse is affected by one pulse before and one pulse after, then in order to calculate the real amplitude of the current pulse one needs to invert a 3×3 matrix. Without reducing the generality of the method, one may assume the elements of the matrix to be normalized. The mixing of the triplet formed by the pulses $i - 1, i, i + 1$ is described by

$$\begin{pmatrix} 1 & p & 0 \\ r & 1 & q \\ 0 & s & 1 \end{pmatrix} \begin{pmatrix} a_{i-1} \\ a_i \\ a_{i+1} \end{pmatrix} = \begin{pmatrix} b_{i-1} \\ b_i \\ b_{i+1} \end{pmatrix}, \quad (3.19)$$

where

$$\begin{aligned} p &= m(t_{i-1} - t_i + l), \\ r &= m(t_i - t_{i-1} + l), \\ q &= m(t_i - t_{i+1} + l), \\ s &= m(t_{i+1} - t_i + l). \end{aligned} \quad (3.20)$$

The analytical inverse for a_i is equal to:

$$a_i = \frac{b_i - rb_{i-1} - qb_{i+1}}{1 - pr - qs}. \quad (3.21)$$

As can be easily seen from equations 3.20 and 3.21, the products pr and qs depend on the same time difference, i.e. $(t_i - t_{i-1})$ and $(t_{i+1} - t_i)$, respectively. Therefore, these products can be tabulated and just extracted from a lookup table. It is clear that in the first-neighbor approximation the procedure requires the storage of two lookup tables $m(\Delta t + l)$ and $m(\Delta t + l) m(-\Delta t + l)$. One problem may arise if the denominator of Eq. 3.21 is 0. In this case the matrix \mathbf{M} is singular, which means that a_i cannot be uniquely determined. Should such an event occur, the implementation of the method catches the error, for example if $|pr + qs - 1| < \epsilon$ the algorithm returns the best known value for a_i , i.e. b_i . ϵ represents a small number. If the current pulse is affected by more than one pulse before or after, which is the case for high rates, the situation is more complicated as the size of the matrix increases. In any case, one tests at every step if the matrix is singular, for which case the pile-up compensation module returns b_i for the current pulse value.

The method has been tested [48] both on synthetic data sets, as well as measured data. For each synthetic data set, 10^6 pulses have been generated. Each pulse has been modeled as an exponential with the decay constant of 25 samples folded with a Gaussian of width 2 samples to obtain both a non-zero rise-time and to test the stability of the method against time stamp distortions. The generated pulses have the same amplitude A , with an explicitly implemented width of the distribution of 5% full-width at half-maximum around the mean value. Tests have been performed for three different counting rates, each corresponding to a different pileup regime: $1/(50\tau_{decay})$, which corresponds to the low pileup regime, $1/(15\tau_{decay})$, corresponding to a moderate pileup regime, and $1/(3\tau_{decay})$, corresponding to a severe pileup regime. Time stamping was performed using the box trigger with a width of 3 sampling units. The procedure generated a set of time stamped amplitudes $b_i(t_i)$ that were used as input for the pileup compensation algorithm with the first neighbor approximation. As seen from Fig. 3.15, the pile-up compensation improves greatly the spectrum of uncorrected amplitudes. Nonetheless, some artifacts are easily identifiable. The method is unable to separate or resolve in the recovered spectrum (blue line) amplitude values which are equal to an integer multiple of the initial amplitude A , $2A$. This can be intuitively understood from the origin of these values. Since all generated amplitudes had the same value A , a value like $2A$ comes from two generated amplitudes with time stamps very close to each other, but which the trigger is unable to resolve. The algorithm identifies only one of the peaks and assigns an amplitude equal to the summation of the amplitudes of the two original pulses. This explains the presence of the peaks at A , $2A$.

The method clearly shows a great improvement in the reconstruction of the original signal. Moreover, in the case of severe pileup (rate of $1/3\tau_{decay}$), even though initially one can not recognize a peak, after applying the pileup compensation a peak is easily identifiable and more than 65% percent of the simulated data is recovered. The same great improvement can be seen in Fig. 3.16 on a measured spectrum of a ^{137}Cs gamma source irradiating a CsI scintillator with a rate of 45 kHz. The blue line is the measured spectrum, whereas the red line is the spectrum obtained after ap-

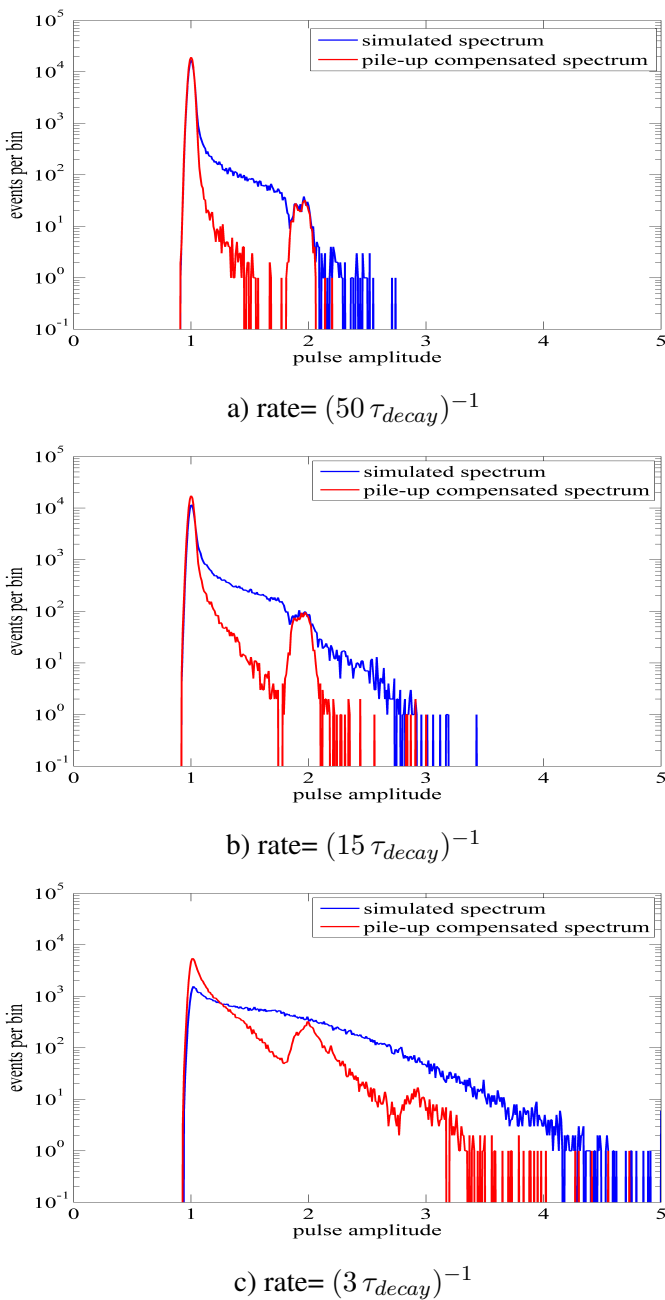


Figure 3.15: Pile-up compensation in the first-neighbor approximation for three different pile-up regimes with τ_{decay} the decay time of the pulse. The blue line represents the simulated spectrum, as recovered by the digital data acquisition system. The red line is the spectrum obtained from the simulated spectrum after the pile-up compensation.

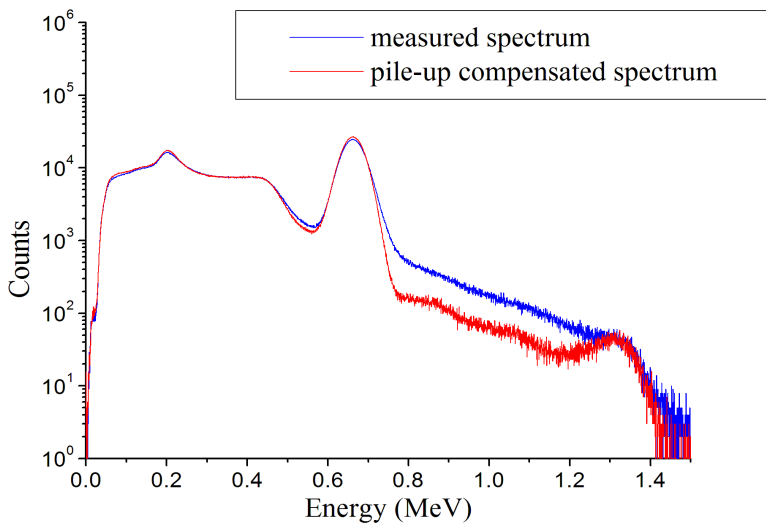


Figure 3.16: Pile-up compensation for a measured spectrum of a CsI detector irradiated by a ^{137}Cs γ -source, with a rate of 45 kHz.

plying the pile-up compensation routine. In the case of the pile-up compensation the number of counts in the photo-peak area increased by 35% compared to the number of counts in the photo-peak when no compensation has been applied.

As stated before, an exact simple analytic solution for a larger pile-up matrix is not readily at hand. Even though the problem is reduced to solving a set of linear equations, the real difficulty consists of doing this in a way, that is suited for real-time implementations. In this case, instead of using an exact solver for the set of linear equations, an approximate solution based on an iterative procedure proves to be the right way to handle the real-time implementation. Usually such a method consists of the iteration of a computationally inexpensive process for a certain number of times until the approximation is close enough to the exact solution of the problem. One important requirement for an iterative procedure is a fast convergence. Such methods have been extensively studied in [47]. Among the methods studied, the Gauss-Seidel [47] method showed better convergence in the given domain; the precision of the

result can be changed by adjusting the number of iterations. This method has been optimized for the Xilinx Virtex-4 FPGA and was implemented on the SIS3302.

3.7 Developed hardware for R&D towards NuSTAR FEE

In the course of this project two types of FEE have been used. The prototype board was developed at KVI [49], during this thesis, and consists of a Quad ADC board [41] built on top of the previously developed Trigger and Response Board (TRB) [9]. The prototype contains a Xilinx [10] Virtex-4 Field Programmable Gate Array (FPGA). The specifications of the Quad ADC board are enumerated in the following list:

- Number of ADCs : 4 (type ADS5541),
- Resolution : 14 bits,
- Speed : 100 MSamples/s,
- Bandwidth : 50 MHz,
- Input range : -4 to 4 Volt,
- Input connector : SMA,
- Input impedance : 50 Ohm,
- External trigger inputs : 4*SMA,
- External trigger input impedance : 50 Ohm,
- Power supply : 5 Volt from TRB.

On the second board [50] of each QuadADC we have implemented our DPSA algorithms. During the beam test experiment discussed in chapter 5 we used the Struck SIS3302 16-bits ADC board [13]. A few specifications of the SIS3302 board are given here:

- Number of FPGAs : 5,

- FPGA type : Xilinx Spartan Xcs31000,
- Number of ADCs : 8,
- Resolution : 16 bits,
- Speed : 100 MSamples/s.

One of the five FPGAs is used for the interface to the VME-bus. Each one of the others performs Pulse-Shape Analysis on the data from two ADCs.

One of the main reasons for focusing the R&D developments towards FPGAs was the fact, that they are fully parallel by design, which will not put any constraints on scalability of our algorithms. The internal resources of an FPGA chip consist of a matrix of configurable logic blocks with I/O blocks on the side. FPGAs are arrays of programmable gates which can be programmed into many parallel hardware paths. This makes that different processing operations do not have to compete for the same resources. It allows the user to create any number of task-specific cores that all run like simultaneous parallel circuits inside one FPGA chip. A further discussion on the parallel nature of an FPGA can be found in [51].

4

Non-supervised control loops based on local digitized-signal processing

4.1 NuSTAR data acquisition

The NuSTAR [3] data acquisition (DAQ) concept tries to incorporate and deal with the changes that are related to the discontinuation of production and support of all CAMAC [52] and FASTBUS [53] modules, together with the much increasing number of channels in the different experiments. Dedicated front-end electronics boards are foreseen in most experiments for NuSTAR. The other main issue is to provide a maximum interoperability of the different setups of the NuSTAR facility, as many parts of particular setups, detectors systems and their associated DAQ systems should be used simultaneously. The in-ring instrumentation of the NESR [7] that will be used in parallel by the EXL [8, 54, 55] and ELISe [56, 57, 58] collaborations may serve as an example. The same holds for the combination of Super-FRS [4] instrumentation and R³B [5] setup, or gamma-spectroscopy arrays in conjunction with reaction setups. It is mandatory for the NuSTAR DAQ to allow a certain flexibility to be able to couple various systems together.

The main idea is to build a highly parallel, self-triggered system that can transfer time stamped data streams of up to one TB/s over standard networks. Event definition, building, and filtering will then be done on computer farms. However, the current Multi-Branch System (MBS) DAQ has access to control a huge hardware base (about 100 devices installed, 50% outside GSI) and it, therefore, must be integrated in the new DAQ concept. The new DAQ system must meet the following requirements: be able to build events over fast networks, handle triggered or triggerless front-ends (a detailed discussion can be found in [59]), process time stamped data streams, provide data-flow control (to front-ends), connect to (nearly) any front-end, provide interfaces to plug in application codes, and connect MBS readout or collector nodes. Last but not least, it must be controllable by several control frameworks.

EPICS (Experimental Physics and Industrial Control System) [11] is a widely used scalable control system that meets most of the requirements listed above. The use of EPICS has the advantages of being free of purchase or licensing costs, providing reliability even for applications that require the handling of a large amount of variables, not requiring large hardware resources and being extremely adaptable. The EPICS Input/Output Controller (IOC) is a server application that can run on many platforms (Linux or Windows PC, embedded systems, etc.) and is in charge of delivering information on the current system parameters over the network in regular intervals or upon request. Requests to the server can be done from normal computers running client applications, which can directly take any data distributed by the servers, achieving an easy maintainable and reliable system.

The communication is based on the Channel Access (CA) protocol using Ethernet as transport layer. The IOC (Input/Output Controller) is the application which provides Process Variables (PV) via CA. Once a PV is published, it is visible over the whole network. EPICS gives the freedom to use any CA client to display the acquired data. Presently, the user interface builder MEDM (Motif Editor and Display Manager) [60] is used at GSI. But in the near future other means of displaying CA data will be tested. Any other service than displaying, such as archiving, building histograms, and alarm handling are available as CA clients.

The GSI standard MBS DAQ system provides status information for the server. An EPICS IOC on a Linux machine [61] was implemented to retrieve this status structure, which enables the reading of the MBS status at intervals of 1 second.

It should be possible, via MBS and EPICS, to couple together different stand-alone NuSTAR DAQ systems in a simple way. Typically, the individual DAQ systems are used to set up and debug detector groups or experiments. Such a scheme can be realized by taking into account the necessary settings for triggers and control signals and by keeping the modularity of the system and event buffer capabilities in mind while building the local trigger.

For the common NuSTAR DAQ system, specific Front-End Electronics (FEE) together with their digitization part are seen as part of the detector. Only the control, trigger and data flow will be specified as interface description by the common NuSTAR DAQ system. This includes the necessary trigger types to be implemented, like data, calibration and synchronization triggers together with a prescription on how to lock the FEE to realize a clearly defined dead time of the total system.

We foresee two kinds of data from the experiments: event-by-event data that is taken with the physics and control triggers and the second type of data, called slow-control data, like scaler readouts and beam profiles. These data are of interest for the distributed slow-control system throughout the NuSTAR facility and the accelerator. For example, profile data may be taken to generate a feedback loop in order to perform automatic beam steering, whereas scaler data can provide information on the sanity of particular setups. Some of the main parameters to be controlled are the threshold settings, the temperature monitoring over the system, the voltages and currents of the power supplies, turning on/off the power supplies, and flow and pressure monitoring of the gas components.

4.2 Control systems and self-adjusting control loops

The term "control" has many meanings and often varies between communities. We define control as the use of algorithms and feedback in engineered systems. Control provides the principles and methods that maintain a desirable performance of the

system that is automatically adapting to changes in the environment. These methods are established using a variety of modeling and analysis techniques that capture the essential dynamics of the system and permit the exploration of possible behaviors in the presence of uncertainty, noise and component failure. The algorithm that computes the control action as a function of the sensor values is often called a *control law*. The purpose of controlling a process is to ensure that all the requirements for the process take place without human intervention. For a deeper understanding of the control theory and the control techniques involved in the present chapter the following references are recommended [62, 63].

We have a dynamical system which is defined as a system whose behavior changes over time, often in response to external stimulation or forces. We use the term feedback to describe the case in which at least two dynamical systems, the original system (called a plant) and the controller, are connected together such that each system influences the other and their dynamics are thus strongly coupled. The two fundamental structures for realizing controls are open-loop (Fig. 4.1a) and closed-loop control, also known as feedback control (Fig. 4.1b).

Figure 4.1b is a closed-loop system since the different subsystems are interconnected in a cycle. If the structure cycle is not present, then we have an open loop as seen in Figure 4.1a. One of the key uses of feedback is to provide stability to the system. By measuring the difference between the sensed value of a regulated signal and its desired value, one can supply a corrective action. If the system undergoes some change that affects the regulated signal, then the controller senses this change and tries to force the system back to the desired operating point.

Open-loop control is generally simpler, it does not require a sensor to measure the output, and does not, on its own, introduce stability problems. Feedback control is more complex and may cause stability problems but also has the potential to give much better performance than is possible with open-loop control. If the process is naturally (open loop) unstable, feedback control is the only possibility to obtain a stable system and meet any performance specifications at all.

The controlled system, with the inputs u and v_i , obeys the command u gener-

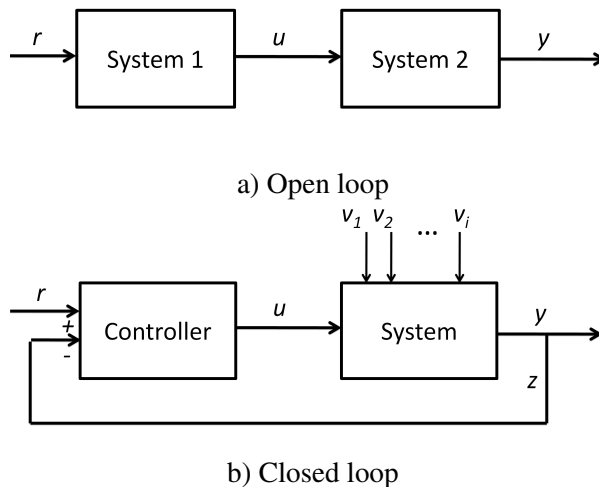


Figure 4.1: a) Open-loop diagram. The output u of the first system is the input to the second system, but the output y of system 2 is no longer the input to system 1; b) Closed-loop diagram. The output u of the first system is used as input for the second system and the output y of the second system also acts as the input to the first system. $v_1, v_2 \dots v_i$ are external perturbations that may affect the system.

ated by the controller and reacts to the exterior perturbations v_i . These perturbations acting on the system can be *additive* or *parametric*. Additive perturbations appear as a consequence to the change of the conditions in which the system is evolving, while parametric perturbations appear when the internal behavior of the system is changed, reflected as a change in the connection between the inputs and outputs or as a change in the internal evolution parameters of the system or system components. The action upon the additive perturbations are combined at the output of the controlled system with the action upon the controller command u , while the action of the parametric perturbations determine structural changes of the controlled system. The inverse connection z (called negative feedback) between the controlled system and the controller has major consequences for the global behavior of the system (stability, robustness, sensibility). If the controller is decomposed into components that process the information from the system y and the routines that ensure the required evolution

of the system, then the system is called a closed-loop system. The structure of such a system is depicted in Fig. 4.1b.

The controller processes the reference signal $r(t)$ and the output $y(t)$ and/or the error $\epsilon(t) = r(t) - y(t)$ using pre-defined internal laws. The error signal $\epsilon(t)$ is generated automatically inside the controller. Starting with the model in Fig. 4.1 and assuming the pre-defined reference working parameter $r(t) = y_r$, the deviation $\epsilon(t) = r(t) - y(t) = y_r - y(t)$ is a quality indicator of the internal state of the system with respect to the predefined working parameters. We define the system in Fig. 4.1 to be a self-adjusting system if, independently of the action of the exterior perturbations v_i , the following requirement is fulfilled:

$$\lim_{t \rightarrow \infty} \epsilon(t) = 0. \quad (4.1)$$

Self-adjusting systems can be classified with respect to the final output of the controller into two major classes:

- systems that reject the perturbation, for which the controller function tries to achieve in the end the output $y(t) = y_r = \text{constant}$ equal to the reference, independently of the external perturbations $v_i(t)$;
- follower systems, for which the controller function makes sure that the output $y(t)$ follows as closely as possible the reference value $r(t)$.

For the NuSTAR experiments at FAIR the chosen control system is EPICS. We propose an integrated solution that uses the concept of feedback loops in order to keep the system within the specified working parameters. "System" refers to the ensemble of all the constituents of a detection and acquisition chain which includes: experimental setup, the associated front-end electronics and all the interconnections that facilitate the communication between subsystems.

4.3 EPICS control system

There are several control systems on the market. One commonly used for experimental physics is Vista Control Systems® (Vsystem) [64]. Vsystem is a collection

of comprehensive, real-time, networked process control software tools known for performance and scalability, openness, support and training, and cross-platform/cross-version application. The software architecture of Vsystem makes it easy to incorporate computer models and complex control algorithms into the software. Current applications of Vsystem to experimental physics projects include satellite control room systems, nuclear power plant simulators, charged-particle accelerators and beam lines. The control system of the ISIS [65] pulsed neutron and muon source at the Rutherford Appleton Laboratory in Oxfordshire and the ISL-accelerator facility at the Hahn-Meitner-Institut Berlin are based on Vista Control Systems. The main disadvantage of Vsystem is that it is a commercial software and it is also not oriented to experimental physics applications. Moreover, these are only a small number of facilities using Vsystem, which limits the access to technical support.

The control system used in this work is EPICS [11, 66, 67, 68, 69, 70], a collection of software tools, libraries, and applications developed in collaboration between multiple institutions. EPICS is used worldwide to create real-time, distributed control systems for scientific instruments such as particle accelerators, telescopes, and other large scientific experiments. Current scientific instruments controlled by EPICS vary widely in scale, starting with small-scale experiments using a single VME [12] crate up to systems composed of hundreds of VME crates with thousands of channels. The big advantage of EPICS lies in making use of communication standards at every layer, which makes it possible to upgrade the system incrementally to add new equipment. This implies that each layer knows only the details of the communication protocol, and not the internal details of the other layers.

The following description of EPICS is based on documentation given in [11, 66]. Architecturally, the fundamental feature of EPICS is that it is fully distributed. This means that the operations are performed as much as possible locally. This achieves the goals of easy scalability and of incremental operation and upgrade. EPICS uses broadcasting to implement a discovery of a process for name-to-location resolution.

As seen in Fig. 4.2, EPICS uses three physical layers and several software levels. The physical front-end layer is typically built from VME/VXI [71] hardware crates,

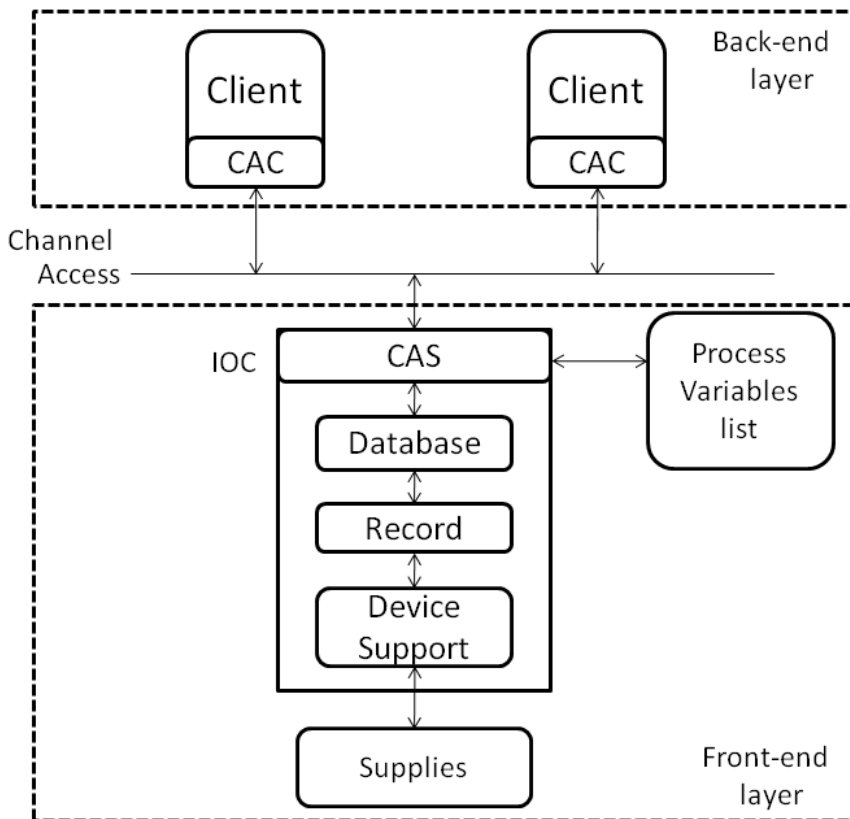


Figure 4.2: Functionality structure of EPICS. The physical layers are back-end layer and front-end layer, connected by the network. The channel access provides connectivity between the channel access client (CAC) and the channel access server (CAS). Each CAS has a list of process variables. An Input/Output Controller (IOC) contains one or several databases, that make use of records to access the supplies. The communication of the records to the supplies is done using device support.

CPU boards, and I/O boards and contains the supplies necessary to run the experiment. The physical back-end layer consists of just a set of PCs, which may be used e.g. for graphical data representation, advanced calculations, data monitoring, and storage. These two layers are connected by a network layer (e.g. ethernet) which ensures the communication between the front-end and back-end layers.

The two main structures of the EPICS software are *channel access* (CA) and the *Input/Output Controller* (IOC). At the highest software level is the channel access [68], with the *channel access server* (CAS) and the *channel access client* (CAC). Channel access is the backbone of EPICS that takes care of the communication protocols between clients and servers, hiding all the details of the TCP/IP network. CA acts as a firewall between all client and server code, ensuring their architecture independence, so they can run on different processors, and can even be from different versions of EPICS. CA allows for the transfer of different data representations, so clients and servers can mix ASCII data, integer data, and floating types (as well as *big-endian* and *little-endian*), making sure each application uses its natural units. Endianness refers to how bytes are ordered within a single 16-, 32-, or 64-bit word and is in this case the same as the byte order. The usual contrast is whether the most-significant or least-significant byte is ordered first within the larger data item, which is known as big-endian and little-endian, respectively. Software running in a VME crate uses also channel access to communicate with other crate-resident software.

EPICS Input/Output Controller (IOC) is an application that can run on many platforms (Linux or Windows PC, embedded systems, etc.) and is in charge of delivering information of the current system parameters over the network in regular intervals or under request. An IOC has three primary components. The heart of an IOC is a memory resident database together with various memory resident structures describing the contents of the database. Another important component of an IOC is the device driver support for interfacing to equipment. Each IOC provides a channel access server which is willing to establish communication with an arbitrary number of clients and provides network access to the database.

As seen in Fig. 4.2, the EPICS architecture permits a large number of clients to

run simultaneously, the actual number being limited by the resources of the network and the number of workstations. Clients may be dynamically executed or terminated at will; on execution they connect to all applicable IOCs and on termination they cleanly disconnect. This makes it easy to add new functionality in the form of additional application programs. The basic channel access client services are to locate the IOCs containing selected process variables and establish communication with each one, get the value plus additional optional information for a selected set of process variables, change the values of selected process variables. A Process Variable (PV) is a named piece of data associated with the machine (e.g. status, readback, setpoint, parameter). Channel access does not provide access directly to the database records, but making use of the communication protocol available at this level. This allows new record types to be added without impacting any software that accesses the database via channel access. A channel access client can communicate with multiple IOCs having differing sets of record types.

The channel access server runs on the target central processing unit embedded in every IOC, whether a VME/VXI crate or PC. It isolates all clients from the database level below. This server cooperates with all CA clients to implement a call-back and synchronization mechanisms. Even though CA clients are typically independent host programs that call channel access routines through a shared library, the CA server runs just one copy of itself on each network node.

An important part of the software is the database [72], which is really the heart of EPICS. Using a host tool, the database is described in terms of function-block objects called ‘records’. About 50 record types exist (and can be extended) for performing tasks like analog input and output, binary input and output, building histograms, storing waveforms, moving motors, performing calculations, implementing proportional - integral - derivative controller loops, driving timing hardware and other tasks. Records that deal with physical sensors provide a wide variety of scaling laws, allow smoothing, provide for simulation and accept independent hysteresis parameters for display, alarm, and archive needs. Besides its name, a record has a value, and perhaps other attributes such as units or maximum/minimum. By accessing the record name

and the attributes the CA connects a client to a server. A database is effectively a high-level program and, because records in one database can be linked with records in another database, a collection of databases can be viewed as a still higher-level program.

An example of a record is the analog-output record, whose fields include: an analog value, the units in which the value is expressed, limits on the value, fields describing how the value should be displayed to the user, fields and attributes describing when the record functions should be executed, fields for the private use of the record functions, fields used by EPICS core software to manage the execution of those functions, a field naming the device-support module that is to convey the analog value to hardware or to another record and fields for the private use of that device-support module.

Record activity is initiated in several ways: from I/O hardware interrupts, from software ‘events’ generated by clients, when fields are changed from a write command or using a variety of periodic scan rates. Records support a great variety of data linkage and flow control, such as sequential, parallel, and conditional. Data can flow from the hardware level up, or from the software level down. Provision is made for local and global simulation, in which additional records stand in for hardware input/output records. Records validate data passed through from hardware and other records as well as on internal criteria, and can initiate alarms for uninitialized, invalid, or out-of-tolerance conditions.

The bottom level of software is the device driver layer. A large list of drivers has been written, usually in C language, for many popular VME and VXI interface boards.

The speed of EPICS depends mainly on the used hardware (e.g. the type of the central processing unit) and the speed of the network. For a machine running a Vx-Works [73] operating system with a PPC750 CPU [74] with an internal clock speed of 450 MHz, EPICS can perform up to 100000 recorded events per second. However, database design and periodic scanning effects dramatically affect the speed of the system.

In summary, EPICS provides a software toolkit for implementing control systems for a large class of experimental setups. The intense collaboration between scientific laboratories, industrial partners, and other users helps to increase the class of available applications. EPICS control systems can achieve modularity, scalability, robustness, and high speed in hardware and software, yet remain largely vendor and hardware-independent. EPICS provides the integration of several data acquisition-bus standards. The software-development environments for intelligent local controllers and workstations can be identical. Good documentation, training, and support are available. Standard systems can be configured with text editors and other simple tools, yet full customization is available to sophisticated sites.

At the moment the LabView [75] control system is used at GSI. LabView is a control system with the same functionality as EPICS. In the last version a connection to EPICS has been developed for LabView by National Instruments and it has been included in the standard package. This allows for direct link between the two systems which represents a huge advantage for both, since it will allow for the reusability of the already-implemented systems in LabView. The major difference is the easy achievable scalability that EPICS offers and its device support, whose functionality can be easily extended by adding new records in the database. All these advantages make EPICS the best choice for the control system of large-scale experiments.

4.4 Realization of a self-adjusting control loop embedded in front-end electronics

In the framework of the NuSTAR [3] project at FAIR [1] we have to develop control systems which integrate automated calibration, optimization and adaptive stabilization, basically constituting the characteristics of intelligent sensors and cognitive systems. In the controls concept for the NuSTAR experiments we are looking into the conditions of the hardware structure, the initialization and monitoring of the system along with the optimization and calibration of the detectors. Based on the digitized detector signal/pulses, online feedback will be provided based on our control tech-

niques which support a strong correlation between signal characteristics and detector settings.

Making use of the control techniques, we have built a self-adjusting system. The working principle of this system is depicted in Fig. 4.3. We have a single detector unit, irradiated by a gamma emitting ^{137}Cs source. The signal from the detector is analyzed using the methods described in the previous chapter: baseline follower, $k\sigma$ triggering, moving window deconvolution, moving average, box trigger and pile-up compensation. As a result of this analysis, a spectrum is constructed which in this case contains a single peak. These data are fed to the peak-sensing algorithm which can return the number of peaks in the spectrum and the positions of the maximum values of the peaks. For the peak with the highest channel number, the quality factor RER (Relative Energy Resolution) is returned. This is defined as:

$$RER = \frac{FWHM}{i_{max}}, \quad (4.2)$$

where $FWHM$ is the full-width half-maximum of the peak, and i_{max} is the channel number corresponding to the centroid of the peak.

The control function is built in this case on the quality factor of the peak. However, any other control parameter that reflects the quality of the spectrum can be used. Other quality factors that could be considered are, for example, the behavior of the peak related to the rate change and the settings for the MAF related to the change in rate. The quality factor RER depends on the bias voltage (HV) applied to the detector in a non-linear way. The open-loop behavior of the system is given by the dependence of RER on the voltage applied to the detector. The type of feedback that one can build depends crucially on the open-loop function. We can conclude that we have implemented a feedback method based on rejecting perturbations and disturbances: if the quality factor RER does not match the reference value, the system is forced back to the reference voltage for which the detector gives the best performance.

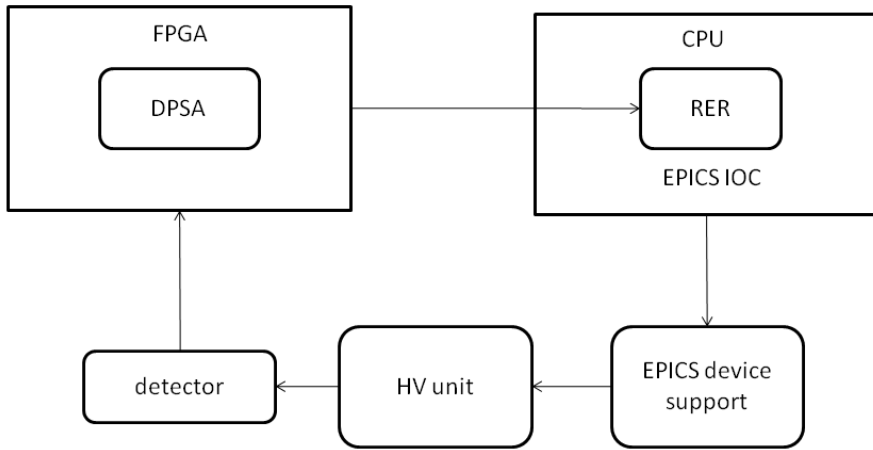


Figure 4.3: Organization of the self-adjusting control loop. The FPGA performs the Digital Pulse-Shape Analysis (DPSA) of the signal read from the detector. The result is passed on to the CPU which evaluates the RER and based on the result the voltage of the HV unit is adjusted with the help of EPICS device support.

4.4.1 Device support

The employed power supply is an ISEG, HV-Power Supply, CPS-Series, CPn 30 405 245 [76]. In order to build the control loop, one needs to be able to control the power supply from EPICS. Although a large class of supplies have been implemented in EPICS, the specific high-voltage unit used by us was not. The first step required was to write a protocol file to make sure we are able to communicate with the power supply from the computer. Due to the fact that the HV unit output port is a CAN port, a LAWICELAB adapter CAN232-to-serial has been used, that plugs into any PC COM port or any other RS232 port in an embedded system and gives an instant CAN connectivity. This means that the output port of the HV unit can be treated by software as a standard COM Port (serial RS232 port), with the advantage that sending and receiving can be done in standard ASCII format. The CAN232 handles both the 11 bit ID format (standard) as well as the 29 bit ID format (extended), built

in FIFO queues, extended info/error information and simple power-up through a few commands. A transmit command via the CAN232 starts with the letter *t*, followed by a set of hexadecimal numbers representing the CAN command for the HV unit. The CAN232 replies back when sending a frame to a *t* command with a letter *z*, followed by the carriage return, making it possible to recognize that a transmit command was sent out successfully from the CAN232.

The communication between the controller (which can be the PC or the FPGA) and the HV module works according to the Device Control Protocol DCP, which has been designed for the use of multi-level-hierarchy systems for instruments. The DCP protocol works according to the master-slave principle. Therefore, the controller, which is always on a higher hierarchy, is the master, while the device (as a front-end device with intelligence), works as the slave.

The data exchange between the controller and the front-end device works with the help of data frames. Each frame is built with 2 hexadecimal digits representing the device address, one direction bit DATA-DIR, another digit indicating the number of data bytes to be further transmitted, and further data bytes representing the value of the read or written voltage or current, depending on the transmitted command. The direction bit DATA-DIR defines whether the data frame is write or read-write access.

Commands have been implemented to turn the power supply on/off, to check if the unit is on/off, to set the voltage and read the current value within the power supply, to test for the status of the unit, to set and read the ramping speed and to log the controller on/off. All these commands have been embedded in EPICS in the course of the present project and are available as process variables.

4.4.2 Peak-sensing algorithm

We have implemented in EPICS a peak-sensing algorithm to evaluate on-line the quality factor RER. The main input of the code is the histogram collected by the FPGA, which is transmitted as a process variable to the peak-sensing algorithm. The histogram is read periodically from the FPGA. The amount of time between two consecutive read operations is strongly related with the rate of particles that impinge

on the detector. The higher the rate, the smaller the acquisition time can be set. The collection time can also not be very long, because the control loop will lose sensitivity to the changes in the voltage on the high-voltage unit. After the data have been passed to the peak-sensing process variable, the algorithm identifies the expected number of peaks by their starting and ending positions. The starting and ending positions of the peaks are identified as the points where the numerical derivative of the curve changes sign. For the peak with the largest channel number, corresponding to the highest energy, the control algorithm returns the quality factor RER .

The fact that there are natural fluctuations in the data may lead to misidentifying peaks in the measured histogram. Therefore, the first step is to apply a moving average filter to the histogram to reduce the local fluctuations. Depending on the time between two consecutive readings and the rate on the detector, more than one pass of the moving-average filter may be required. For the next step, we calculate the first derivative of the filtered data and find the points of zero crossing. These points are exactly the beginning and ending of each peak. For the peak with the highest channel number, we identify the maximum and its position, as well as the position of the half-maximum.

There are two sources of error in the calculation of the RER . The first error comes from applying the moving-average filter to the data. Each pass of the filter causes a broadening of the peak. This leads to a slightly higher value for the RER than the one obtained by a proper Gaussian fit of the original data. However, this error is systematic and is the same for different measurements taken for the same time duration and at the same voltage. This can be seen in Fig. 4.4, where the influence of the number of passes of the moving-average filter on the RER is shown. Even though the value of RER increases with the number of passes, around the optimum value of the voltage this deviation becomes very small. We apply a number of three passes to each collected histogram, since for three or more passes the RER depends smoothly on the voltage. Applying more repetitions will increase the time required for the evaluation of the RER , which is very important for systems with a large number of channels. Another source of error is the asymmetry in the shape of the peak, which

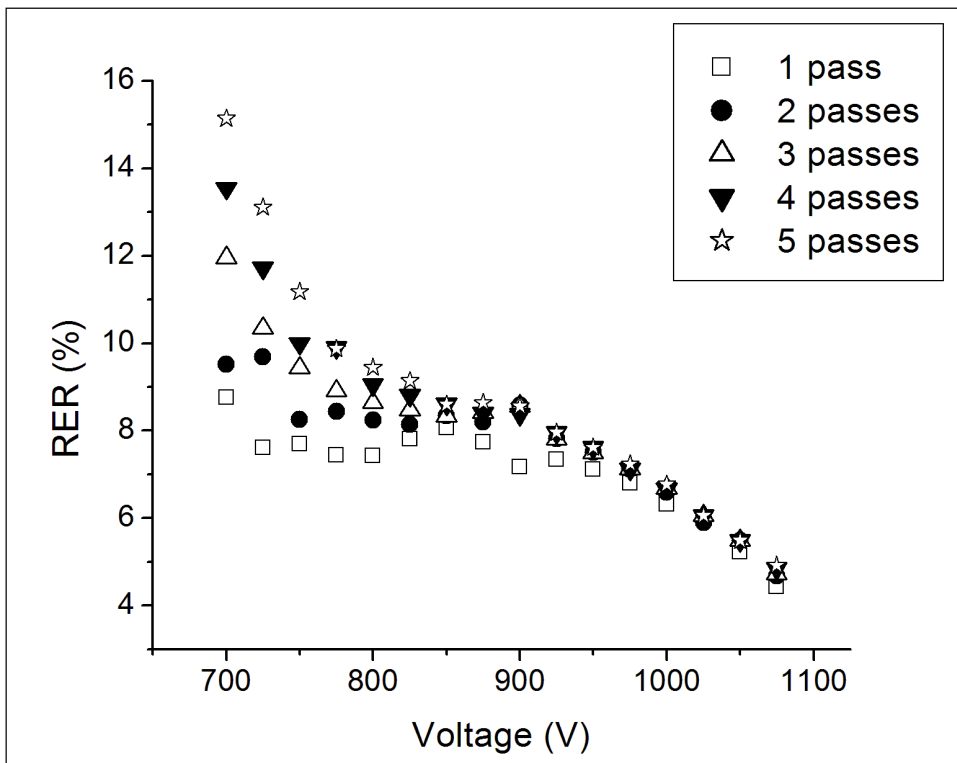


Figure 4.4: Dependence of the calculated RER value on the applied detector voltage for different number of passes of the moving-average filter.

can be reduced by increasing the time between two consecutive readings.

Each time the histogram is passed on to the process variable that calculates the RER, the histogram is reset and data start to be collected again. Therefore, the RER factor is being calculated only from the latest data and not from the total spectrum collected from the beginning of the measurement.

4.4.3 System dynamics

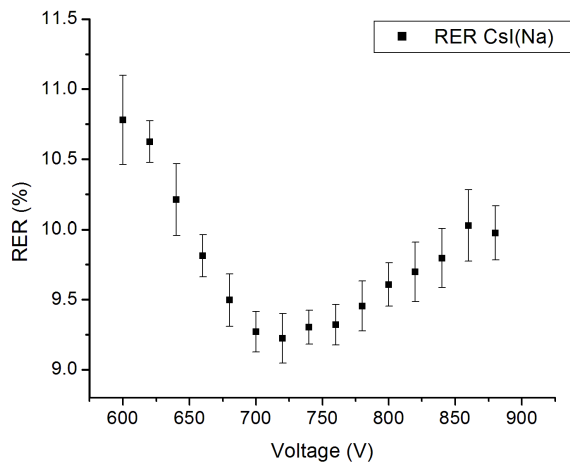
The first step in implementing a good feedback function consists in studying the system in an open-loop environment. The system looks just as in Fig. 4.3, but without the connection from the EPICS IOC that calculates the RER of the detector, i.e. ba-

sically without the feedback connection. The used detectors are a CsI(Na) scintillator connected to a XP2042B photomultiplier [77] and a NaI(Tl) connected to a XP 2950 photomultiplier [78] that are powered by the ISEG HV unit described in Sec. 4.4.1.

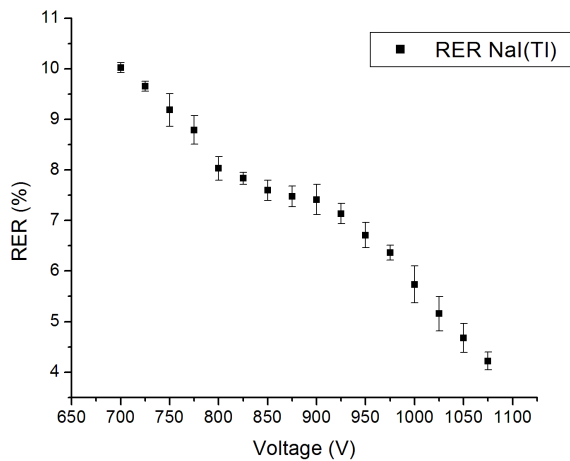
In order to establish the optimum working point for the detectors, we have performed online measurements using a ^{137}Cs source to irradiate the detectors. The voltage on the power supply has been set in the range from 600 V up to 880 V, in steps of 20 V for the CsI detector and from 700 V up to 1075 V in steps of 25 V for the NaI detector. Several measurements have been performed at each value of the voltage, each measurement with a duration of 3 minutes. The black data points in Fig. 4.5a and in Fig. 4.5b are the result of the measurements with the CsI(Na) and the NaI(Tl) detectors, respectively, performed at each voltage value. The error bars represent the standard deviation of the data.

From Fig. 4.5a and from Fig. 4.5b it is clear that the CsI(Na) detector has the best performance for 730 V and the NaI(Tl) has the best performance at 1075 V, therefore, those reference points have implemented for the data. Even though the *RER* value decreases monotonically with higher voltage for the NaI(Tl), the 1075 V point is at the high end of the operating range of the PMT, therefore one can not search a better value for *RER* beyond this voltage value. As discussed in section 4.2, we have implemented a system with rejection of the perturbation. If the value of the *RER* does not fit the expected value within the allowed tolerance which is preset based on the fluctuations of the system, the voltage of the power supply is forced back to the optimum value.

We have tested the system for hysteresis, in order to check that the open-loop function is the same, if one ramps up the voltage or ramps it down. The results have been plotted in Fig. 4.6a for the CsI(Na) and in Fig. 4.6b for the NaI(Tl) detectors. The data points shown by filled squares are the results of the *RER* as one increases the voltage. The data points represented by filled circles are the *RER* values as the voltage is decreased. The data points represented by filled triangles are the *RER* values as the voltage is increased again after a voltage decrease. From the two plots we can see that the two sets of data agree within the error bars, so we may conclude

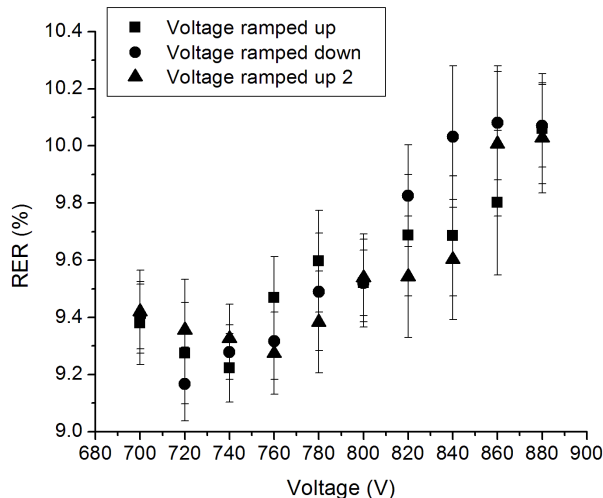


a)

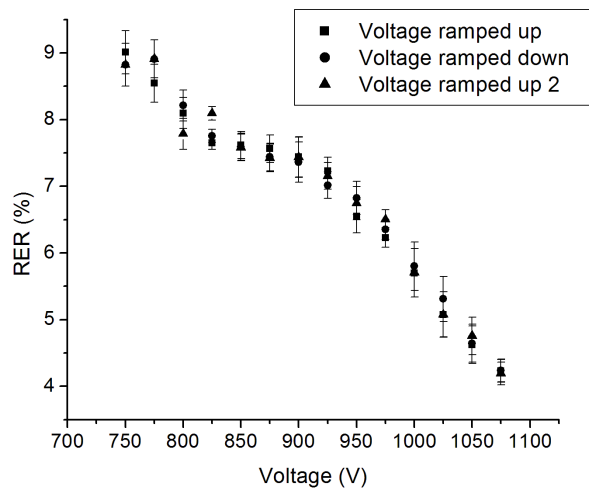


b)

Figure 4.5: RER of two different scintillator/PMT combinations as a function of the detector supply voltage value for the CsI(Na) (a) and NaI(Tl) (b) detectors. The black data points are the results of several measurements performed at each voltage with the error bar as the standard deviation.



a)



b)

Figure 4.6: Test of the system for hysteresis for the CsI(Na) (a) and NaI(Tl) (b) detectors. The data points shown by filled squares are the results of the RER as one increases the voltage. The data points represented by filled circles are the RER values as the voltage is decreased. The data points represented by filled triangles are the RER values as the voltage is increased again after a voltage decrease.

that no hysteresis is present.

4.4.4 Self-adjusting control loop

Having built both the device support for the ISEG HV power supply, such that it can be controlled from EPICS, and the peak-sensing algorithm, which was also embedded into an IOC, we have constructed an interface in LabView that enables access to all the control parameters described in this chapter. Fig. 4.7 is a snapshot of the interface during one of the performed test measurements.

To prove the functionality of the complete system that we built, we performed online measurements during which we influenced the conditions of the measurements such that the system needed to react as designed. In Fig. 4.8 the RER for the CsI(Na) detector and the detector supply voltages are plotted as a function of time for two different data-collection times of 180 s and 45 s, respectively. We have set the working point for this detector at 740 V and the system will compute the RER every 180 s and 45 s for the first and the second example, respectively. As long as there are no disturbances in the system which affect the RER, the system keeps running without any change. At time $t=1080$ s, we changed the voltage on the HV unit on purpose to 640 V for 180 s collection time. In this case, the RER obtained will be outside the preset working conditions, so the system would have to detect this change at the next RER computation and react by changing back the voltage to the working point and therefore producing the required RER. This sequence of events is evident in Fig. 4.8. At the beginning the RER is stable at 9%; after the settings have been disturbed the RER=11% is detected. Consequently, the system detects that the optimum working conditions are not met, and the voltage is automatically changed to the previous working setting and, therefore, the RER is restored back to 9%. Similar behavior can be seen also if we reduce the collection time to 45 s for disturbances introduced at 360 s and 540 s.

In Fig. 4.9 the same functionality is presented, except that in this case the measurement was done with the NaI(Tl) detector with the optimum working point at 1075 V. The sequence of events in Fig. 4.9 is similar to the one in Fig. 4.8: at the beginning

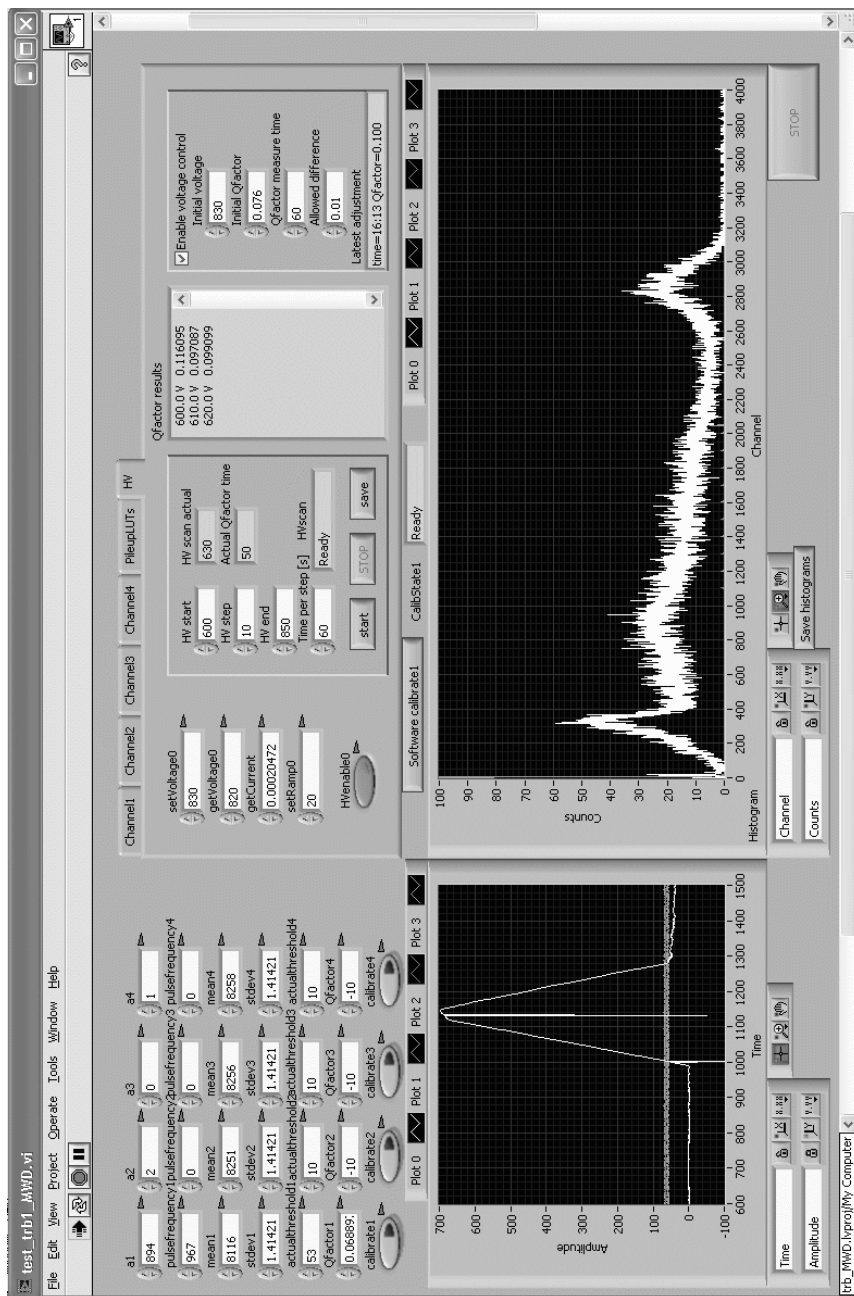


Figure 4.7: LabView interface to the control loop.

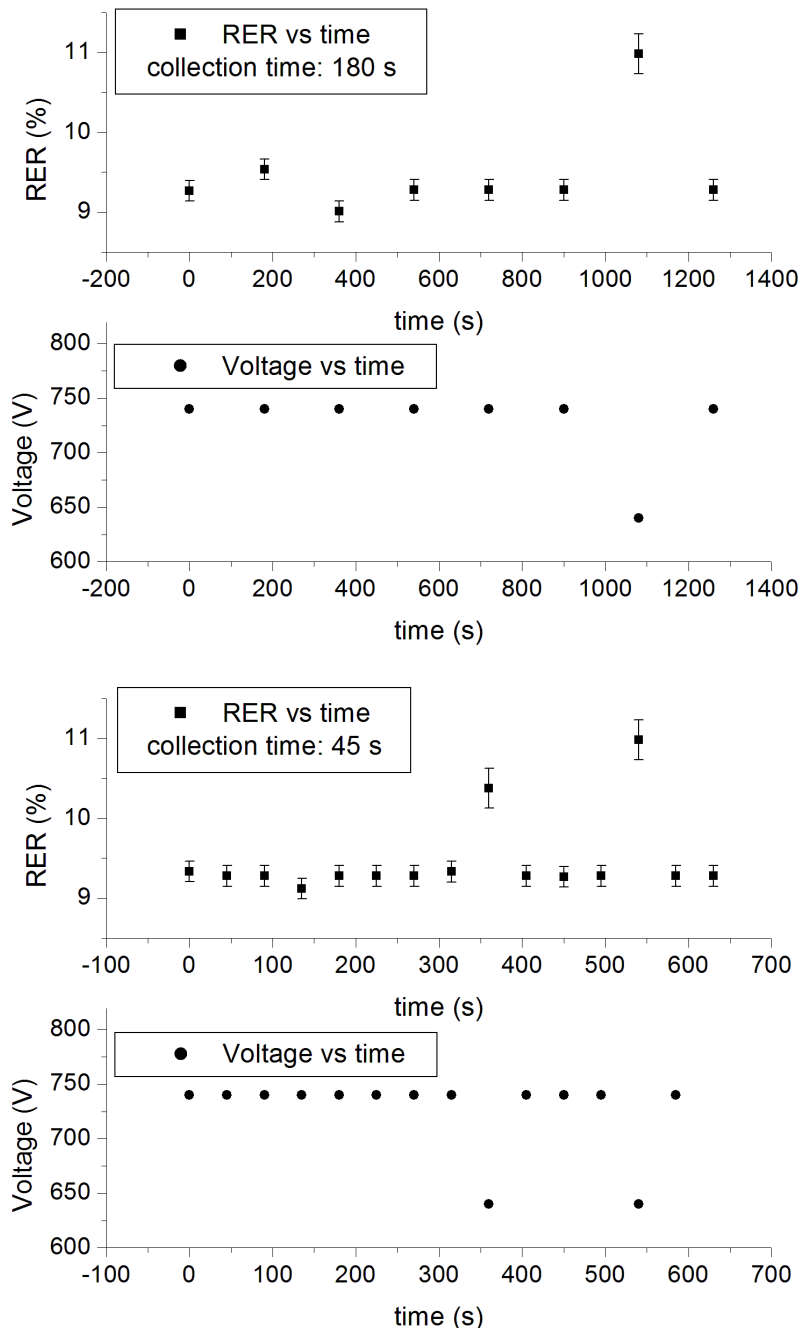


Figure 4.8: Self-adjusting control loop for the CsI(Na) detector for two different data-collection times.

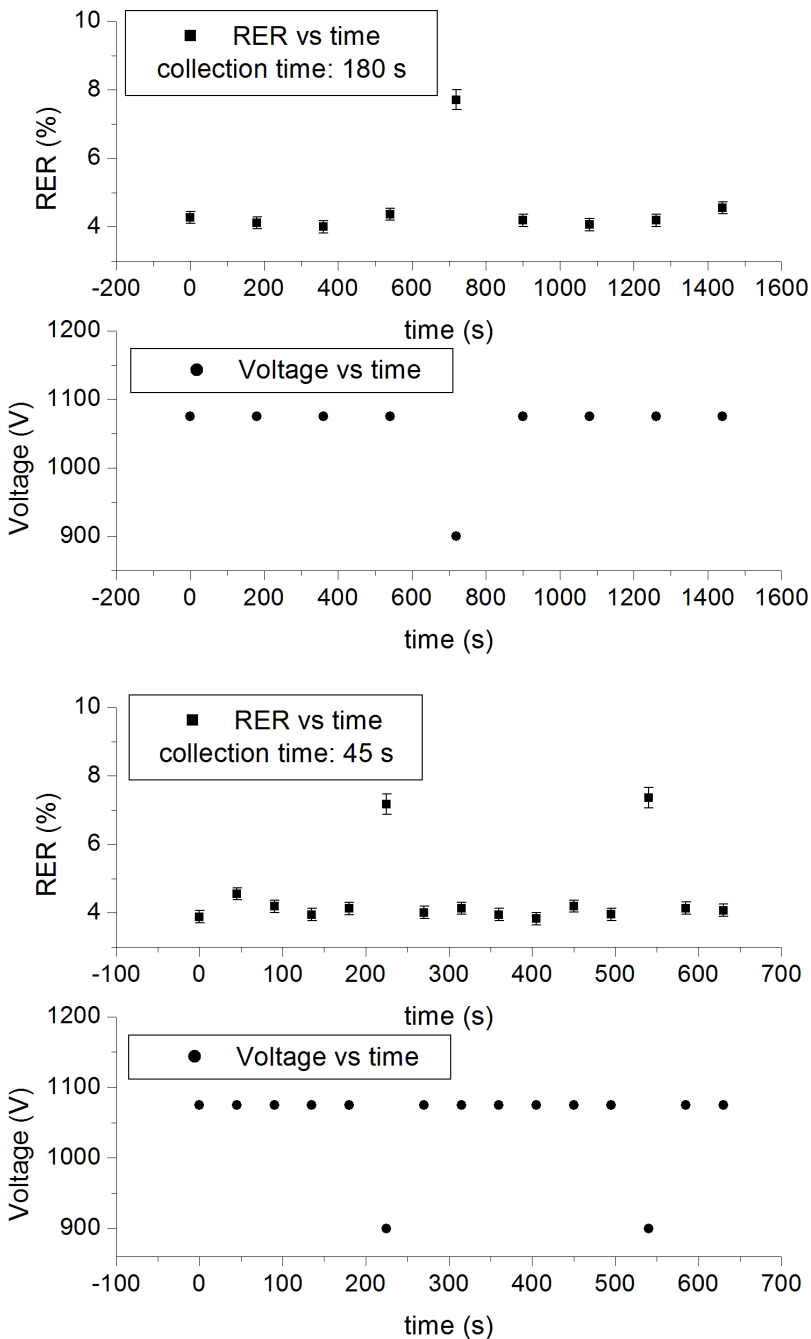


Figure 4.9: Self-adjusting control loop for the NaI(Tl) detector for two different data-collection times.

the RER is stable at 4%, after the settings have been disturbed the RER is detected to be 7%, so the system detects that the optimum working conditions are not met, and the voltage is automatically changed to the previous working setting and, therefore, the RER recovers at 4%. Again, the same behavior can be seen also if we reduce the collecting time to 45 s.

The measurements were also performed at the same time for both detectors, each of the detectors being handled by a different FPGA. Both detectors were set at their specific working points. Afterwards, we varied the voltage for each detector at a time and noticed that the system corrected the affected detector, while the second detector continued working unaffected. We also changed the voltage on both detectors at the same time and the system applied, as expected, the correction for both detectors simultaneously. This test underlines not only that the control loop works as designed but that the system is scalable and more boards could be added and enabled to work at the same time.

4.4.5 Time aspects/constraints in the self-adjusting control loop

In order to check the performance of our system, we have measured the time required for the processor to calculate the RER value. Even though the time for calculation is highly dependent on many factors we did a measurement that can give an estimate of this time for two different situations. The most important factors are: the amount of data that is sent over the network while calculating RER, the acquisition rate, and even the peak position. Since we deal with a UNIX system, we know that in the same time with the RER calculation there is some data traffic that slows down the calculation. To be more explicit, one could compare this situation to the situation when we are copying a large amount of files on our computer, but at the same time we are running other applications. The processor will run of course much slower in this case, slowing down some applications. However, in the final design this setback will be avoided and will impose no limitation whatsoever because the data traffic will be routed through an optical fiber (for example) and, therefore, not interfere with the processor calculations. We have measured the time required for the processor

to calculate the RER for one, two, three and four detectors at two different rates. The four detectors were connected to the same FPGA and processor. The results are shown in Table 4.1. From the results it is obvious that the time required for the calculation of the RER value is a lot smaller than the collection time for calculating the RER. Rate 1 in Table 4.1 corresponds to: 1.2 kHz, 1 kHz, 1.2 kHz, and 1.5 kHz for channels 1, 2, 3, and 4, respectively. Rate 2 corresponds to: 1.7 kHz, 3.3 kHz, 1.7 kHz, and 5 kHz for channels 1, 2, 3, and 4, respectively. The collection time for these measurements was 40 s. The hardware systems that are currently applied enable to use a maximum of 4 channels for the TRB and 8 channels in the case of the SIS3302. By increasing the number of channels that correspond to a single processing unit the calculation time would eventually reach the collection time and, therefore, would become a time constraint. However, this would require that the number of channels/processor exceed the maximum number that is allocated at the moment or that are currently designed in the framework of our project.

Table 4.1: The time required for the processor to calculate the RER value for a number of channels. The times given are the average of 20 measurements for each number of channels. Rate 1 and Rate 2 correspond to typical low and high rates (see text for details), respectively.

Number of channels	Rate 1: Average time/channel (s)	Rate 2: Average time/channel (s)
1	0.54	0.55
2	0.61	0.66
3	0.65	0.82
4	0.72	1.37

Apart from the calculations performed on the CPU, another possibility for time limitation could be the control system itself. However, EPICS presents no limitations as a control system for the purpose that we have used it for. In Table 4.2, the dependence of the number of records processed in one second is shown for different applied hardware systems. We can see that depending on the machine, processor,

CPU type and CPU speed the number of records that can be processed varies considerably. Further details about the processors mentioned in Table 4.2 can be found in [74, 79, 80, 81, 82]. This shows clearly that the speed of EPICS is highly hardware dependent.

Table 4.2: EPICS speed depending on the applied hardware system [83].

Machine	OS	CPU	Speed	Records/s
MVM167	VxWorks	68040	33 MHz	3.000
MVME2306	VxWorks	PPC604	300 MHz	20.000
MVME5100	VxWorks	PPC750	450 MHz	100.000
PC	Linux	P II	233 MHz	10.000
PC	Linux	P4	2.4 GHz	100.000

We have shown that a self-adjusting control loop can be implemented inside EPICS and that it can be related to physics parameters such as the energy resolution. Furthermore, the implementation in EPICS is scalable, does not impose critical time-related constraints, and by the design of EPICS it allows for further extensions of the feedback parameters.

5

Overall testing of the signal processing

5.1 Results from test measurements performed with a radioactive source

This chapter is dedicated to the results obtained in off-line and in-beam experiments, which were designed to test the functionality of the Digital Pulse-Shape Analysis (DPSA) described in chapter 3. The data were obtained using a CsI(Na) crystal attached to a XP2042B photomultiplier [77]. This PMT is a 10-stage, 39mm (1,5") diameter, round tube, that has a spectral range of 270 nm to 650 nm with a maximum sensitivity at 420 nm. For the off-line measurements the digital pulse-shape analysis routines have been implemented on an electronics board featuring a Virtex 4 LX40 FPGA [10] mounted on the General Purpose Trigger and Readout Board (TRB) [9]. The QuadADC [41] board which contains four ADCs (corresponding to four readout channels) is connected to the TRB. The FPGA code reads 14 bits of parallel data from the four ADCs, performs a baseline restoration, triggers upon the occurrence

of pulses and extracts the pulse amplitude using specifically designed filters. The number of trigger events is recorded and corrected for pile-up. All of this information can be stored as a binary or text file on a PC. The data from our detector is digitized in one of the four ADCs.

5.1.1 Data

Several ^{137}Cs and ^{60}Co spectra have been recorded at KVI, over a wide range of rates using the XP2042B-CsI(Na)-combination, which was covered in a conventional μ -metal shield. During operation, the detector was connected to an ISEG high voltage power supply [76] (CPS-Series, CPn 30 405 245) at a voltage of 800 V. The data have been taken using two of the four ADC channels, with the pile-up compensation activated on one of the channels only. Fig. 5.1 shows the measurements performed with a ^{137}Cs source at 6.5 kHz, 12.2 kHz, 21 kHz, 29.5 kHz, 40 kHz and 45 kHz. Fig. 5.2 shows the measurements performed with a ^{60}Co source at 4 kHz, 7 kHz, 10 kHz, 17 kHz, 21 kHz and 25 kHz. The rates were changed by varying the distance of the source with respect to the detectors. The black line shows the spectrum at the specified rate taken without pile-up compensation, whereas the gray line shows the data with pile-up compensation. For all the spectra, the measuring time has been normalized to a 300 s acquisition time.

In both sets of spectra, the full energy peak(s) as well as the Compton continuum are clearly observed for all rates. Also the effect of the pile-up compensation routine is plainly visible on the full energy peak(s) but also at energies above.

5.1.2 Energy resolution

We have calculated the improvement in energy resolution of the 662 keV photopeak of the ^{137}Cs source when using the pile-up compensation. The peaks have been fitted with a Gaussian and a linear background, for spectra in both ADC channels. The energy resolution is defined as

$$\epsilon = \frac{FWHM}{E}, \quad (5.1)$$

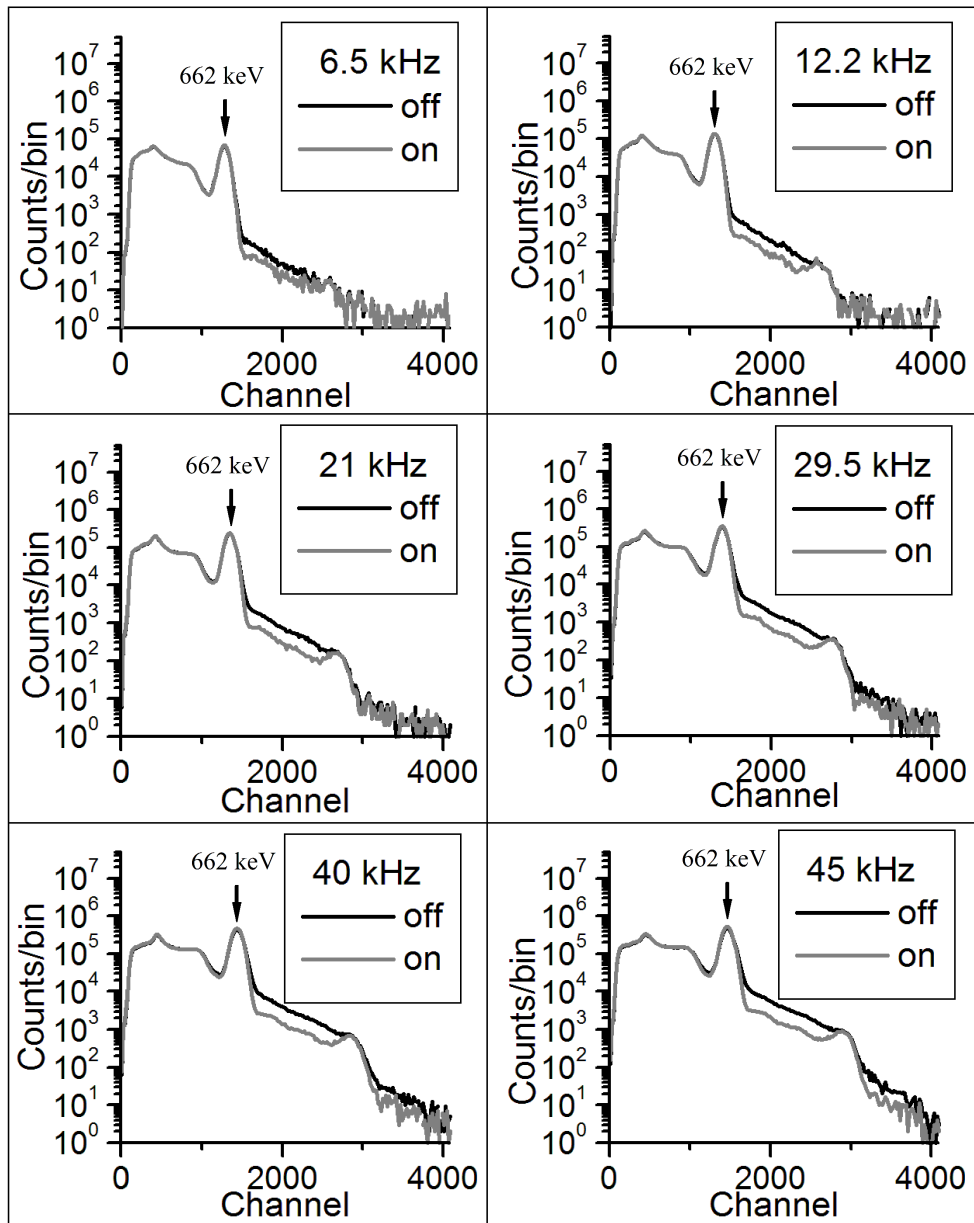


Figure 5.1: Measurements with a ^{137}Cs source performed with a $\text{CsI}(\text{Na})$ crystal. The black line represents the spectrum measured without pile-up compensation. The gray line is the same measurement when pile-up compensation has been activated. The bin size is 20 channels.

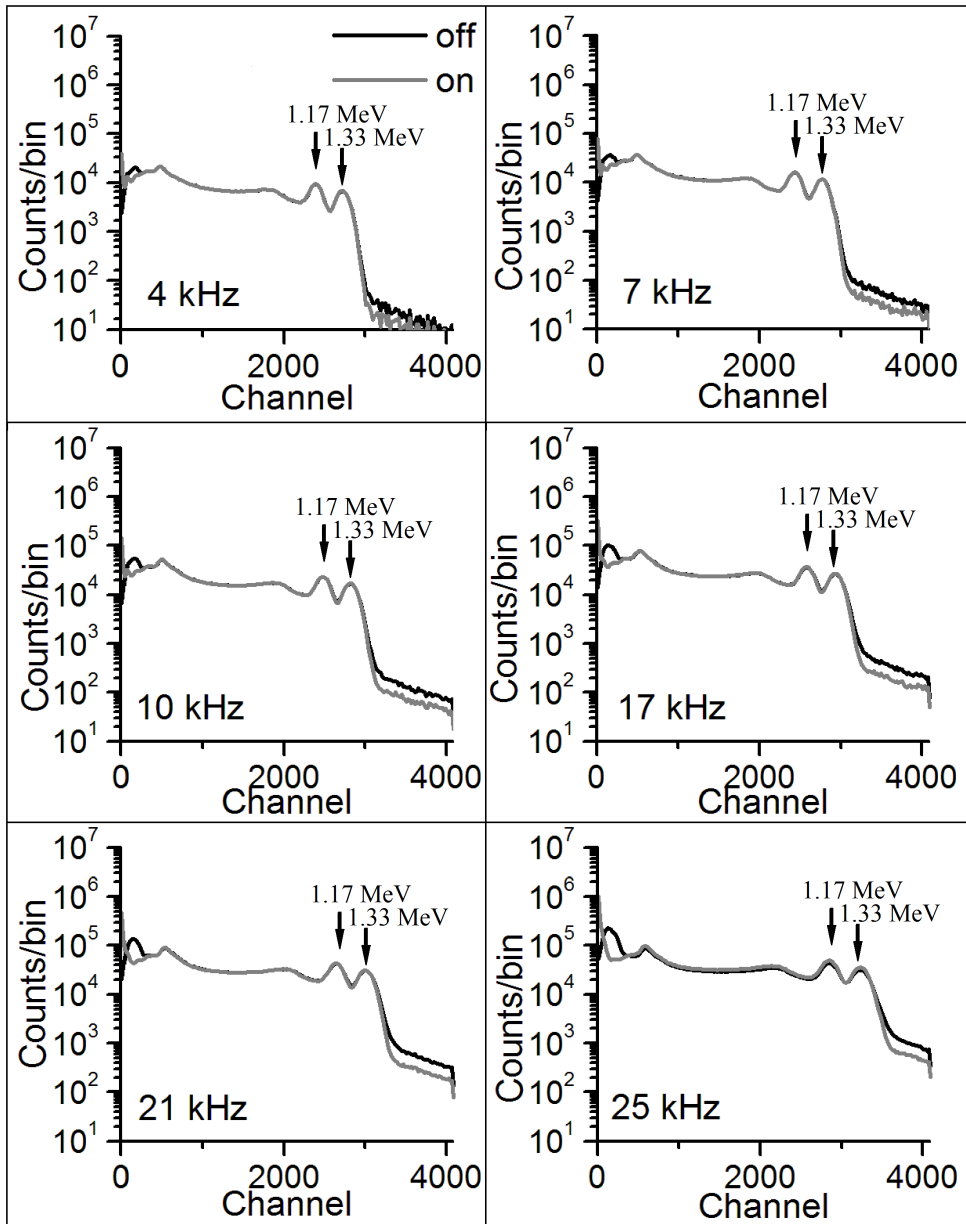


Figure 5.2: Same as Fig. 5.1 but for a ^{60}Co source.

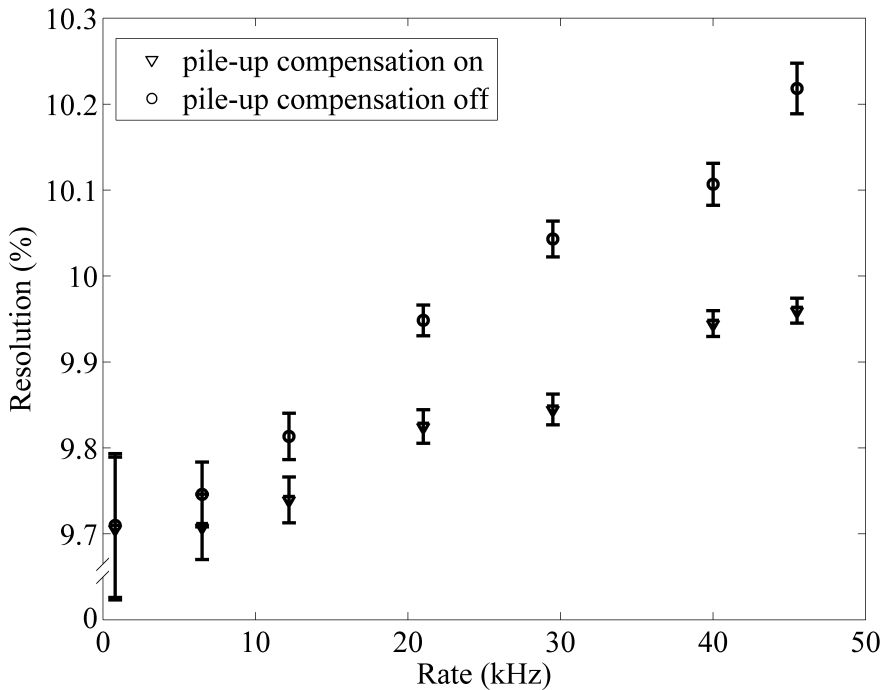


Figure 5.3: Energy resolution of the 662 keV photopeak of the ^{137}Cs as a function of the rate. The circles are the energy resolution for the spectrum taken without pile-up compensation. The triangles are the energy resolution when the pile-up compensation has been activated. The error bars are the one σ statistical errors.

where FWHM is the full width at half maximum and E is the energy of the centroid.

In Fig. 5.3 the energy resolution as a function of the rate has been plotted. The data are shown with pile-up compensation (triangles) and without it (circles). As the rate increases, the energy resolution gets degraded. By using the pileup compensation routine, more of the pulses in the pile-up regime are moved towards lower values of the energy, thus leading to a narrower photopeak. As seen from Fig. 5.3 the energy resolution is improved slightly at large rates, where the width of the peak has been most affected by the pile-up. The results are also tabulated in Table 5.1.

Table 5.1: Improvement in the energy resolution of the 662 keV photopeak of the ^{137}Cs source, measured with a CsI(Na) scintillator. The first column shows the rate at which the resolution was measured. The ϵ_{on} column shows the energy resolution with pile-up compensation while the column ϵ_{off} shows the energy resolution without the pile-up compensation. In the last column the difference between ϵ_{on} and ϵ_{off} is calculated.

Rate (kHz)	$\epsilon_{on}(\%)$	$\epsilon_{off}(\%)$	Improvement(%)
0.8	9.71	9.71	0
6.5	9.72	9.75	0.3
12.2	9.75	9.82	0.7
21	9.83	9.95	0.12
29.5	9.85	10.05	0.20
40	9.95	10.12	0.17
45.5	9.97	10.23	0.26

5.1.3 Peak efficiency

The advantage of using the pile-up compensation method is the improvement of the peak-to-total ratio, which is the fraction of the number of full-energy events out of the total number of identified particles. At higher rates, a lot more pulses are affected by pile-up and, as a consequence, they are shifted out of the photopeak area. When applying the pile-up compensation, part of the pulses are shifted back into the photopeak, thus leading to an increase in the number of counts.

As mentioned in section 5.1.1, we use two of the ADC channels of the board. The information from each channel is saved into files containing the amplitudes a_i and time stamps t_i of each pulse, where one of the ADC channels contains the amplitudes obtained after applying the pile-up compensation. The values of the amplitude A_{off} before applying pile-up compensation can be matched to the amplitude A_{on} obtained after pile-up compensation. Fig. 5.4 shows the distribution of the pile-up corrected amplitude A_{on} vs. the pile-up uncorrected amplitude A_{off} . The general trend is that an amplitude A_{off} will move to smaller values after applying pile-up compensation.

Table. 5.2 shows the dependence of the peak-to-total ratio on the rate for spectra

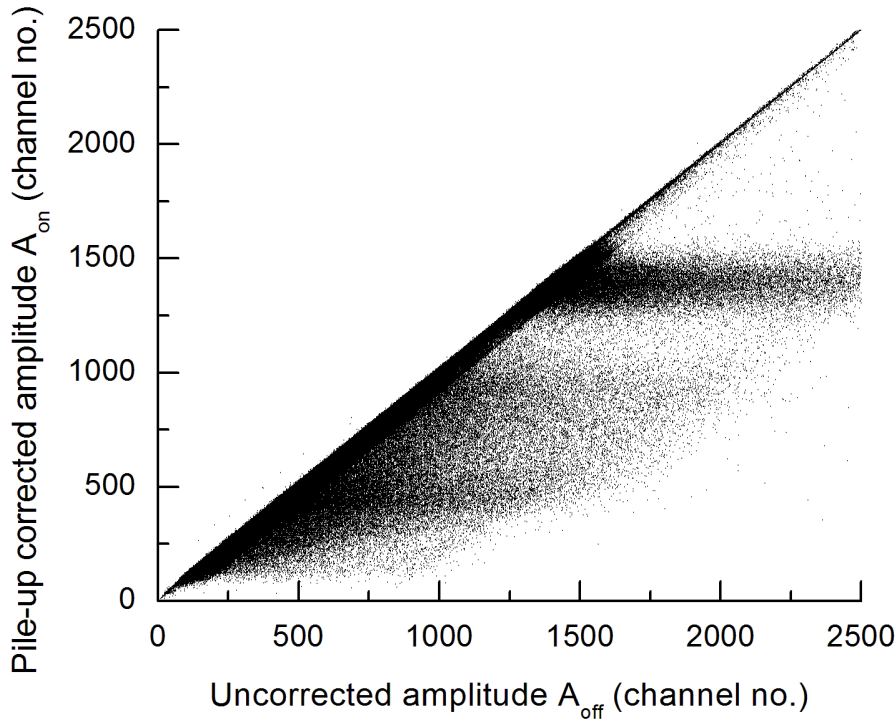


Figure 5.4: Change of the amplitudes A_{off} after applying pile-up compensation for an incoming rate of 21 kHz.

taken with and without pile-up compensation. The improvement in the peak-to-total ratio is given by:

$$\text{Improvement} = \frac{r_{on} - r_{off}}{r_{off}} \quad (5.2)$$

where r_{on} and r_{off} are the peak-to-total ratios of the photopeaks in the spectra taken with and without pile-up compensation, respectively.

Fig. 5.5 shows the improvement in the number of counts in the 662 keV photopeak of ^{137}Cs as a function of the rate. This plot points out clearly that the improvement increases with the rate. The improvement increases with the rate and reaches 8.06% at 45.5 kHz.

Table 5.2: Improvement in the peak-to-total ratio of the 662 keV photopeak of ^{137}Cs source, measured with a CsI(Na) scintillator.

Rate (kHz)	$r_{off}(\%)$	$r_{on}(\%)$	Improvement(%)
0.8	19.11	19.13	0.09
6.5	22.40	22.59	0.83
12.2	24.37	24.79	1.68
21.0	25.93	26.77	3.23
29.5	26.53	27.71	4.44
40.0	26.76	28.89	7.95
45.5	27.22	29.42	8.06

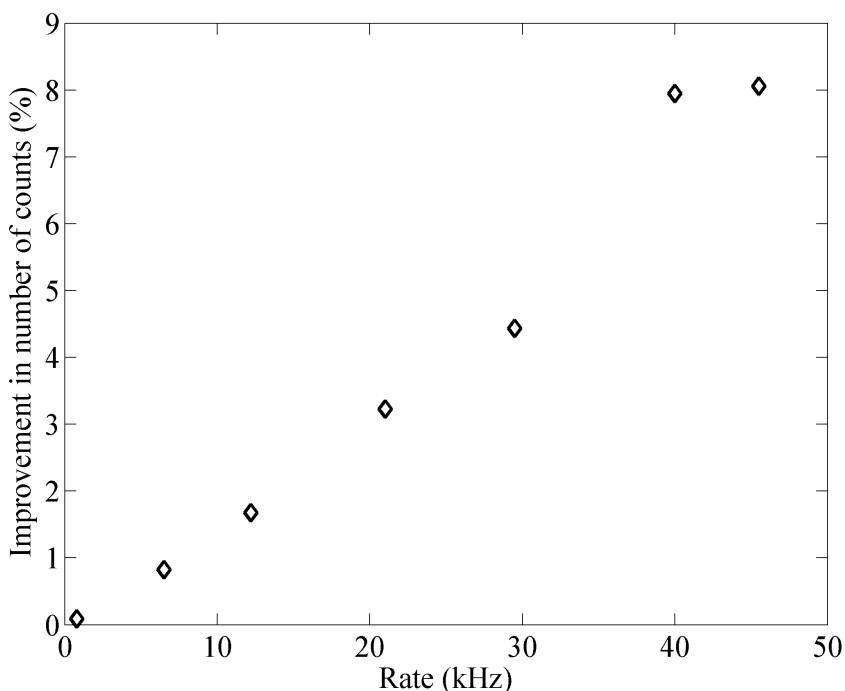


Figure 5.5: Improvement in the number of counts in the 662 keV photopeak of ^{137}Cs as a function the rate.

5.1.4 Time stamps

The probability of a radioactive decay of atoms follows the Poisson statistics [84, 85, 86]. The number N of particles emitted from a radioactive source at an average rate of λ particles per unit time in a fixed interval of time t is then described by the Poisson distribution with mean λt :

$$P(N = r) = \frac{(\lambda t)^r e^{-\lambda t}}{r!}, \quad (5.3)$$

where r is a positive integer, equal to the number of events found in the interval t . The probability to find no events in the time interval t is given by the exponential distribution $e^{-\lambda t}$.

For a Poisson process the numbers of occurrences counted in disjoint intervals are independent from each other. This latter property is known as the independent increments property of the Poisson process. Moreover, the probability distribution of the number of occurrences counted in any time interval only depends on the length of the interval.

The number of arrivals occurring in any bounded interval of time after time t is independent of the number of arrivals occurring before time t . An immediate consequence of these properties is that the waiting time until the next occurrence is exponentially distributed.

To illustrate the exponentially-distributed inter-arrival times property, consider a homogeneous Poisson-process $N(t)$ with rate parameter λ , and let t_k be the time of arrival of the k -th hit, for $k = 1, 2, 3, \dots$. Clearly the number of arrivals before some fixed time t is less than k if and only if the waiting time until the k -th arrival is more than t . In symbols, the event $[N(t) < k]$ occurs, if and only if the event $[t_k > t]$ occurs. In particular, if one considers the waiting time until the first arrival, it is clear that the time is more than t , if and only if the number of arrivals before time t is 0. Combining this latter property with the above probability distribution for the number of homogeneous Poisson-process events in a fixed interval gives:

$$P(t_2 - t_1) = \lambda e^{-\lambda(t_2-t_1)}. \quad (5.4)$$

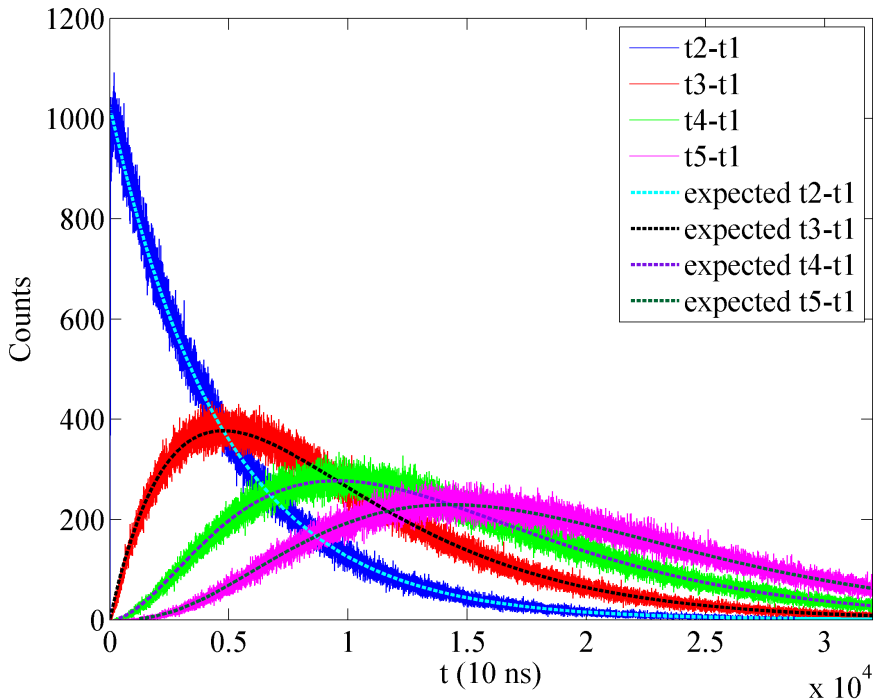


Figure 5.6: Distribution of the difference in the arrival times $t_k - t_{k-1}$, $t_k - t_{k-2}$, $t_k - t_{k-3}$ and $t_k - t_{k-4}$. The dashed lines are the expected distributions for a given average rate λ measured with the detector normalized to the total number of counts, while the continuous lines are the measured distributions of the inter-arrival times.

One can similarly show that the other inter-arrival times $t_k - t_{k-1}$ share the same distribution. Hence, they are independent, identically-distributed random variables with parameter $\lambda > 0$ and expected value $1/\lambda$. Fig. 5.6 shows the distribution of the inter-arrival times $t_k - t_{k-1}$, $t_k - t_{k-2}$, $t_k - t_{k-3}$ and $t_k - t_{k-4}$. The dashed lines are the expected distributions for a given average rate λ measured on the detector normalized to the total number of counts. The distribution of the difference in the arrival times of consecutive pulses $t_k - t_{k-n}$ is given by the expression in Eq. 5.3, with the number of pulses $r = n - 1$ in the time interval $t_k - t_{k-n}$. The continuous lines are the measured distributions of the inter-arrival times. There is a good agreement between

the expected distributions and the measured ones.

5.1.5 Multiple channels pile-up compensation

The DPSA developed in this project has been implemented and tested on the General Purpose Trigger and Readout Board (TRB) which can host up to 4 ADC channels. We have performed a test to verify the functionality of the FPGA-processor combination when the maximum number of channels is used. We used for our tests four detectors: CsI(Na), NaI(Tl), and two CsI detectors irradiated by a ^{60}Co source. Fig. 5.7 and Fig. 5.8 show the measurements that were done for different rates for each detector. For all rates, we have first acquired data with each detector alone and afterwards with all four at the same time, while keeping the same setup for each rate.

The red and brown lines represent the spectra collected by one detector when all detectors are simultaneously collecting data with the pile-up compensation turned OFF and ON, respectively. The green and blue lines represent the spectra collected by one detector alone, with the pile-up compensation turned OFF and ON, respectively. These curves are nicely overlapping as expected. We can, therefore, conclude that there is no difference in using one channel or all 4 channels of the TRB at the same time and that the DPSA algorithms are not influenced by the simultaneous operation.

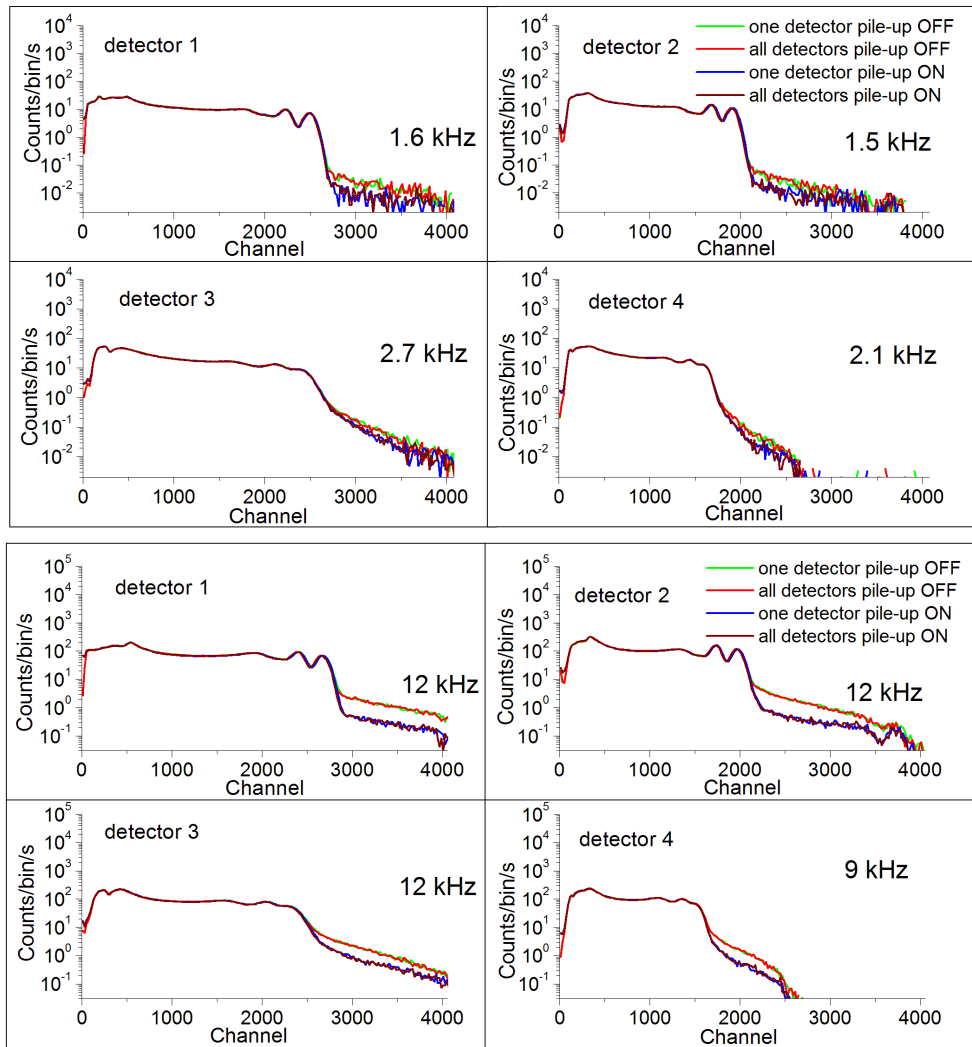


Figure 5.7: The ^{60}Co spectra for detector n ($n=1\text{-}4$) corresponding to (CsI(Na), NaI(Tl), and two CsI detectors) for two sets of acquisition rates. The red and brown lines represent the spectrum collected by one detector when all detectors are simultaneously collecting data with the pile-up compensation turned OFF and ON, respectively. The green and blue lines represent the spectrum collected by one detector alone with the pile-up compensation turned OFF and ON, respectively. The bin size is 20 channels.

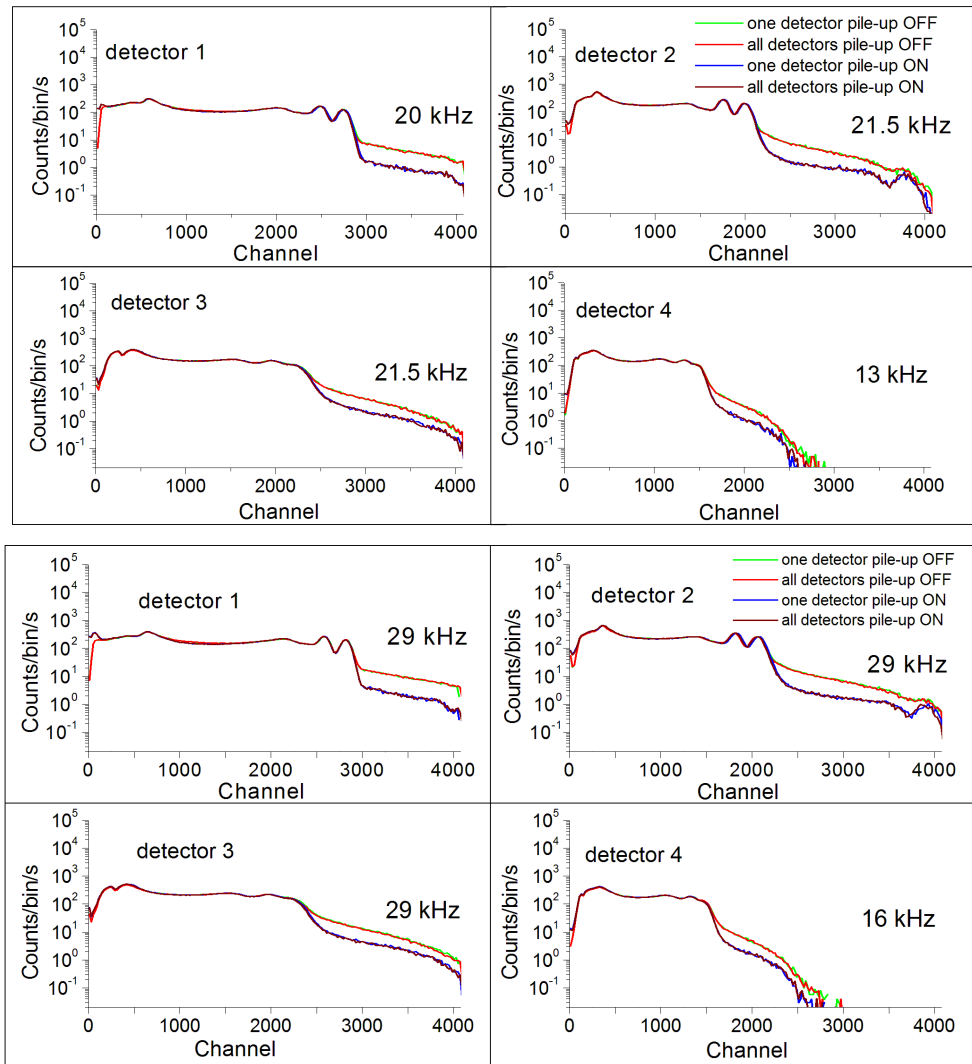


Figure 5.8: Same as Fig. 5.7 for two higher rates.

5.2 In-beam test measurements

To test the DPSA under realistic beam conditions, we have performed an experiment at GSI [2]. For this test our DPSA was implemented on the SIS3302 [13] as described in section 3.7. The beam was ^{64}Ni with an energy of 600 MeV/u impinging on a target

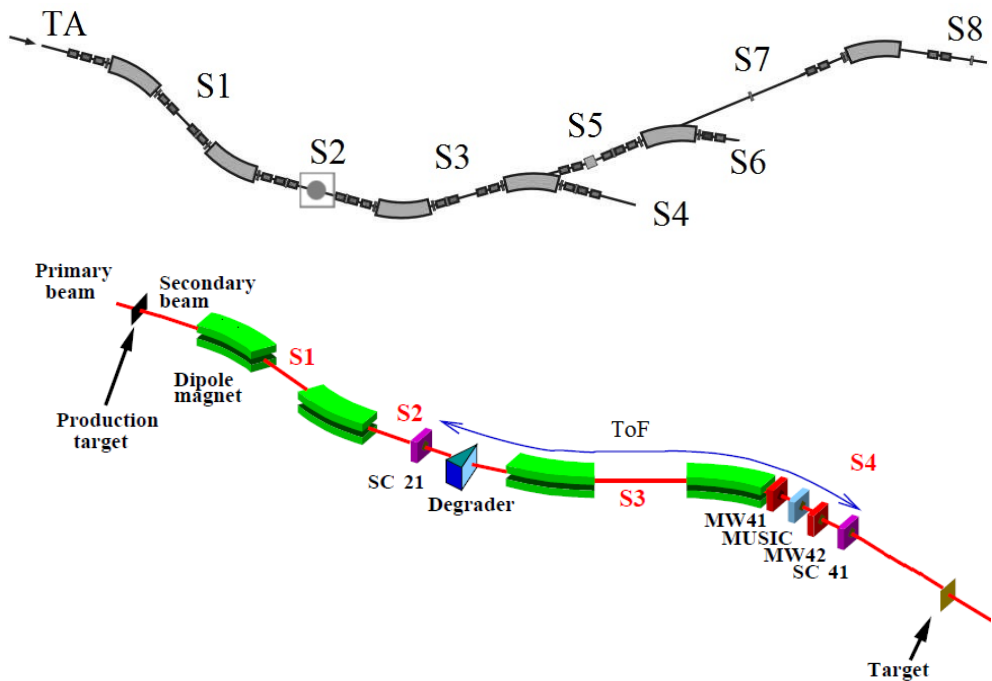


Figure 5.9: Scheme of the FRS. After leaving the SIS Synchrotron, the beam hits one of the production targets, situated at the target area (TA), and is subsequently guided through the beamline by bending magnets to slit positions S1-S8. The bottom picture shows our experimental setup, located at S2 and S4.

of ${}^9\text{Be}$ at the entrance of the FRagment Separator (FRS).

The main elements of the FRS are listed below in the same order as the beam passes through them (see Fig. 5.9). The first element is the *target area*. After leaving the SIS Synchrotron by penetrating the vacuum window, the beam hits one of the production targets, mounted on a ladder that can be remotely moved into the beam line. Passing through the first ion optical section, the beam reaches the first focal plane. At the second focal plane resides the Sc21 Scintillator, the S2 slit, and an energy degrader. Additional components like stripper foils can be mounted on a ladder located behind the degrader. At the end station S4 of the FRS, the final focal plane is used usually for particle identification, but can also host additional detectors for experi-

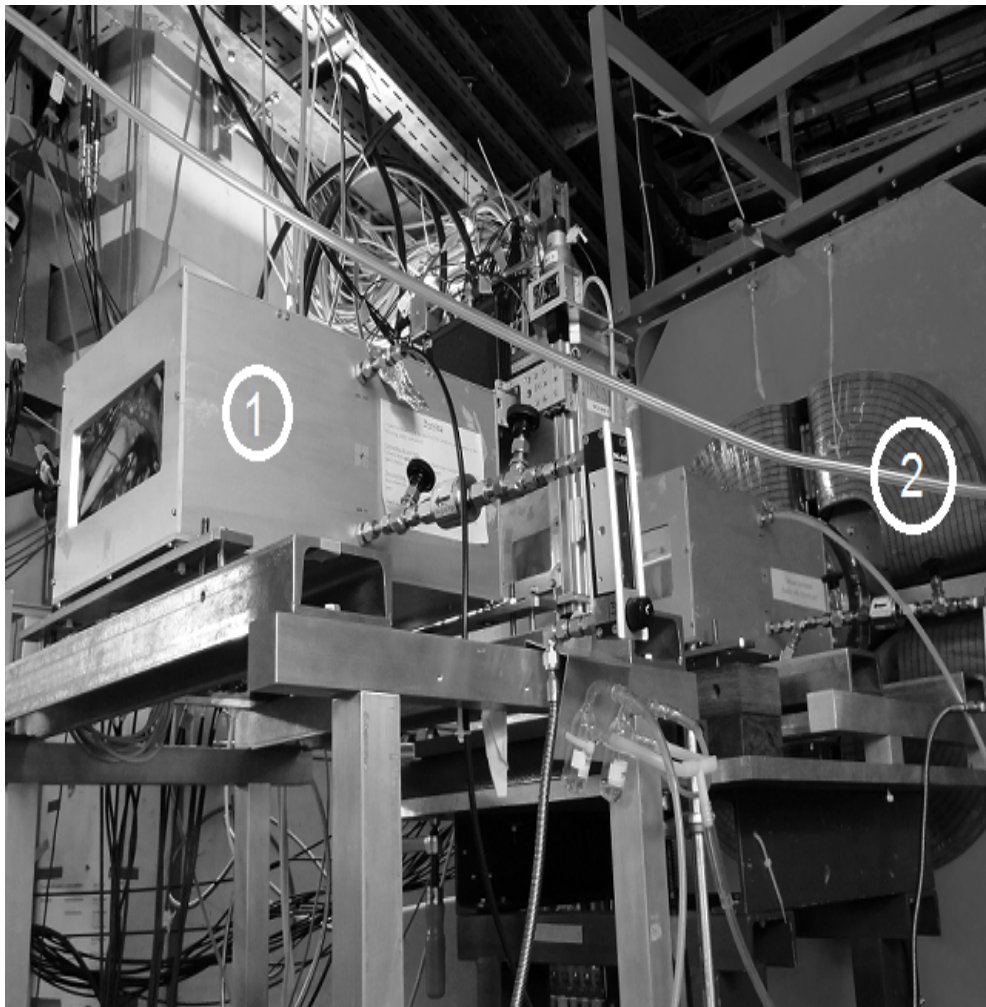


Figure 5.10: Photograph of the MUSIC80 detector at the station S4 of the fragment separator. Indicated on picture are: 1 - MUSIC detector, 2 - quadrupole magnet

ments. The S4 components are mounted in air, which causes no serious disturbance at the relativistic ion energies, however the amount of air and the corresponding energy loss and straggling have to be considered for proper implantation of the ions in a stopper foil.

In this experiment, our focus was the multi-wire ionization chamber (MUSIC)

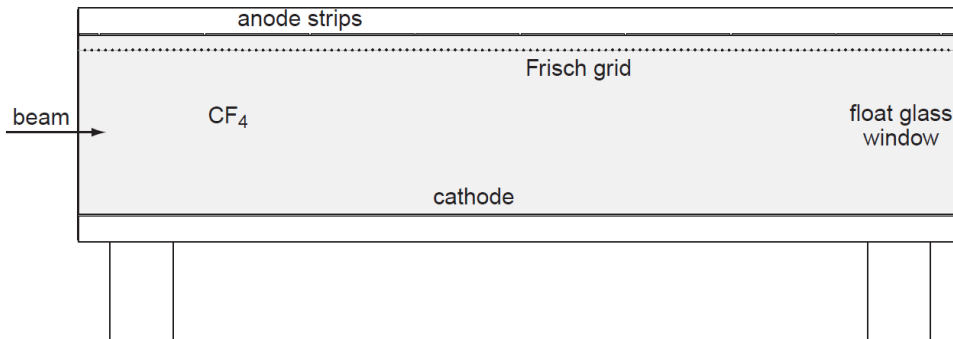


Figure 5.11: Internal scheme of the MUSIC80 ionization chamber. When a relativistic heavy ion traverses the active volume of MUSIC, which contains a counting gas, it creates an ionization track consisting of electrons and positive ions. A strong, uniform, vertical electric field drifts the electron cloud up through a grounded Frisch grid to a positive anode plane.

detector shown in Fig. 5.10, which was read by our FEE employing the SIS3302 with DPSA. The principle behind MUSIC as schematically shown in Fig. 5.11 is as follows: when a relativistic heavy ion traverses the active volume of MUSIC, which contains a counting gas, it creates an ionization track consisting of electrons and positive ions. A strong, uniform, vertical electric field drifts the electron cloud up through a grounded Frisch grid to a positive anode plane. The ionization chamber MUSIC80 is a fast, multiple sampling ionization chamber with 8 anode strips and a vertical drift length of 80 mm. It is operated with pure tetrafluoromethane (CF_4) at room temperature and atmospheric pressure as counting gas. To ensure the correct operation of the chamber, the gas should not contain more than 10 ppm impurities. The homogeneous entrance windows consisting of thin float glass D263 (DESAG), with a thickness of $210 \mu\text{m}$ with integrated field homogenization enable a compact setup. The field homogenization consists of aluminium strips (thickness $1 \mu\text{m}$) deposited on the float glass by photolithography and connected via a voltage divider with resistors glued directly onto the glass plate. The anode strips are read out with an optimized charge-sensitive preamplifier and shaper combination for particle rates up to 200 kHz. Since the number of generated electrons in the counting gas is roughly proportional to the

square of the charge of the penetrating particle, the output voltage of the shaper is a measure for the atomic number of this particle.

Using an additional fast start signal (e.g. a scintillator signal) the drift time of the electron cloud provides information about the vertical position of the passing particle. The stop signal can be derived from the common timing output of the shaper module.

The active area of the MUSIC80 is 200 mm × 80 mm, and the active length is 400 mm. The 8 anode strips are equally distributed, each with an active length of 50 mm. The distance from the anode to the Frisch grid is 7 mm.

Four of the MUSIC80 channels were read using analog readout electronics, whereas the other 4 were read using our digital acquisition system embedded in the Multi Branch System (MBS). An external trigger is used to signal the start of the data acquisition. For the analog acquisition chain, the pre-amplifiers are mounted on top of the MUSIC very close to the anode. The signals are sent to specially built shapers, and then further transmitted to the ADC. The gate of the ADC is generated from the trigger given by the detection of one particle in the Sc41 plastic detector. When the trigger starts the acquisition, a time window of 150 μs is opened for the digital readout. All the signals arriving in this time window are read and analyzed using the DPSA. The information about their amplitudes and time stamps with respect to the trigger are stored for each channel. The acquisition chain enables a continuous read out of the data coming from the MUSIC detector.

5.2.1 Energy calibration

For the energy calibration, detailed simulations were performed using LISE++ [87] to calculate the transmission and yields of fragments produced and collected in the FRS. The code allows to simulate the beam transport for different settings of the FRS and provides access to a number of parameters such as: stopping powers, energy losses, energy-loss straggling, angular straggling.

The calibration runs have been performed using a $^{64}\text{Ni}^{28+}$ beam with an energy of 550 MeV/u. Table 5.3 shows the calculated energy loss inside the MUSIC80 for different settings of the FRS (described as $\alpha - \beta - \gamma$, with α g/cm² for the primary

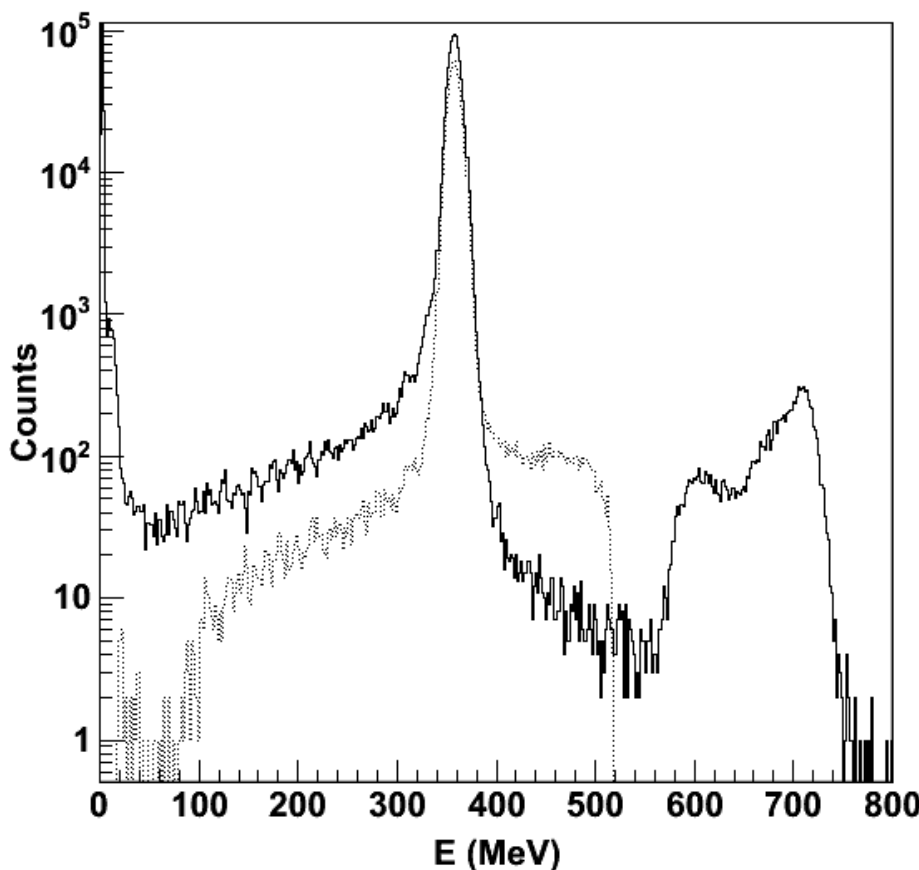


Figure 5.12: Energy loss distribution in the MUSIC80 detector. The solid line represents the energy lost in one of the MUSIC channels read with the digital readout. The dashed line is the energy lost in one of the analog channels.

target area, β g/cm² of the S2-degrader, γ g/cm² of the S4-degrader).

Fig. 5.12 shows the energy loss in the MUSIC detector after calibration, corresponding to a 4-4-2 setting of the FRS. The solid line is the energy lost in one of the channels read with the digital readout (DPSA is active) and the dashed line is the energy lost in one of the channels read by the analog readout. The peak at 357 MeV corresponds to the primary ⁶⁴Ni beam. The reaction products appear on the left hand

Table 5.3: Calculated energy loss dE inside the MUSIC80 detector for different settings of the FRS (labelled as $\alpha - \beta - \gamma$, α g/cm² for the primary target area, β g/cm² of the S2-degrader, γ g/cm² of the S4-degrader).

FRS setting	0-4-0	0-6-0	4-4-2
dE (MeV)	300	323	357

side of the peak. The part of the spectrum situated to the right of the peak is due to pile-up. The spectrum collected by the analog readout is more strongly affected by pile-up than the digital spectrum. The smaller range of the energy is a consequence of the analog readout chain which cuts the spectra at 520 MeV.

5.2.2 Event multiplicity

In general, using the digital readout, more than one pulse is identified in one time window of 150 μs . Fig. 5.13 shows the energy distribution for each of the subsequent hits. The number of counts decreases with the hit number. However, the shape of the spectra remains the same. Fig. 5.14 shows the time stamps of the hits in the sequence from 1 to 6 with respect to the trigger. It is clearly visible that the first hit is detected soon after the trigger signal.

The arrival times are an indication of the rate on the MUSIC80 detector. If the beam is uniform during the measurement, there are several ways to determine the rate. The most simple and accurate way to measure the rate is to find the total number of hits detected in one of the ADC channels during the measurement. If the total number of triggers is n_{trig} and for each trigger the measuring window is $\Delta t = 150 \mu s$, then the average rate is:

$$R = \frac{n_{counts}}{\Delta t n_{trig}}, \quad (5.5)$$

where n_{counts} is the total number of counts detected in one ADC channel for the time of the run. Selecting one channel for a given run, the calculated rate is found to be $R = 267$ kHz.

Alternatively, the rate could be determined by exploiting the exponential distri-

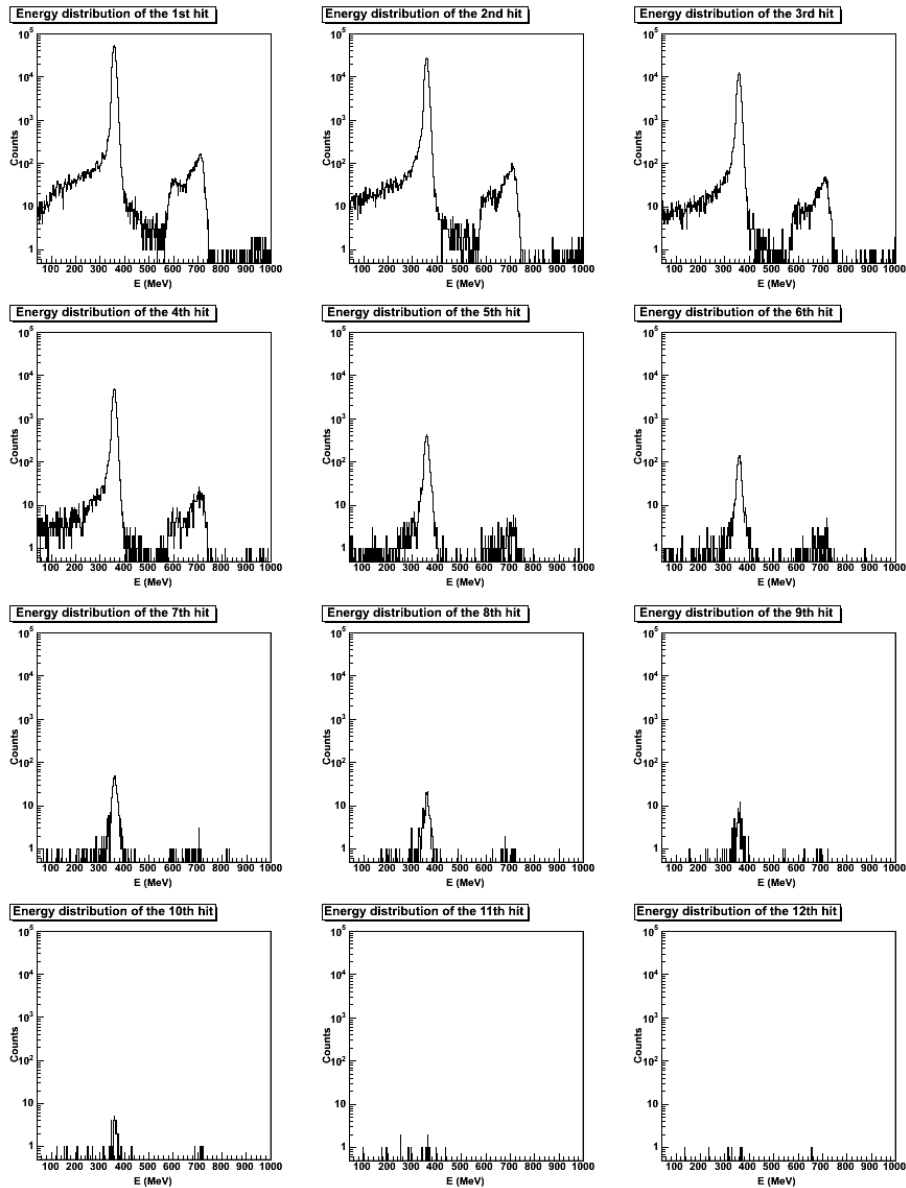


Figure 5.13: Distribution of the energy deposited by ionizing particles inside the MUSIC80 detector for each of the subsequent hits. The number of counts decreases with the hit number, but the shape of the spectra is the same.

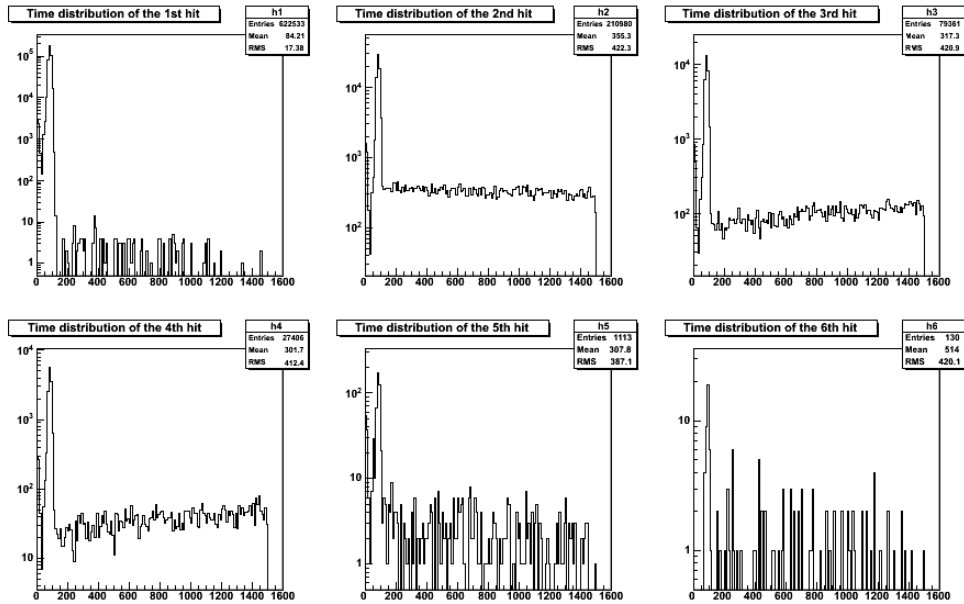


Figure 5.14: Distribution of the arrival times of each hit with respect to the trigger for one acquisition channel. Most of the first hits come immediately after the trigger signal. The setting of the FRS was 4-4-2.

bution of time differences between two consecutive hits. In section 5.1.4, the distribution was described as:

$$P(t_2 - t_1) = Ne^{R(t_2 - t_1)}, \quad (5.6)$$

where N is just a normalizing factor that acts as a parameter in the fit, R is the rate and t_1 and t_2 are the time stamps of the first, and second hit in one event, respectively. In Fig. 5.15, using the same run and ADC channel as for the previous method, the distribution of the time differences between two consecutive hits is plotted and the fitted rate is $R = 263$ kHz.

A third method to evaluate the rate analyzes the number of events with k hits. The probability of finding an event with k hits in the MUSIC80 for a single trigger is

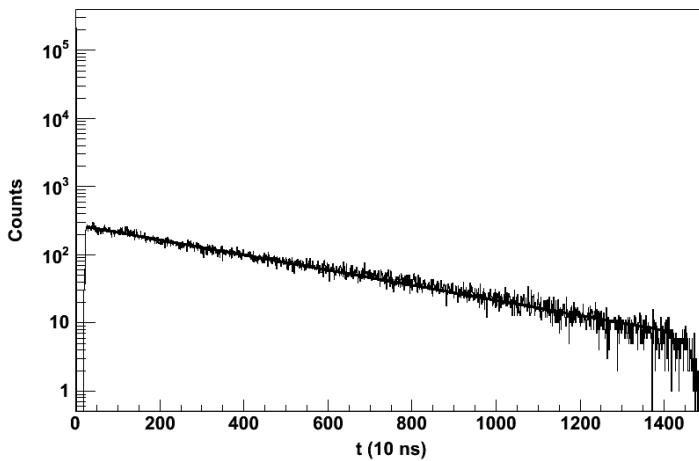


Figure 5.15: Distribution of the difference in arrival times of two consecutive hits for one digital acquisition channel at an incoming rate of 263 kHz as extracted from the fit with an exponential distribution.

given by the Poisson distribution:

$$P(n = k) = \frac{(R \Delta t)^k e^{-R \Delta t}}{k!}, \quad (5.7)$$

where R is the rate and $\Delta t = 150 \mu s$ is the measuring window for each trigger. Fig. 5.16 shows the distribution of the number of hits and the Poisson fit to the data. Due to the measurement starting after the trigger signaling a particle at the Sc41 plastic detector, there are no events with zero hits, so the fit starts from $k = 1$. Using the same run and ADC channel number as in the previous two methods, the fitted rate of the incoming beam is 260 kHz.

Table 5.4 lists the calculated rates obtained with all three methods for each channel. The rate calculated from the number of counts has the smaller uncertainties, whereas the rate calculated from the time difference between two consecutive hist has the largest uncertainty. Using the three different methods, the result agrees quite well with each other within a 2σ error.

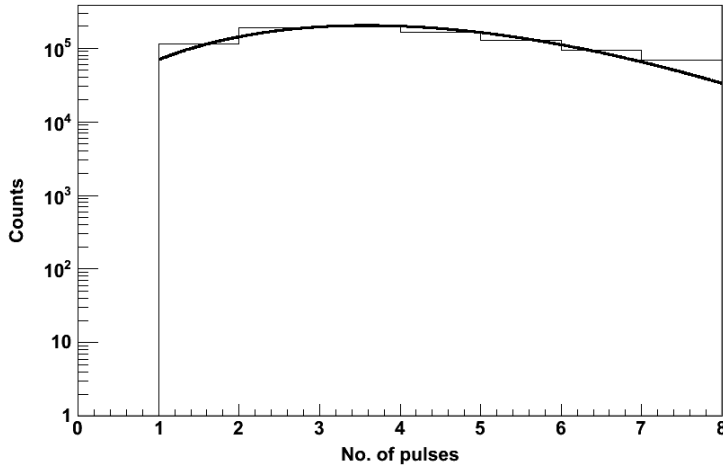


Figure 5.16: Distribution of the number of hits per event and Poisson fit to the data. The evaluated rate on the MUSIC80 detector is 260 kHz.

5.2.3 Energy resolution and pile-up to peak ratio

We proceed in the data analysis with the calculation of the energy resolution and the number of counts in the peak, for both the analog and the digital data. In order to compare the pile-up rate of the analog data with the digital one, we limit ourselves to the part of the spectra below 520 MeV deposited energy, which is the upper limit of the analog spectra, see Fig. 5.12. We estimate the fraction of pile-up to be the ratio between the number of counts from the end of the peak up to 520 MeV and the number of counts in the peak. We define the end of the peak as the energy corresponding to the point situated 3 standard deviations to the right of the centroid. Table 5.5 shows the fraction of pile-up for the analog (P_{an}) and digital (P_{dig}) data. ΔP represents the difference between P_{an} and P_{dig} . The last column, I_{counts} , represents the total number of counts in the MUSIC measured with the analog electronics subtracted from the total number of counts measured with the digital electronics, and the result divided by the number of counts in the analog spectrum. It can be clearly seen that this improvement is dependent on the rate. At the highest rate (265.4 kHz) the pile-up drops from 5.81% for the analog data to 1.31% for the digital one. Moreover, at this

Table 5.4: Calculated rates for each of the four detector channels and for four runs, evaluated by three different methods. Each of the four runs has been measured for different beam intensities.

Run	Method	Rate ch. #1 (kHz)	Rate ch. #2 (kHz)	Rate ch. #3 (kHz)	Rate ch. #4 (kHz)
run 1	counts	265 (2)	262 (2)	267 (2)	267 (2)
	poisson	265 (5)	264 (5)	260 (4)	256 (4)
	$t_2 - t_1$	255 (6)	258 (6)	263 (6)	269 (6)
run 2	counts	270 (2)	266 (2)	273 (2)	272 (2)
	poisson	267 (4)	267 (4)	263 (4)	259 (4)
	$t_2 - t_1$	258 (6)	257 (6)	263 (6)	270 (6)
run 3	counts	116 (1)	117 (1)	114 (1)	114 (1)
	poisson	108 (2)	112 (2)	106 (2)	109 (2)
	$t_2 - t_1$	120 (3)	117 (3)	121 (3)	119 (3)
run 4	counts	139 (1)	139 (1)	137 (1)	138 (1)
	poisson	140 (2)	142 (2)	142 (3)	143 (2)
	$t_2 - t_1$	135 (3)	134 (3)	135 (3)	142 (3)

Table 5.5: The dependence of the pile-up and the number of counts from the digital and analog data with the rate of particles on the MUSIC80 detector. The rates in this table are the mean values of the rates in Table 5.4. P_{an} is the pile-up for the analog and (P_{dig}) is the pile-up for the digital data. ΔP represents the difference between P_{an} and P_{dig} . The last column, I_{counts} , represents the total number of counts with the analog electronics subtracted from the total number of counts with the digital electronics, and the result divided by the number of counts in the analog spectrum.

Run	Rate kHz	P_{an} (%)	P_{dig} (%)	ΔP (%)	I_{counts} (%)
run 1	112	0.73	0.36	0.37	12.6
run 2	139	1.86	0.53	1.33	55.1
run 3	263	5.67	1.23	4.44	191.1
run 4	265	5.81	1.31	4.50	195.0

high rate one measures 195% more counts in the case of the digital data. The great improvement in the number of counts as well as the reduction of pile-up advocate strongly for the use of a digital readout acquisition chain.

6

Summary and conclusions

The aim of the project reported in this thesis was to develop Digital Pulse-Shape Analysis (DPSA) algorithms and control systems for the Nuclear STructure Astrophysics and Reactions (NuSTAR) experiments at the upcoming Facility for Antiproton and Ion Research (FAIR). Some of these experiments will encompass a tremendous number of electronics channels ($> 10^6$), requiring smart online solutions for data processing.

After an introduction to the physics of NuSTAR and the challenges for front-end electronics arising from the diversity of requirements for the three experimental branches, we described the DPSA algorithms, their implementation and testing with the help of simulations in chapter 3. It is necessary to develop tools as general as possible and to allow for a future extension of those tools. By tools we refer to the DPSA algorithms that we have implemented, to the design of the control methods, and to the design and construction of the hardware that we have used. More specifically, for the hardware design a prototype board was developed at KVI, during this project. The board consists of a Quad ADC board built on top of the previously developed Trigger and Response Board (TRB), as was presented in chapter 3.

The DPSA algorithms are independent modules dealing with digitized data in a real-time environment. A baseline follower, $k\sigma$ triggering, moving-window deconvolution, moving average filter, box-trigger and pile-up compensation were implemented on two types of front-end electronics using powerful Field-Programmable Gate Arrays (FPGA). In brief, we present the DPSA starting from the raw signal, as it is read from the ADC. This signal is analyzed and filtered with the baseline follower. The information of the baseline values and the filtered signal are used to calculate dynamically-adjusted thresholds. Whenever the filtered signal exceeds the value of the threshold, the baseline follower enters a sleeping mode. This way, the baseline is immune to pulling due to the occurrence of a pulse. The threshold calculated in terms of the standard deviation of the noise level is also used as input for the box-trigger, which returns the time stamp of each pulse. The baseline-corrected signal is then filtered with the Moving Window Deconvolution (MWD) and the Moving Average Filters (MAF) in order to recover the amplitudes of each pulse. The time stamps and obtained amplitudes are passed to the pile-up compensation block and the corrected amplitudes are recovered. As pointed out throughout this thesis, the pile-up compensation algorithm does not identify and reject the pile-up events as common methods do, but it identifies and corrects the affected amplitudes and thus enables to also use the events affected by pile-up in the analysis. The modular nature of the algorithms allows flexibility in the data processing depending on the particularities of the input signal. Moreover, the FPGA characteristic of being fully parallel permits operations on data to run simultaneously without having to share the same resources.

Controls is a key aspect in the development of any experiment. We have shown that, due to the stringent and broad requirements of the experiments currently being set up by the NuSTAR collaboration, not only controls are needed, but flexible and distributed controls are required. The interactions between various subsystems, that may be situated at different locations, and the need of processing data in real time, in order to extract the required information, makes controls highly necessary. First, we define the basic concepts of controls, such as open and closed loops. We describe the functionality and structure of a control system and motivate the choice of Experi-

tal Physics and Industrial Control System (EPICS) for our implementation. Secondly, the realization of a self-adjusting control loop embedded in Front-End Electronics (FEE) provides a good example of the limitations of the system. We implement a self-adjusting control loop based on the constant monitoring of the constructed spectrum. If the value of the relative energy resolution of the preselected peak is outside the preset values, the system readjusts the voltage to the optimum value. The functionality of the control loop is tested in an online environment and test results show that the performance of the system is satisfactory. The arising limitations lie in the used hardware, i.e. the processor associated with the FPGA, but not within EPICS. In most of the FAIR experiments, EPICS will be used as a control system together with the Multi Branch System (MBS) DAQ currently in use at Gesellschaft für Schwerionenforschung GmbH (GSI). This enables our access to a set of unique tools to develop applications and to build our controls concept.

The last chapter is dedicated to the tests of the complete DPSA with focus on the pile-up compensation, the operation of which was tested in two types of experiments, with radioactive sources and in-beam. The beam tests were performed at GSI and the results from those tests are analyzed in this thesis. The outcome of these tests shows a clear improvement of the pile-up to peak ratio, especially at large rates, where the data are most affected by the pile-up distortion. It is shown that the digital electronics performs well in beam conditions and that our solution is not only viable, but also offers improved results compared to the existent setups.

It is clear from the requirements that the new FAIR experiments demand a new and robust method for controls and DAQ. We have motivated this by pointing out in this thesis the multitude of requirements (e.g. large number of channels, high rates) that come from the experiments planned for FAIR. We have presented our approach for controls and we have developed such controls during the PhD research presented in this thesis. Furthermore, we have developed hardware solutions suitable for the implementation of our DPSA that put into practice our controls approach. All these R&D results were tested in realistic experiments and their results are discussed in detail in this thesis. With the results presented in this thesis we have shown, that

our approach on controls and DPSA algorithms is a viable solution for the upcoming NuSTAR experiments and that it opens the way for a robust, modular and scalable data acquisition including data processing for NuSTAR.

The framework for the self-adjusting control loop approach has been created and proven functional in this thesis. It has been developed in such a way that it will allow the expansion of the number of controlled parameters in the future.

Both the DPSA algorithms and the EPICS device support, discussed in chapters 3 and 4, respectively, can be developed separately. However, the combination of both becomes a powerful tool for data acquisition and online monitoring simultaneously. Parameters from the (new) DPSA can be used for control actions, in the same way the relative energy resolution was used in the self-adjusted control loop for the HV unit as implemented in EPICS.

In the near future, the requirements from the upcoming experiments at FAIR will become clearer and new specialized electronics will be made available. This implies that new DPSA algorithms can be developed for specific applications, but also that new devices (such as temperature control system) and new embedded electronics (such as the FEBEX [88] board which is the new Front-End Board developed at GSI) should be included in EPICS for the users and ultimately for the scientific community at large.

A

Abbreviations used in this thesis

AGATA	Advanced GAMma Tracking Array
AIDA	Advanced Implantation Detector Array
CAMAC	Computer Automated Measurement And Control
CBM	Compressed Baryonic Matter Experiment
DAQ	Data AcQuisition
DESPEC	DEcay SPECtroscopy
DPSA	Digital Pulse-Shape Analysis
ELISe	ELection-Ion Scattering experiment in a storage ring (eA collider)
EPICS	Experimental Physics and Industrial Control System
EXL	EXotic nuclei studied in Light-ion induced reactions
FAIR	Facility for Antiproton and Ion Research
FEBEX	Front-End Board with optical link EXtension
FEE	Front-End Electronics
FPGA	Field-Programmable Gate Array
FRS	FRagment Separator
GSI	Gesellschaft für Schwerionenforschung GmbH

HISPEC	HIgh-resolution in-flight SPECtroscopy
HESR	High-Energy Storage Ring
HPGe	High-Purity Germanium
KVI	Kernfysich Versneller Instituut
MAF	Moving-Average Filter
MBS	Multi-Branch System
MWD	Moving-Window Deconvolution
NESR	New Experimental Storage Ring
NIM	Nuclear Instrumentation Module
NuSTAR	Nuclear STructure Astrophysics and Reactions
PANDA	anti-Proton ANihilation at DArmstadt
PMT	PhotoMultiplier Tube
R ³ B	Reactions with Relativistic Radioactive Beams
Super FRS	Super FRagment Separator
TRB	Trigger and Response Board
VME	Versa Module Europa

Nederlandse Samenvatting

Voor het einde van dit decennium zal de nieuwe Facility for Antiproton and Ion Research (FAIR) een van de grootste natuurkundefaciliteiten in de wereld worden. FAIR zal bundels leveren van antiprotonen en radioactieve ionen met een ongeëvenaarde intensiteit, hogere bundelkwaliteit en -energie en het wordt mogelijk om verschillende experimenten parallel uit te voeren. Kernfysica- en astrofysica-onderzoek zal georganiseerd worden binnen de Nuclear STructure, Astrophysics and Reactions (NuSTAR) collaboratie.

De diversiteit in het onderzoek dat NuSTAR zal doen, vraagt om de ontwikkeling en bouw van speciale detectoren (bv. R³B, HISPEC/DESPEC, EXL) die op hun beurt weer een breed scala aan eisen stellen aan data-acquisitie en controls (besturing van de apparatuur). In dit proefschrift presenteren we de ontwikkeling van Digital Pulse Shape Analysis (DPSA , analyse op basis van pulsvorm), ingebouwd in Front-End Electronics (FEE, elektronica bij de detector) en de benodigde 'slow control' voor dergelijke systemen. Functies die het slow controls systeem zoal voor zijn rekening neemt zijn initialisatie, statusraportage, calibratie, optimalisatie en run-time controls (instellingen tijdens de meting) zoals het updaten van controlparameters en het mon-

itoren van systeem- en omgevingsparameters.

Het grote aantal electronische kanalen met elk zeer verschillende vereisten zal één van de uitdagen vormen voor de Data-Acquisitie (DAQ). De hoge telsnelheden en het grote aantal kanalen leidt tot een ongeëvenaarde hoeveelheid informatie. Daarom is het nodig om de data online te verwerken om de gewenste informatie uit de metingen te halen. In dit proefschrift behandelen we de DPSA algoritmes die zijn geïmplementeerd in de FEE en die gedurende het project zowel offline als in de bundel zijn getest.

De DPSA algoritmes zijn onafhankelijke modules die gedigitaliseerde data verwerken in een realtime-omgeving. Een baseline follower, $k\sigma$ -triggering, moving-window deconvolution (MWD), moving average filter, box-trigger en pile-up compensatie (compensatie voor overlap van pulsen) zijn geïmplementeerd in twee verschillende FEE's met behulp van krachtige Field-Programmable Gate Arrays (FPGA). Hier volgt een korte beschrijving van de DPSA, beginnend bij het oorspronkelijke signaal zoals die wordt uitgelezen uit de Analog to Digital Converter (ADC). Dit signaal wordt geanalyseerd en gefilterd door de baseline follower. De baseline-waarden en het gefilterde signaal worden gebruikt om de dynamisch geregelde thresholds (drempelwaarde) te berekenen. De baseline follower gaat in een slaapstand zodra het gefilterde signaal boven de threshold uitkomt. Op deze manier wordt de baselinemetting niet beïnvloed door de puls zelf. De threshold, die berekend is in termen van de standaarddeviatie van de ruis, wordt ook gebruikt als input voor de box-trigger, die een time stamp (tijdmeting) geeft aan elke puls. De time stamps en amplitudes gaan naar het pile-up compensatieblok en de gecorrigeerde amplitudes worden uitgerekend. Het pile-up compensatie-algoritme verwijdert de pile-up pulsen niet, zoals dat bij veel methoden wel gebeurt, maar identificeert en corrigeert de aangetaste amplitudes zodat ook deze pulsen bruikbaar worden in de analyse.

Flexibele en gedistribueerde aansturing (controls) zijn vereist en met dit proefschrift introduceren we onze aanpak van controls. We maken gebruik van open en closed loop (teruggekoppelde) controls bij het bouwen van een zelfcorrigerende control loop ingebouwd in de FEE. We hebben de zelfcorrigerende control loop geïm-

plementeerd, gebaseerd op het constant monitoren van het geconstrueerde spectrum. Als de relatieve energieresolutie van de voorgeselecteerde piek buiten de vooraf ingestelde waarden valt, reguleert het systeem het voltage naar de optimale waarde. Deze opstelling laat zien dat control loops bewerkstelligd kunnen worden en functioneren volgens het ontwerp.

Een substantieel deel van dit proefschrift is gewijd aan testen van de DPSA met radioactieve bronnen en deeltjesbundels. De uitkomst van deze testen laat een duidelijke verbetering zien van de ratio tussen pile-up en piek, met name bij hoge telsnelheden wanneer de data het meest beïnvloed wordt door pile-up vervorming.

Met de resultaten in dit proefschrift hebben we aangetoond dat onze aanpak van controls en DSPA algoritmes een haalbare oplossing is voor de aankomende NuSTAR-experimenten en de mogelijkheid biedt voor een robuuste, modulaire en schaalbare data-acquisitie voor NuSTAR.

Acknowledgments

There are very few people that can look back at a four year project and say they have no regrets. Of course, things can always be done differently, which might be either better or worse. However, I am one of the lucky few: I am ending successful a journey that I started four years ago, and the "discoveries" of that journey are presented in this book. Before I embark on a new challenging journey that promises to deliver a lot of treasures for soul and mind, I think this is the time and the place to thank those that were, in many different ways, part of this amazing voyage that concludes here.

I wish to thank my promotor Prof. N. Kalantar-Nayestanaki for the time spent reading my thesis and the valuable advices I received from him during the project. I hope you will keep the enthusiasm for research that you share with your students. I also enjoyed our trips together to various places, they were a lot of fun!

Here I want to thank my first supervisor Dr. H.J. Wörtche. Dear Heinrich, it is not exaggerated when I say that this project wouldn't have been completed without you. Apart from the scientific relation that we had, which enabled me to always solve the puzzles that appeared during my thesis, you have always been next to me when I needed it most. It is hard to mention everything in just a few words, but I

will never forget your encouraging words and kindness... For all this, I thank you from the bottom of my heart! I can't end this paragraph without thanking here your wife Gudula and daughters: Fredi, Antonia and Helene for all the nice moments and dinners we all shared.

I want to express my thanks to my second supervisor Dr. C. Rigollet. Thank you for all your help and for all the discussions we had. You were especially nice and helpful when it was more frustrating for me and for that I am grateful. I had a lot of fun also during our trips, even to the very cold Russia. Oh, I almost forgot...cheese rules! (I promised to mention cheese in my thesis).

I would like to thank Profs. T. Aumann, H. Löhner, T. Nilsson for accepting to be part of my reading committee.

During my work, I was lucky to have Peter Schakel involved in this project. Dear Peter, your help during the last four years can't be measured. I am deeply grateful for all the effort you have put into this project. Whenever something was not working, you were there, and after that things worked again... It is not by chance, but by hard work and amazing engineering skills. I will also remember with great pleasure all the trips we made to GSI, and they wore quite a few of them. I thank you for all of this!

I would like to thank Dr. H. Simon for his contribution to this work and for always being supportive with my work. I would also want to thank Dr. N. Kurz for always making the time for Peter and me during our visits and also contributing significantly to this project. I also wish to thank Dr. S. Pietri for his great help during the experiment at GSI and, most important for me, after the experiment, in the data analysis.

I would like to thank Prof. H. Löhner for the time spent reading my thesis and his valuable comments, that improved the value of my thesis. I truly enjoyed our discussion!

I would like to also thank the "old" SAM group members Pim Lubberdink and Julia Jungmann for sharing a lot of fun during our projects. I still think the poster we made (one of them) was the best one...

I want to thank Dr. Janis Endres and Duurt Johan van der Hoek for being my

paranymphs. With Janis I had the pleasure of being part of the experiments he ran at the BBS. I was always delighted by the determination, skills and pleasure he had in spending nearly all the hours of a day in making the impossible, possible. Those times were a lot of fun... and they are probably the thing I will miss most... good physics, enthusiast people and a great friend! Dear Duurt, I thank you for all the fun and awesome moments we had, but also for your encouraging words whenever I needed, you are a great friend...looking forward to more nice memories!

Additionally, I want to thank Duurt Johan van der Hoek and Peter Schakel for translating my summary into Dutch.

I would like to thank Prof. K. Jungmann for his help and for always being supportive.

I would also want to express my thanks to everyone at INCAS³ for welcoming me there and creating a wonderful working environment.

I promised myself when I started to write this that I will not name all my colleagues and friends here since eventually I will forget someone (most of you already know this). I am happy to have so many friends and you guys made me enjoy life at it's maximum. Since only some of you will be able to attend my defense (this world is big, isn't it?), I wish to thank you all for the amazing great fun we had and I am looking forward to even more!

The last paragraph is usually for those who are closest to you...your family. Things would not be complete if I would not remember here the ones that have inspired me most and have given my childhood an aura of perfection: my grandparents, which are no longer among us. I was always encouraged by my parents to do whatever made me happy in life, and I have received from them the education that enables me to do so. For your unconditioned love and care, I thank you! There is no better way of ending this than to thank my dear wife. You have been next to me in my darkest hours and also in my happiest moments, there are no words to express my feelings... I guess I just have to invent one word for it...

References

- [1] FAIR: http://www.gsi.de/portrait/fair_e.html; H. H. Gutbrod, I. Augustin, H. Eickhoff, K. D. Gross, W. F. Henning, D. Krämer, and G. Walter, editors. FAIR Baseline Technical Report. GSI, 2006.
- [2] GSI Helmholtzzentrum für Schwerionenforschung: <http://www.gsi.de>.
- [3] NUSTAR: http://www.gsi.de/forschung/fair_experiments/NUSTAR/index_e.html.
- [4] The SuperFRS Facility: http://www.gsi.de/forschung/fair_experiments/superfrs/index_e.html.
- [5] Reactions with Relativistic Radioactive Beams: http://www.gsi.de/forschung/fair_experiments/NUSTAR/R3b_e.html.
- [6] DEcay SPECtroscopy (DESPEC) and HIgh-resolution in-flight SPECtroscopy (HISPEC): http://www.gsi.de/forschung/fair_experiments/NUSTAR/hispec_e.html.
- [7] NESR, The New Experimental Storage Ring: http://www.gsi.de/forschung/fair_experiments/sparc/nesr.html.
- [8] EXL, EXotic Nuclei Studied in Light-Ion Induced Reactions: <http://www.rug.nl/kvi/research/hnp/research/exl/index>.

- [9] TRB: <https://www.gsi.de/documents/DOC-2007-Mar-60.html>.
- [10] Xilinx Virtex 4 LX40 FPGA: <http://www.xilinx.com/publications/archives/xcell/Xcell52.pdf>.
- [11] Experimental Physics and Industrial Control System: <http://www.aps.anl.gov/epics/>.
- [12] VME, IEEE standard: <http://standards.ieee.org/findstds/standard/1014-1987.html>.
- [13] SIS3302 8 Channel 100 MS/s 16-bit ADC: <http://www.struck.de/sis3302.htm>.
- [14] STRUCK: <http://www.struck.de/>.
- [15] FAIR Conceptual Design Report: http://www.fair-center.com/fileadmin/fair/publications_FAIR/FAIR_CDR.pdf.
- [16] R³B Letter of intent: <http://www-land.gsi.de/R3B/docu/LoI-R3B-final.pdf>.
- [17] UNILAC, Linear accelerator: http://www.gsi.de/portrait/beschleunigeranlage_e.html.
- [18] SIS, heavy ion synchrotron: http://www.gsi.de/beschleuniger/sis18/sis_e.html.
- [19] PANDA, anti-Proton ANnihilation at DArmstadt: <http://www-panda.gsi.de/>.
- [20] CBM: http://www.gsi.de/forschung/fair_experiments/CBM/index_e.html.
- [21] APPA: <http://www.fair-center.de/APPA-Physics.187.0.html>.
- [22] NuSTAR Letter of intent: <http://www.ft.uam.es/Nuclear/Archis/NUSTAR-LoI.pdf>.
- [23] E. Farnea, F. Recchia, D. Bazzacco, Th. Kröll, Zs. Podolyák, B. Quintana, and A. Gadea. Conceptual design and Monte Carlo simulations of the AGATA array. *Nucl. Instr. Meth. Phys. Res. A*, 621(1-3):331 – 343, 2010.
- [24] H.J. Wollersheim *et al.*, Rare ISotopes INvestigation at GSI (RISING) using gamma-ray spectroscopy at relativistic energies, *Nucl. Instr. Meth. Phys. Res. A*, 537(3):637 – 657, 2005.
- [25] AIDA, Technical specifications: http://www2.ph.ed.ac.uk/td/AIDA/Design/AIDA_Draft_Technical_Specification_v1.pdf.
- [26] W.R. Leo, Techniques for Nuclear and Particle Physics Experiments, A How-to Approach. Second Revised Edition, Springer-Verlag, 1994.

- [27] G.F. Knoll, Radiation Detection and Measurement, John Wiley and Sons, 1979.
- [28] C.M. Davisson, Interaction of gamma-radiation with matter. Alpha, beta and gamma spectroscopy, North-Holland, 1965.
- [29] O. Klein and T. Nishina, Über die Streuung von Strahlung durch freie Elektronen nach der neuen relativistischen Quantendynamik von Dirac, *Zeitschrift für Physik A Hadrons and Nuclei*, 52:853–868, Oct. 1928.
- [30] H. Bethe, Zur Theorie des Durchgangs schneller Korpuskularstrahlen durch Materie, *Annalen der Physik*, 397(3):325–400, 1930.
- [31] F. Bloch, Zur Bremsung rasch bewegter Teilchen beim Durchgang durch Materie, *Annalen der Physik*, 408(3):285–320, 1933.
- [32] F. Bloch, Bremsvermögen von Atomen mit mehreren Elektronen, *Zeitschrift für Physik A Hadrons and Nuclei*, 81:363–376, 1933.
- [33] L. Papadopolus, Rise time of scintillation emission in organic and inorganic scintillators, *Nucl. Instr. Meth. Phys. Res. A*, 401:322 – 328, 1997.
- [34] P.B. Littlewood, K.D. Ianakiev, B.S. Alexandrov, and M.C. Browne, Temperature behavior of NaI (Tl) scintillation detectors, *Nucl. Instr. Meth. Phys. Res. A*, 607:432 – 438, 2009.
- [35] S.E. Derenzo, D.K. Wehe, J.D. Valentine, W.W. Moses, and G.F. Knoll, Temperature Dependence of CsI(Tl) Gamma-ray Excited Scintillation Characteristics, *Nucl. Instr. Meth. Phys. Res. A*, 325:147 – 157, 1993.
- [36] J. Birks, The Theory and Practice of Scintillation Counting. Macmillan, 1964.
- [37] Photomultiplier tubes. Basics and applications. Technical report, Hamamatsu: <http://jp.hamamatsu.com>.
- [38] J.C. Barton, Basic physics and statistics of photomultipliers, Technical report, EMI Electron Tubes Note R/P063, 1977.
- [39] Yifei Zhang, Bobing Wu, Yanguo Li, Yongwei Dong, Yongjie Zhang, Wen Xing, Junying Chai, Shixiu Kang, Liming Song, and Shuangnan Zhang, Interior temperature monitoring of NaI(Tl) crystal in space environment by pulse width measurement, *Nucl. Instr. Meth. Phys. Res. A*, 615:272–276, 2010.

- [40] OCTAVE: <http://www.gnu.org/software/octave/index.html>.
- [41] P. Schakel, QuadADC: <http://kvip81.kvi.nl/twiki/bin/view/Sandbox/TRBquadADC-manual>.
- [42] P. Salabura *et al.*, HADES - a high acceptance di-electron spectrometer, *Nucl. Phys. B*, 44:701 – 707, 1995.
- [43] J. Jungmann, Master thesis, A watchdog and radionuclide identification detection system for gamma-ray emitters in aquatic environments, Groningen 2008.
- [44] A. Georgiev, W. Gast, and R.M. Lieder. An analog-to-digital conversion based on a moving window deconvolution, *IEEE Trans. Nucl. Sci.*, 41:1116 – 1124, Aug 1994.
- [45] R. Kalman, A New Approach to Linear Filtering and Prediction Problems, *Trans. ASME J. Basic. Eng.*, 82(Series D):35–45, 1960.
- [46] M. Kavatsyuk, D. Bremer, V. Dormenev, P. Drexler, T. Eissner, W. Erni, E. Guliyev, T. Hennino, B. Krusche, B. Lewandowski, H. Löhner, M. Moritz, R.W. Novotny, K. Peters, J. Pouthas, P. Rosier, M. Steinacher, G. Tambave, A. Wilms, Performance of the prototype of the electromagnetic calorimeter for PANDA, *Nucl. Instr. Meth. Phys. Res. A*, 2011.
- [47] R. Novak, and M. Vencelj, Gauss-Seidel, Iterative Method as a Real-Time Pile-Up Solver of Scintillation Pulses, *IEEE Trans. Nucl. Sci.*, 56:3680 – 3687, Dec 2009.
- [48] M. Vencelj, K. Bucar, R. Novak, and H.J. Wörtche, Event by event pile-up compensation in digital timestamped calorimetry, *Nucl. Instr. Meth. Phys. Res. A*, 607(3):581 – 586, 2009.
- [49] P. Schakel, private communication, KVI Groningen, 2010.
- [50] <http://wiki.kvi.nl/twiki/bin/login/signalsandmore/>.
- [51] B. Bond, K. Hammil, L. Litchev, and S. Singh, FPGA Circuit Synthesis of Accelerator Data-Parallel Programs: <http://research.microsoft.com/apps/pubs/default.aspx?id=120999>.
- [52] CAMAC, Electronics standards and definitions, <http://standards.ieee.org/findstds/standard/583-1982.html>.

- [53] FASTBUS, IEEE standard, http://ieeexplore.ieee.org/xpls/abs_all.jsp?isnumber=894&arnumber=22449&tag=1.
- [54] N. Kalantar-Nayestanaki, H. Moeini, M. Mahjour-Shafiei, F. Aksouh, K. Beckert, P. Beller, K. Boretzky, A. Chatillon, A. Corsi, P. Egelhof, H. Emling, G. Ickert, S. Ilieva, C. Kozuharov, T. Le Bleis, X.C. Le Xuang, Y. Litvinov, K. Mahata, J. P. Meier, F. Nolden, U. Popp, H. Simon, M. Steck, T. Stöhlker, H. Weick, A. Zalite, O. Kiselev, D. Werthmüller, S. Paschalidis. First feasibility study for EXL prototype detectors at the ESR and detector simulations. *Int. J. Mod. Phys. E*, 18:524, 2009, No. 2.
- [55] H. Moeini, S. Ilieva, F. Aksouh, K. Boretzky, A. Chatillon, A. Corsi, P. Egelhof, H. Emling, G. Ickert, J. Jourdan, N. Kalantar Nayestanaki, D. Kiselev, O. Kiselev, C. Kozuharov, T. Le Bleis, X.C. Le, Yu.A. Litvinov, K. Mahata, J.P. Meier, F. Nolden, S. Paschalidis, U. Popp, H.Simon, M.Steck,T.Stöhlker, H.Weick, D.Werthmüller, A.Zalite. First feasibility experiment for the EXL project with prototype detectors at the ESR storage ring. *Nucl. Inst. Meth. Phys. Res. A*, 634:77, 2011.
- [56] T. Adachi, M.N. Harakeh, N. Kalantar-Nayestanaki, H.J. Wörtche, G.P.A. Berg, H. Simon, I.A. Koop, M. Couder, M. Fujiwara. Constant-gap spectrometer design for the electron/ion collider ELISe. *Nucl. Instr. Meth. Phys. Res. A*, 659:198, 2011.
- [57] G.P.A. Berg, T. Adachi, M.N. Harakeh, N. Kalantar-Nayestanaki, H.J. Wörtche, H. Simon, I.A. Koop, M. Couder, and M. Fujiwara, A novel spectrometer for studying exotic nuclei with the electron/ion collider ELISe, *Nucl. Instr. Meth. Phys. Res. A*, 640(1):123 – 132, 2011.
- [58] Antonov *et al.*, ELISe collaboration, The electron-ion scattering experiment ELISe at the international facility for antiproton and ion research (FAIR)-a conceptual design study, *Nucl. Instr. Meth. Phys. Res. A*, 637(1):60 – 76, 2011.
- [59] E. Guliyev, M. Kavatsyuk, P.J.J. Lemmens, G. Tambave, and H. Löhner, on behalf of the PANDA Collaboration, VHDL Implementation of Feature-Extraction Algorithm for the PANDA Electromagnetic Calorimeter, *Nucl. Instr. Meth. Phys. Res. A*, 2011.
- [60] MEDM, Motif Editor and Display Manager, <http://www.aps.anl.gov/epics/Epics Documentation/ExtensionsManuals/MEDM/MEDM.html>.
- [61] MBS status: www-win.gsi.de/daq/.

- [62] W. Levine, *The Control Handbook*, CRC Press, 1996.
- [63] B. Francis, J. Doyle, and A. Tannenbaum, *Feedback Control Theory*, Macmillan Publishing Co., 1990.
- [64] Vista control system: <http://www.vista-control.com/>.
- [65] ISIS pulsed neutron and muon source: <http://www.isis.stfc.ac.uk/>.
- [66] L.R. Dalesio, M.R. Kraimer, and A.J. Kozubal, EPICS Architecture, *International Conference on Accelerator and Large Experimental Physics Control Systems*, 1991.
- [67] J.F. Bartlett, J.S. Bobbitt, B.J. Kramper, T.E. Lahey, B.A. MacKinnon, *et al.*, The EPICS System, An Overview, 1984.
- [68] K.U. Kasemir and L.R. Dalesio, Overview of the experimental physics and industrial control system (EPICS) channel archiver, page THAP019, 2001.
- [69] R.E. West, J.F. Bartlett, J.S. Bobbitt, T.E. Lahey, Brian J. Kramper, et al, EPICS System: System Structure and User Interface, 1984.
- [70] T.M. Mooney, N.D. Arnold, B.K. Cha, M.R. Kraimer, and R.L. Sluiter, EPICS and its Role in Data Acquisition and Beamline Control, 2000.
- [71] VME/VXI, IEE standard: <http://ieeexplore.ieee.org/stamp/stamp.jsp>.
- [72] C. Cuevas, J. Heefner, G. Melton, and L. Plesea, EPICS Database Development Using ECAD Software, 1994.
- [73] vxWorks, Description: <http://www.windriver.com/products/vxworks/>.
- [74] PPC750 CPU, Technical details, <http://www.ukcpu.net/Collection/Processors/IBM/PowerPC/750.asp>.
- [75] LabView: <http://www.ni.com/labview/>.
- [76] ISEG HV: <http://www.iseg-hv.com>.
- [77] XP2042: <http://www.electrontubes.com/pdf/XP2042.pdf>.
- [78] XP2950: <http://www.electrontubes.com/pdf/XP2950.pdf>.
- [79] CPU68040: http://www.freescale.com/webapp/sps/site/prod_summary.jsp.

- [80] PPC604: http://www.everymac.com/systems/by_processor/powerpc604.html.
- [81] Pentium II: <http://www3.intel.com/design/PentiumII/prodbref/>.
- [82] Pentium IV: <http://www.intel.com/products/processor/pentium4HTXE/>.
- [83] Experimental Physics and Industrial Control System, CPU tests: <http://www.aps.anl.gov/epics/docs/USPAS2010.php>.
- [84] W. T. Eadie and F. James, Statistical methods in experimental physics, World Scientific, 2006.
- [85] R.J. Barlow, Statistics: a guide to the use of statistical methods in the physical sciences, John Wiley and Sons, 1989.
- [86] B.P. Roe, Probability and statistics in experimental physics, Springer, 1992.
- [87] LISE++: <http://groups.nscl.msu.edu/lise/lise.html>.
- [88] FEBEX: http://www.gsi.de/informationen/wti/ee/elekt_entwicklung/febex_e.html.

